UNIVERSITÀ
DEGLI STUDI
FIRENZE

DOTTORATO DI RICERCA IN
*FISICA e ASTRONOMIA*

CICLO XXVIII

COORDINATORE Prof. Roberto Livi

# Development of the Time-Resolved Ion Beam Luminescence Technique and its Application to the Provenance Studies of Lapis Lazuli

Settore Scientifico Disciplinare FIS/07


**Dottorando**
Dott. Caroline Czelusniak

**Tutore**
Prof. Pier Andrea Mandò

**Coordinatore**
Prof. *Roberto Livi*


Anni 2012/2013-2013/2014-2014/2015

*Two roads diverged in a wood, and I—*
*I took the one less traveled by,*
*And that has made all the difference.*
*(Robert Frost)*

# CONTENTS

# INTRODUCTION

The objective of this work was to implement the time-resolved ion beam induced luminescence (TRIBIL) technique at the pulsed beam facility (DEFEL) of the LABEC laboratory. LABEC is mainly dedicated to the application of Accelerator Mass Spectrometry (AMS) and Ion Beam Analysis (IBA) techniques to Cultural Heritage and environmental studies, but its instrumentation is also used in other experimental fields such as detector testing and material science. The laboratory is always passing through innovations and its philosophy is that home made hardware and software are used as often as possible. Developments of coding, mechanics and electronics are part of the routine in the laboratory. Moreover, measurement preparation concerns not only the final experimental setup but the whole beam transport process. Most of the accelerator control is performed remotely through dedicated software. Learning how to drive the accelerator and produce a proper beam can take approximately a year, considering that the accelerator time is shared between several other groups. That is why this work was written in a way to incorporate the various aspects of working in an interdisciplinary laboratory as LABEC, and to emphasize that implementing a new technique concerns the knowledge of the entire instrument as a whole (ion sources, accelerator itself, diagnostic elements and devices for beam transport).

LABEC is equipped with several beamlines, each one of them dedicated to a particular purpose. DEFEL is a beamline that was initially built at the old single-ended Van de Graaff accelerator at Arcetri, Florence, and its operation principle and first hardware version were first published in 2002 [1]. Later, after the Van de Graaff was substituted by a 3 MV Tandetron and the laboratory was moved to Sesto Fiorentino, the implementation of an improved version of the beamline was published in 2008 [2]. It consists of two electrostatic deflectors that work together to deliver to the final target - starting from the continuous beam produced by the ion sources - a pulsed beam, whose features can be finely controlled, such as mean number of ions per pulse and pulse duration. Thanks to this versatility, in particular the possibility to obtain from a single ion up to thousands of ions per bunch, the facility was potentially exploitable for several types of studies where a pulsed beam was necessary. The TRIBIL implementation did not require to largely modify the characteristics of the beamline, although it was necessary to preliminarily restore a reliable operation of the facility, which had been only occasionally employed until the start of my thesis; in addition, during my PhD period the operational capability of DEFEL was extended to the use of further ion species and not only of proton beams, until then the only ones with which DEFEL was operated. This extension to heavier

ions required a non-negligible effort for tuning the beam transport in such a way to work smoothly also with the heavier ions.

During the evolution of my thesis, besides those dedicated to the implementation of TRIBIL, the beamtime slots allocated to DEFEL were shared with another project, of which I was also a participant. This project ended up being the PhD work of a colleague ("Accurate on line measurements of low fluencies of charged particles"), which was based on different aspects and "qualities" of the DEFEL performance than required for my PhD work. In my work, as will be seen in the following, DEFEL was exploited in the more suitable specific manners to respond to the requirements of TRIBIL measurements.

TRIBIL is a relatively new technique, even though the concept has been discussed for several years. With modern instrumentation it became more easily and economically viably implemented (once an accelerator is available), but even so the literature is scarce. The physical processes behind the ionoluminescence phenomenon are themselves not completely understood. The luminescence emission can be thought as the result of the decay of excited states within the material to the ground state. We decided to implement TRIBIL with the goal to exploit its high sensitivity towards defect and impurity sites in the study of insulating and semiconductor materials, since it is known that luminescence techniques, and in particular TRIBIL, can be an effective tool to better understand these issues. The fields of application are vast, from ion implantation monitoring to basic studies of condensed matter physics. Ion-induced luminescence is extremely sensitive and can respond to impurity levels of ppm or less, and time-resolved measurements can reveal variations in defect formation through the luminescence lifetime obtained from the signals. For that, pulsed ion beams are required, and DEFEL, which offers the possibility of a good time mark of the excitation of the material, appeared to be an appropriate facility where implementing this technique.

Since LABEC is a laboratory in which one of the main activities concerns Cultural Heritage, it was quite natural that the first application of this work were addressed towards a subject of interest in this area. Lapis lazuli, a stone already extensively studied by the LABEC group and colleagues from other laboratories, was chosen as the object of study because of its historical importance. This stone has been used in many ways (for example, jewelry and pigments) since the early civilizations. There are open questions concerning the origin of lapis lazuli used in ancient times as well as in more recent periods like Renaissance. Since this stone comes from only few ores in the world, being able to state the origin of lapis lazuli in a work of art has archaeological and economic importance. IBA techniques are most indicated when probing works of art because they are non-invasive and non-destructive. Standard ion beam induced luminescence had already been applied to lapis lazuli and showed to be able to distinguish between Chilean lapis lazuli from the others that were studied because of a particular emission band only present in stones from Chile [3], and the work of my thesis was carried out attempting to find through the use of time-resolved IBIL further, more distinguishable markers. Lapis lazuli samples from Afghanistan, Myanmar and Chile were provided by the INFN of Torino. The Museum of Natural History of Florence provided samples from Tajikistan and Siberia.

LABEC is a laboratory where not only accelerator-based techniques are exploited. In fact, before I started the main work of this thesis, I was part of a team that built the first scanning X-Ray Fluorescence (XRF) system from the laboratory. As is well known, XRF is a technique for elemental analysis, based on the detection of characteristic X rays from the various elements in a material, emitted under excitation of a primary electro-magnetic radiation (such as produced by an X-ray tube). The first generation of the new scanning system took about a year to be completed and the work consisted in software and hardware development. Basically, the movement of a two-axis (vertical and horizontal) motorized linear stage was synchronized with the acquisition system, so that elemental maps relative to an irradiated area could be reconstructed. This prototype has been extensively used for diagnostics of works of arts in museums, also in the frame of a close collaboration with the "Opificio delle Pietre Dure" in Florence. Although the construction of this instrument is not connected with the main investigation performed for this thesis, it has required a considerable effort and took a relevant fraction of my time during my thesis. This effort led to an important implementation, which is now being exploited in two further PhD theses within the LABEC group. Therefore, it deserves to be described in a dedicated chapter.

The first Chapter of this thesis is dedicated to the description of the LABEC laboratory. The beam transport process, the main components of the accelerator and the various beamlines of the laboratory are presented briefly.

A detailed description of DEFEL is given in the second Chapter along with the main features of the obtained pulsed beams that are relevant for the comprehension of the topics dealt with in this work.

In the third Chapter the time-resolved luminescence technique is presented giving an insight into the processes behind the phenomenon of ion induced luminescence as it is understood nowadays. Here it is important to point out that this work is not focused on a deep treatment of physical issues concerning material sciences, so the luminescence phenomenon is viewed and presented in a basic manner. Instead, attention is given to the many advantages of using ion beams for luminescence applications and what is possible to obtain as information that can be useful to characterize materials, and specifically, for the applications subsequently reported, to find new markers for the provenance discrimination of lapis lazuli. A description is also given of these stones and of their historical importance.

The instruments and methods used in this work are presented in the fourth Chapter, including the experimental setup for the luminescence detection and the acquisition system developed on purpose during my thesis.

The fifth Chapter is dedicated to the first applications of our TRIBIL set-up, and the results obtained both with standard scintillators and lapis lazuli are described and discussed (the former were used for a basic characterization of the pulsed beam and the acquisition system).

In the sixth Chapter the XRF scanning system developed is described and some example of application are presented, among which preliminary maps obtained when scanning the same lapis lazuli samples on which TRIBIL measurements had been performed.

Finally, the conclusions and the future perspectives of the work that I have so far carried out will be presented.

# CHAPTER 1

# THE LABEC LABORATORY

Before addressing the specific issues that I have been dealing with in my PhD, I believe it is necessary, for the sake of completeness and of a better understanding of this thesis by the reader, to give an overview of the Ion Beam Analysis (IBA) techniques and of the main equipment of the accelerator laboratory where I have been working during these three years. This chapter gives therefore a synthetic description of the basic principles of IBA, of the accelerator system (ion sources, accelerator itself, beam transport elements and beam monitoring elements) and of the beamlines. For the same reason, Chapter 2 will be dedicated specifically to a more in-depth description of one of the beamlines, the pulsed beam DEFEL line, which has been the one where I have done most of the work reported in the following parts of this thesis[1].

## 1.1 ION BEAM ANALYSIS TECHNIQUES

Ion beam analysis of materials focuses on studying the composition and structure of surfaces and near-surface layers on the depth scale typically from few microns to several tens of microns. It consists in sending a beam of accelerated particles (usually in the energy range of 1 to some MeV), to impinge on the material, the composition of which must be investigated. The interactions of the beam particles with atoms and nuclei of the target material induce the emission of radiation (UV-visible-IR light, X-rays, gamma rays, secondary particles or primary particles scattered in the beam-target collisions). The emitted radiation has energies that are characteristic of the target elements or nuclei with which the interaction has taken place. Therefore, the energy spectrometry of this radiation through appropriate detectors provides the information of the target composition. In addition, information can be sometimes gathered also on the depth structure of the target. The latter may be obtained e.g. by varying the impinging beam energy (i.e. the probed depth from surface) and comparing the results at different energies, or directly in a measurement at a single beam energy, from the detection of back-scattered particles: in this case, indeed, the scattered particle energy depends not only on the hit nucleus mass (compositional information) but also on the depth at which the scattering

[1] As to the present Chapter, a further reason for giving this brief overview of the accelerator system is that getting acquainted with the accelerator operation and control took indeed a non negligible part of my time before I could be able to autonomously use it for my measurements.

has taken place (layer structure information).

The various IBA techniques are classified and named depending on the kind of emitted radiation being exploited. In PIXE (Particle-Induced X-ray Emission), the X-rays of the different elements that are detected and their energy, which is a function of the atomic number Z, form the key to provide elemental analysis. Often (and in particular at LABEC) two or three X-ray detectors with different characteristics are positioned around the target, in order to optimize altogether the detection efficiency over the largest possible range of elements. Using external beam setups (see below) a very wide Z-range is covered by PIXE (from Na to the highest-Z elements) with high sensitivity down to trace elements, exploiting the detection of either K-series, or L-series X-rays (or both), and for the highest-Z elements also the detection of M-series X-rays. Elements with lower Z than Na are however hardly detectable by PIXE owing to the very low energy of their characteristic X-rays, which are strongly absorbed either in the target itself where they are produced, or in their path to the detector. X-ray production cross sections in PIXE are very high (hundreds or even thousands of barns!), so that the technique, besides being largely multi-elemental, keeps its high sensitivity even using very low beam currents (tens of picoAmpères are sufficient with thick targets), thus resulting in achieving its goal in a totally non-damaging way. PIXE analysis can be, in addition, quantitative since all the physical parameters determining the X-ray yield (production cross section, beam energy loss in penetrating the target, absorption of the produced X-rays) are well known.

In PIGE (Particle-Induced Gamma ray Emission), one exploits the production of gamma rays arising from inelastic nuclear interactions of the beam particles. These interactions are in general more probable with low-Z nuclei because of the lower Coulomb repulsion between beam ions and target nucleus. The typically much higher energy of the gamma rays (hundreds to thousands of keV) than the one of the X-rays exploited by PIXE (in the keV to few tens of keV range) makes absorption problems negligible. This fact, together with the mentioned higher probability of emission from lower-Z nuclei, results in a good complementarity to PIXE: also very low-Z elements can be detected through the emission of gamma rays from their nuclei. Gamma ray production cross sections are known but they exhibit a very irregular trend with beam energy, with more or less narrow resonances; this fact makes PIGE less quantitative than PIXE, especially when the depth profile of the composition is not known, although - through the use of standards of similar composition - PIGE, too, can be at least semi-quantitative.

Elastic scattering of beam particles (PESA = Particle Elastic Scattering Analysis) is another IBA technique used at LABEC. Here one exploits the fact that the energy of a beam particle, scattered by a target nucleus at a given angle to the initial direction, is a function of the mass ratio between ion and target nucleus. A particle detector placed in the setup can thus provide information on the different masses of the nuclei in the target, therefore indirectly on the elements. However, except for the interactions in the surface layer, the detected energy is also a function of the depth at which the scattering has taken place, since the ion undergoes energy loss in traversing the material both before and after the beam ion-target nucleus scattering. By the use of appropriate software that simulates

the detected particle energy spectrum under given hypotheses of both composition and depth distribution of the material, and comparing the observed to the simulated spectrum, one can nevertheless often reach a good interpretation, and disentangle the two factors (composition and depth distribution) affecting the results. Thus, in the end, there is an added value (depth information) in using this technique. The typical geometry in which the particle detector is placed is backwards (BS = Backscattering Spectrometry)[2] and if the interaction cross section can be considered to be only governed by Compton repulsion ("Rutherford" hypothesis), the technique is named RBS. For interactions between low-Z ions (e.g., when protons are used) and low-Z nuclei, the distance of closest approach of the beam ions to the nucleus becomes however smaller, and nuclear forces come also into play. The cross section is no more the one of the Rutherford hypothesis and the yield of scattered particles is strongly affected by the nuclear effects. Therefore, any quantitative interpretation of the spectra must take into account the actual cross sections, which must be known experimentally - as they are indeed in many cases.

Ion beam induced luminescence (IBIL, or simply IL) consists in the emission of photons in the IR-VIS-UV range due to the interaction between ion and matter. It is mainly employed in the study of material defects and impurities. Being the technique explored in this work, it will be discussed in more detail in Chapter 3.

## 1.2 X-RAY FLUORESCENCE (XRF)

Besides ion beam techniques, LABEC is also equipped with instruments to perform XRF. As is well known, XRF is another kind of X-ray spectrometry exploiting the emission of energy-characteristic X-rays from the elements to provide information on the composition of a material. The principle is similar to the one of PIXE; however, what induces the inner-shell ionization of the atoms, and the consequent emission of the characteristic X-rays, is in XRF a beam of primary photons rather than a beam of ions as it is in PIXE. The physical effect that is exploited by XRF is therefore the photoelectric effect [3].

During the three years of my PhD, I have also worked with the XRF systems at LABEC, implementing the acquisition software to use them in scanning-mode, so as to obtain elemental maps. This part of my work will be described in the last Chapter of this thesis.

## 1.3 LABEC GENERAL VIEW

A general view of the accelerator system at LABEC is presented in Figure 1.1. The accelerator is of the electrostatic type, a Tandem with 3 MV maximum terminal voltage. As

[2]This is the only possible geometry of PESA with thick targets, because they completely stop the beam. By the way, placing detectors backwards is also the only possible geometry with PIXE, although for another reason (absorption of the X-rays within the target itself, if the X-ray detector were placed at forward angles). Instead, for PIGE, owing to the much higher energy of the emitted photons, the gamma ray detector can be placed at any angle to the to the direction of incidence of the beam.

[3]I will not enter here into any detailed description of XRF; some more considerations about XRF compared to PIXE will be given at the beginning of Chapter 6.

in all accelerators, ion production and beam transport and acceleration is performed in vacuum environments. Therefore, all the sections that I will now describe are kept at as high vacuum levels as possible; beam particles would otherwise interact with the residual gas within the beamlines, deteriorating their "qualities" (energy loss and straggling, scattering, etc.). The typical vacuum levels in the beamlines at LABEC are from some units in $10^{-8}$ to some units in $10^{-6}$ mbar (with deliberate "exceptions" in some sections that will be recalled below). These vacuum levels (which are monitored by vacuum gauges properly located along the beamlines) are achieved thanks to a number of high vacuum systems, which are connected to the lines. The kind of vacuum systems used at LABEC are turbo-molecular pumps, backed by "dry" forepumps[4] mostly of the scroll type. The various sections along the beam transport from the ion source to the end of the beamlines are separated by gate valves, to isolate one section from the other in case one needs to break the vacuum (e.g. for maintenance operation) in one of them, without venting all the other sections.

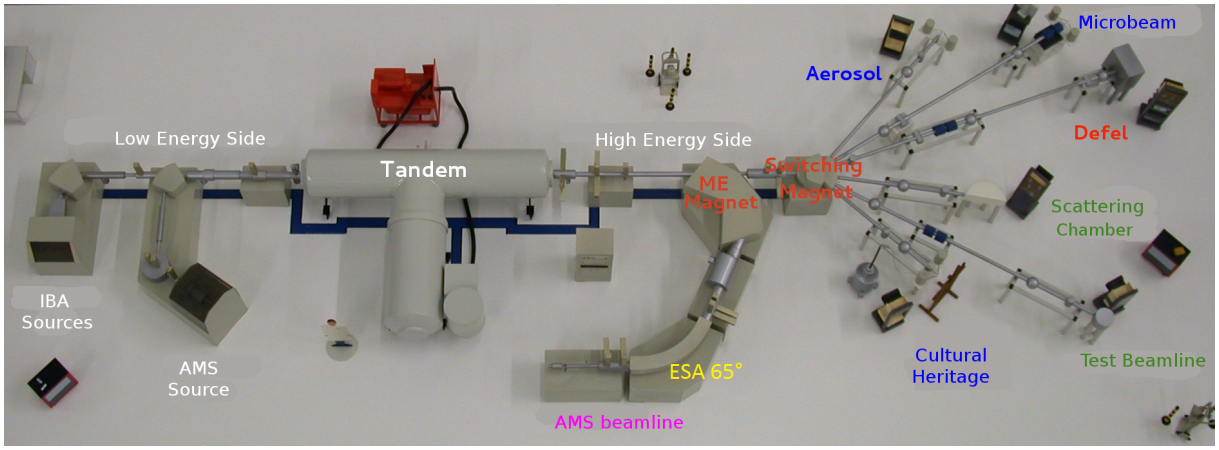


**Figure (1.1).** General view of the LABEC accelerator hall.

## 1.4 ION SOURCES

Accelerators of tandem type are designed to accept negative ions to be accelerated in a first acceleration stage to a positive voltage terminal, where they undergo a charge-exchange becoming positive ions and are thus accelerated a second time towards ground potential at the other end of the accelerator (the working principle of these accelerators will be better recalled in the following paragraph). The first requirement for the overall system to operate is therefore to produce negative ions. Negative ion sources can be of different types, forming the ions through several processes [4]. The LABEC accelerator, in particular, is equipped with three independent ion sources: a single-sample Cs-sputtering source and a Duoplasmatron are used to produce ions for the various applications of

[4]The adjective "dry" is associated with pumps working on a principle that does not imply the use of lubricants like oil or grease, which is particularly important to avoid contamination with organic compounds of the evacuated environment, as is e.g. the case when performing radiocarbon concentration measurements, as it happens at LABEC.

IBA. Another 59-sample Cs-sputtering source is usually dedicated to Accelerator Mass Spectrometry (AMS), but ions produced by this source can also be used for IBA.

In order to provide the produced ions with an initial energy of the order of few tens of keV, which is sufficient for their transmission to the entrance of the accelerator with proper characteristics (beam cross section, position, direction, etc.), all the sources are kept at the appropriate negative voltage (in a closed cabinet, to prevent electrical hazards to the people) and are connected to the beam pipes by means of isolating flanges.

### 1.4.1 Duoplasmatron

The Duoplasmatron source (see Figure 1.2) produces ions from a gaseous material. In a first region of the source, delimited by a "tapered" electrode (shroud) open at its end, electrons are emitted by thermoionic effect from a filament (properly heated by a current). A magnetic field produced by the solenoid placed around the shroud induces a spiral motion of the electrons while also confining them in the volume within the shroud, whose shape is such that the electrons are "compressed" in a smaller volume close to the open tip of the shroud (region A). A bias is applied between the cathode (the filament) and the anode just outside the tip of the shroud, while the shroud itself acts as an intermediate electrode, connected to the anode with a resistor. Part of the gas which is flowing in the region B outside the shroud enters into region A within the shroud, where it is ionized by the electrons. A gas plasma is thus formed already in region A inside the shroud. An arc of the negative components of the plasma is established towards the anode either spontaneously through the application of the bias between cathode and anode, or started by almost short-circuiting the shroud to the anode for an instant. The gas outside the tip of the shroud and the anode is ionized by the arc, and a denser plasma than in region A is locally formed in region B. A high voltage $V_{inj} = -20kV$ is applied between the anode and the beamline at ground potential. Negative ions are then extracted from the plasma and injected into the beamline. In the case of gases for which the fraction of negative ions in the plasma is negligible (for example, He) $V_{inj}$ will be positive, and positive ions will be extracted; these ions after extraction pass through a "charge exchange" canal, where a Li vapour is present (a Li reservoir connected to the canal is heated to this purpose) and a fraction (of the order of one percent) of positive ions become negative by capturing electrons from the Li ions. For hydrogen, instead, the negative ion component in the plasma is already non negligible, and in this case a negative ion beam will be directly extracted by the application of a negative $V_{inj}$[5].

[5]In this case, obviously, the charge exchange is not needed: the Li reservoir is not heated, no Li vapour is allowed to flow into the charge-exchange canal, and the negative ion beam extracted from the source will be directly transmitted downstream to the following sections of the line.

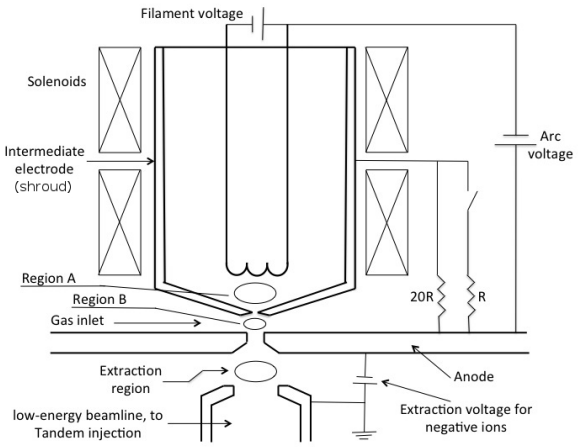


**Figure (1.2).** Schematic view of the Duoplasmatron source of the LABEC accelerator.

### 1.4.2 Cs-Sputtering Source

The sputtering sources working principle is the following: negative ions are produced in the source by bombarding, with positive cesium ions, a target of the material from which it is desired to produce an ion beam. With reference to Figure 1.3: vapours of cesium are obtained by heating a reservoir filled with that metal and connected through a pipe to the source volume. The Cs vapour "coats" the surface of an "ionizer" nearby, and also the surface of the target gets coated with a thin Cs layer. The ionizer is brought to very high temperature (about 1000 °C) and at a positive voltage with respect to the target cathode; cesium evaporates from the ionizer surface and in leaving that, owing to its weak electronegativity, forms positive ions. The positive cesium ions are thus accelerated towards the target material; the shape of the ionizer is such that they form a focused beam into a small spot (order of a fraction of mm) on the target surface. The target material atoms are sputtered from the surface of the target by the bombardment of the cesium ions, and in traversing the thin Cs layer on its surface they easily take an electron from the cesium atoms, becoming negative ions. These negative ions are accelerated from the target cathode towards the ionizer, pass through its central hole, and are injected to the beamline (at ground potential), acquiring a beam energy of about 10 - 40 keV depending on the negative voltage at which the source system is maintained. The typical value at the 59-sample Cs-sputtering source of LABEC (HVEE/846A) is 35 keV, at the single-cathode Cs-sputtering source is 20 keV.

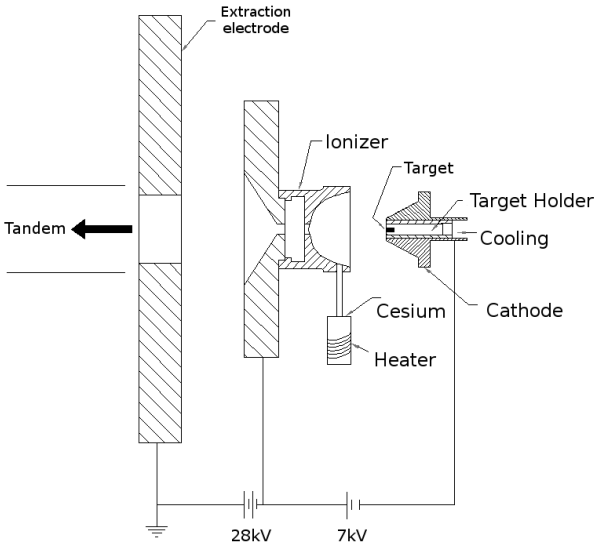


**Figure (1.3).** Schematic view of the single-cathode Cs-sputtering source of the LABEC accelerator.

## 1.5 THE TANDETRON ACCELERATOR

LABEC is equipped with a Tandem accelerator (Tandetron), produced by the Dutch company High Voltage Engineering Europe (HVEE). Tandems are electrostatic accelerators whose configuration produces the acceleration of the charged particles in two subsequent phases (this is the reason why they take the name "tandem"). Two "accelerator tubes", made with a stack of elements each made of an insulating and a metal disk, all glued together, are present (see Figure 1.4) one after the other: the first, on the injection side, from ground to a central electrode (high voltage terminal); the second, on the other side, which goes back from the high voltage terminal to ground. The reason for assembling the tubes as a stack of elements (insulating + metal) instead of a single insulating tube is that in this way the total potential difference between the terminal and ground can be distributed along the length of the tubes using appropriate resistors between the metal disks, to form a voltage divider that provides a homogeneous field along the tubes[6] (except at the entrance of the tube on the injection side, where the local field can be varied by applying an extra voltage difference between ground and the second metal plate). The high voltage at the terminal (up to 3 MV at the LABEC Tandem) is obtained with a multi-stage voltage multiplier, basically after the Cockroft-Walton principle to produce high voltage[7].

[6]This is not peculiar of Tandems of course, but applies to all electrostatic accelerators, even single-ended.

[7]The fact that the high voltage is created by such an electronic method rather than with charge transport from ground to terminal, as it happens with charge injection on a rotating belt in a van de Graaff system, has suggested the commercial name "Tandetron" to this kind of Tandem accelerators.

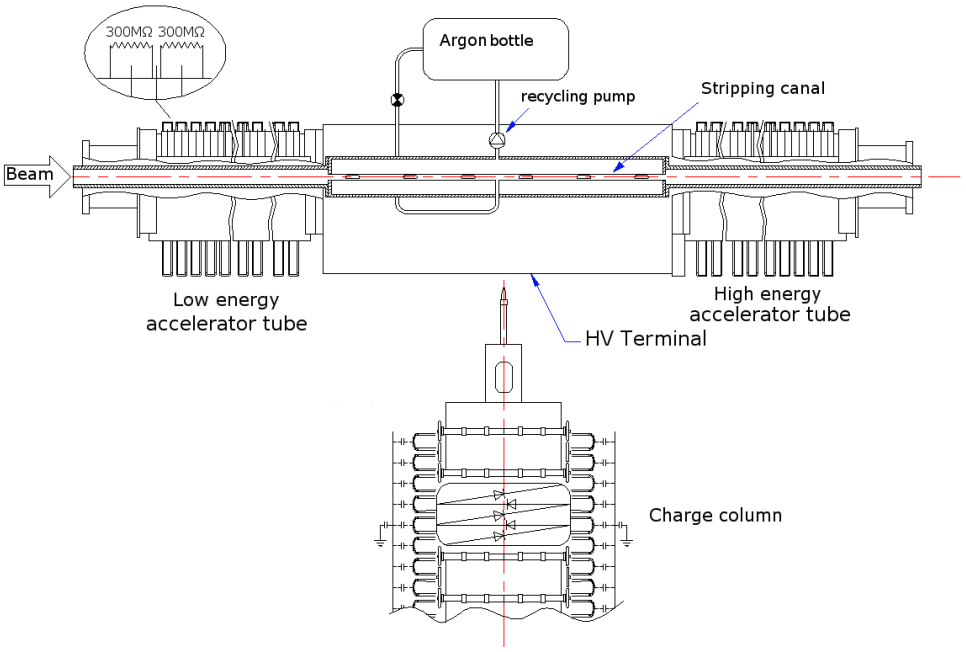


**Figure (1.4).** Schematic view of the Tandem.

Negative ions coming from the source (see the following paragraph about beam transport) are accelerated by the electric field created by the high voltage terminal in the first accelerator tube, and increase their energy up to $e(V + V_{inj})$, where $e$ is the elementary electric charge (injected ions are mono-negative), $V$ the terminal voltage and $V_{inj}$ the injection voltage (e.g. 20 kV for the Duoplasmatron source, see above). Within the terminal, the beam passes through a narrower canal (13 mm diameter and about 1 m long) where the vacuum level is on purpose kept locally worse, circulating some argon from a finely controlled output valve of a bottle placed at the HV terminal (the circulation is maintained by a local turbo pump whose exhaust is re-injected in the canal, and only a small part of the gas streams towards the grounded ends of the two tubes). In the interaction processes of the ions passing through the gas, some electrons are stripped from the incoming ions, which become positively charged. Now, the decreasing voltage from the HV terminal to ground induces a second acceleration of the ions, which reach the grounded end of the second tube with an energy $E_{final} = eV_{inj} + eV + neV = e(V_{inj} + [n + 1]V)$, where $n$ is the positive charge state after stripping.

Not all the ions emerge from the stripper canal with the same charge state $n$. As a matter of fact, there is a distribution of possible final charge states $n_i$ due to the charge exchange processes producing capture or loss of electrons in the stripper medium, and consequently the positive ions at the end of the double acceleration process within the Tandem will have a (discrete) distribution of final energies. The distribution of charge states after the stripping phase depends to a first approximation, for any given ion species (i.e. nuclear charge), on the ion velocity after the first acceleration at the entrance in the stripper gas volume, and on the stripper gas quantity. By knowing this dependence, it is possible to choose the best combination of terminal voltage and final ion charge state that optimizes the beam conditions at high energy (energy, transmitted current intensity, magnetic rigidity for the subsequent deflection one needs to apply to the beam) for a

given experiment.

For any given condition (incoming ion species and velocity) an equilibrium distribution of charge states after stripping is achieved only after a certain quantity of stripper has been encountered by the ions. Indeed, the distribution among the various charge states progressively changes with the depth traveled within the stripper, until equilibrium is reached [5]. Figure 1.5 shows an example of the charge state distribution of C ions after passing through an Ar gas and reaching equilibrium at a typical stripper gas quantity, as a function of the energy acquired in the first stage of acceleration as mono-negative ions.

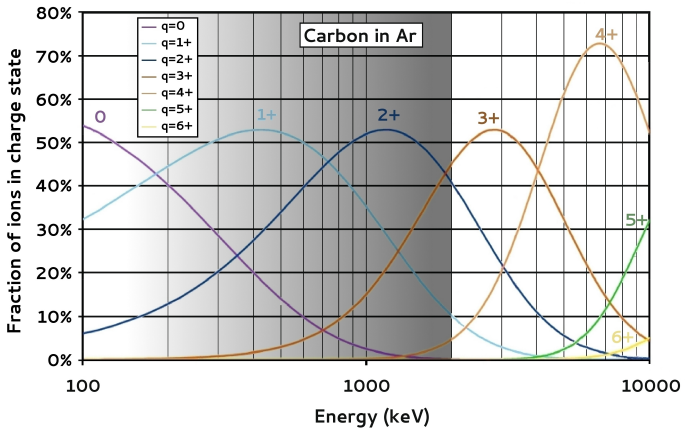


**Figure (1.5).** Charge distribution of C ions after reaching equilibrium in passing through a value of areal density thickness in Ar typically used in a high-voltage terminal of a tandem accelerator.

## 1.6 BEAM TRANSPORT

In general, along all the beamlines in both the low-energy side after the source, prior to acceleration, and the high-energy side, it is necessary to use a number of "active" elements (magnetic or electrostatic deflectors or focusing elements) to drive the beam particles along the desired trajectory, and "passive" elements to monitor the results obtained. The ion optics active elements of the beam transport line come in two varieties: magnetic and electric. Transverse magnetic and electric fields both produce a deflection of the ions without affecting their energy. An important factor to keep in mind is however the fact that electrostatic fields do not separate different ion species with equal energies (when the particles are accelerated by voltage differences, particles of a given energy and charge follow trajectories defined only by the system voltages, regardless of their different mass). The magnetic elements, on the other hand, induce deflections that have a dependence on the mass-to-charge ratio $m/q$ . This allows separation of different particle species of equal energy from one another. The last feature is very important in beam transport because one needs to select only the desired ions produced by the ion source, in the low-energy side of the accelerator; and only the desired ion charge state after stripping - and therefore final beam energy - on the high-energy side.

At the LABEC accelerator system, the active elements used for beam transport are:

- Dipoles (either electrostatic: couples of plates along the beam trajectory, to which a potential difference is applied; or magnetic: electromagnets where the field is produced by coils in which a current is circulated). Dipoles are used just to deflect the beam and (the magnetic ones) to separate different masses of equal energy.
- Einzel lenses, used for focusing purposes in the low-energy section of the system in the first part of beam transport, from beam extraction out of the sources to beam injection into the accelerator.
- Quadrupole multiplets (either electrostatic or magnetic), used for focusing purposes of the beam after they have acquired high energies in the accelerator.

A short description of these ion optics active elements will now be given.

### 1.6.1 Electrostatic dipoles

For deflection purposes, a common element for beam steering in small angles without changing the beam energy is a pair of parallel plates with a voltage difference applied between them. Couples of steering elements in both the horizontal and vertical direction are used to force the beam to recover an axis coincident with the ideal beam line. These devices are also found at the high energy side of the accelerator.

### 1.6.2 Magnetic dipoles

For larger deflection angles electromagnets are the elements that are primarily used to create a dipole (with the exception of the ESA [ElectroStatic Analyser] used after a first magnetic selection on the multi-element line at high energy for the AMS measurements).

In the electromagnets, coil windings create a constant magnetic field $B$ in the transverse direction of the beam, and $B$ can be varied in intensity and (up or down) way by changing the intensity and way of circulation of the current in the coils. When a charged particle of energy $qV$ and mass $m$ enters a uniform magnetic field $B$ oriented perpendicular to the particle trajectory, owing to the transverse Lorentz force $F_L = qvB$, it follows a circular trajectory with radius:

$$R = \frac{mv}{qB} = \frac{1}{B}\sqrt{\frac{2mV}{q}}. \tag{1.1}$$

Magnetic dipoles act therefore as a mass separator of ions with the same charge and accelerated by the same potential difference to the same energy.

A first magnet is present in the low energy region after the ion sources. Indeed, just out of the source, ions of different isotopes or different atomic species can be present: for instance, in the sputtering sources, all the isotopes of an even pure cathode target material are sputtered; the target material itself may be a compressed pellet obtained from a powder mixture of different atomic species; or it can be a solid chemical compound of more atomic species - e.g. an oxide of a metal, from which both the oxygen isotopes and the metal isotopes are sputtered. Also, when it is necessary to use the charge exchange

canal to obtain negative ions, only a small fraction of the entering positive ions will become negative, so that after this element both mono-positive and mono-negative ions will be present in the beam, while only negative ones must be transmitted to the accelerator entrance. A charge and mass selection is therefore obviously required to transmit to the accelerator entrance only the desired negative ion species.

Two more electromagnets are present in the high-energy side of the system. The first is used to separate different masses in AMS measurements, while it is kept off when performing IBA measurements. The second electromagnet is the so-called switching magnet:the vacuum chamber between the pole expansions of the yoke has many output ports at different angles. Several beamlines are installed at these output ports, so that the desired beam (mass and charge state) is transmitted into the appropriate beamline to perform the specific experiment planned.

### 1.6.3 Einzel lenses

Particles coming out of the sources must be kept on the "right" trajectory (ideally corresponding to the beam-pipe axis) to be transmitted to the entrance of the accelerator. Instead, just out of the source they have components of velocity perpendicular to the main direction of motion for a number of reasons (imperfections in the shape and alignments of the various parts of the electrodes in the sources, random thermal motion owing to the high temperatures within them, space charge effects producing an acceleration of the particles away from the axis). In order to maintain a small cross-section beam, forces must be therefore applied to deflect particles and keep them "confined" around the axis. This is accomplished by the so-called einzel lenses, which are a combination of three electrodes, where the first and third ones are at the same potential. Several modes of operation and geometries are possible [6]. The einzel lens, which is cylindrically symmetric, is the only tool for beam focusing in the low-energy side of the system, since relatively low voltage values (easily obtained) are sufficient to obtain focusing, owing to the low energy of the ions in this phase.

### 1.6.4 Quadrupole multiplets

Besides einzel lenses, multiplets of quadrupole lenses are used as focusing elements to decrease the beam dimension; they can either be electrostatic or magnetic [7]. They are used on the high-energy side of the accelerator, both in the first section after the accelerator and placed along or at the end of the beam lines in order to manipulate the beam so as to have the desired dimensions on the target. Taking e.g. an electrostatic quadrupole doublet, the first consists of four hyperbolic electrodes placed symmetrically around the beam axis (z) with positive potential $+V_0$ on the electrodes in the $+x$ and $-x$ directions and negative potential $-V_0$ on the electrodes in the $+y$ and $-y$ directions. The result of this configuration is that in one plane (xz) the beam is focused and in the other (yz) defocused. If the beam passes immediately afterwards through a second quadrupole with a 90° rotated voltage configuration (i.e. negative potential electrodes in

the $x$ direction and positive potential electrodes in the $y$ directions), adjusting the voltage values to properly different values than in the first quadrupole results in finally focusing in both planes at an certain distance to the quadrupole doublet. The magnetic quadrupole (Figure 1.6) has a similar construction to the electrostatic one: the magnet poles are made to be hyperbolic and windings are coiled in such a way to produce alternated North and South magnetic poles, which also produce (this time by the Lorentz force) focusing in one plane and defocusing on the perpendicular one. Here, too, a second quad immediately downstream is placed with a 90° rotated configuration, to finally produce a beam focus at a certain distance in both planes.

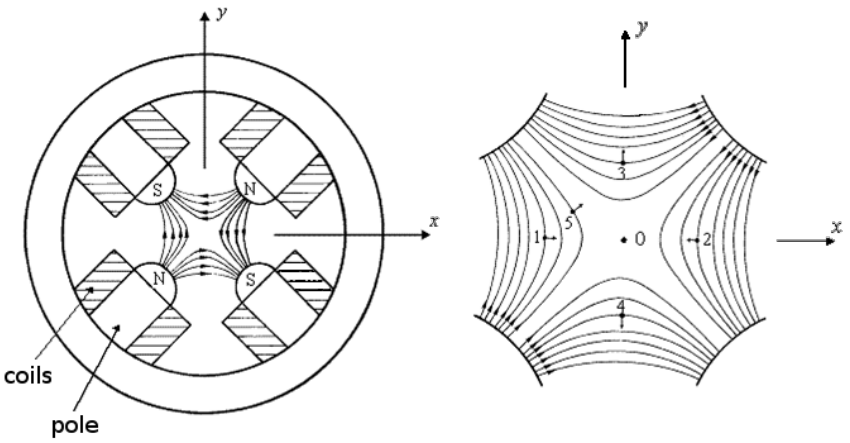


**Figure (1.6).** Left: Cross section of a typical magnetic quadrupole lens showing the associated field lines. Right: The action of the quadrupole field: the arrows represent the direction of the force produced by the magnetic field on a positive charged particle passing down into the lens for various positions in the cross section plane.

## 1.7 DIAGNOSTIC ELEMENTS

All the devices presented previously must be operated controlling their effect on the beam in some way. For that purpose, diagnostic elements are placed along the beam line everywhere they might be needed. For instance, devices to measure the beam current are placed after the ion sources and just before the entrance to the accelerator. In this way, one can know whether there are losses due to a bad beam transport from the source to the accelerator. And by changing the focusing systems and steering systems, always controlling through a diagnostic element, it is possible to optimize the amount of particles transported and accelerated. Some of the diagnostic elements used on a daily routine will be presented in this section.

### 1.7.1 Faraday cups

The simplest way to measure the current intensity of a beam of charged particles is to completely absorb the beam in a block of conducting material connected to a current meter. This device is called Faraday cup (FC in the following). This was the first method used to measure particle beam intensities. Although the principle is very simple, if not properly used it does have problems and limits. For example, one must be sure that all the

beam particles are collected, which implies that the collecting electrode be well centered. The most important problem arises if the secondary electrons ejected from the electrode when hit by the beam particles can escape without being re-captured: this would clearly alter the current reading, and can affect the accuracy even by a large amount. In order to avoid secondary electrons escape, the electrode should possibly have the shape of an as deep and narrow as possible cylinder, with a closed end at the opposite side with respect to the beam provenance (hence the name "cup") and its axis centered along the beam trajectory, so that the solid angle available for the escape of secondary electrons is reduced to a minimum. An alternative, or even an added feature, to avoid the current reading inaccuracy due to secondary electrons escape, is to bias the FC at a proper positive voltage (low voltage values can be sufficient since the energy of the largest fraction of the emitted secondary electrons is small), so that they are immediately re-captured by the FC itself. Also, a "guard ring" immediately outside the FC can be placed and biased to a negative potential, so as to repulse the ejected electrons into the FC. With these precautions, a Faraday cup does allow the beam current intensity to be quantitatively determined to good accuracy, and so these devices are often used for calibrations and current-normalization purposes.

### 1.7.2 Fluorescent screens

The simplest way to observe a charged particle beam, and to make sure the beam axis is centered at a given position along the transport, is to use a fluorescent screen, which fluoresces when and where hit by the beam. The emitted light is viewed using a compact CCD camera. This device is usually mounted on a movable support which can be inserted into the path of the beam when required. There are several kinds of fluorescent screens that can be used [8]. The ones used at LABEC are made of quartz.

### 1.7.3 Beam Profile Monitors

The use of quartz "monitors" only is not enough. In order to check beam centering and size, without stopping the beam (as it happens inserting a quartz) some system that can continuously provide the operator with this information must be placed at several positions along the beam transport. For that, beam profile monitors (BPMs) are installed on both the low and high energy side of the accelerator. BPMs provide a continuous scope display of the shape and position of the beam position in both X and Y coordinates. This can be accomplished in several ways with different methods [8].

## 1.8 ADDITIONAL ELEMENTS

Besides the devices used for diagnostics and manipulation of the beam, other elements are present along the beam path. Apertures and motorized slits are some of the additional devices that help to optimize the beam transport. As it was said before, one of the main concerns when in the process of beam transport is that the beam be centered and parallel

to the beam pipe. If this is not the case, the beam may hit the pipe walls, or any other device, producing undesired effects (radiation background, charging of insulated elements, etc.). Among other effects, ions can become neutral particles that can travel along the beam path and interfere with some measurements. They are a type of "impurity" in the beam and are difficult to eliminate since they are not affected by any electro-magnetic device[8].

Apertures can be of great use when one is interested in knowing whether the beam is centered. This elements, as the name says, are holes that have a smaller diameter than the beam pipe. They can be fixed or placed in a motorized platform, and are present in both the low and high energy sides of the accelerator. When inserted, often before a Faraday cup or a BPM, apertures show if the beam is taking the right trajectory: if the current intensity read by a Faraday cup with and without an aperture in front is the same, one can know that the beam is able to pass the middle of the aperture without significant loss. If the contrary happens, and the current intensity is much lower with the aperture inserted, this is an indication that the beam trajectory and size must be corrected using focusing and/or steering systems.

Slits are movable apertures usually made of metallic plates whose distance to the center of the beam pipe can be changed. Slits can be single or double, working only horizontally or vertically, or in both directions. The aperture size defined by the slits can be changed moving the two slits of each direction (horizontal, x, and vertical, y) symmetrically with respect to a defined center, or it can also be adjusted by acting separately on the individual slits elements. The role of slits is to produce a variable aperture limiting the beam size, in such a way that the current intensity can be increased or decreased as desired.

## 1.9 BEAM LINES AT LABEC

As mentioned and shown in Figure 1.1, after acceleration and some focusing and deflecting elements to keep the beam on the right trajectory, a large magnet is present to deflect the beam into the so-called multi-element line used for AMS. When performing other kinds of measurements, this electromagnet is switched off and the beam can proceed to the switching magnet, at the outputs of which are installed several beamlines that I will now very briefly describe, just for the sake of completeness. By convention, beamlines at "negative" angles out of the switching are those where the beam is deflected leftwards, positive ones correspond to those rightwards.

### 1.9.1 The "aerosol" beamline

The beamline at -45° is dedicated to the study of the atmospheric aerosol. Aerosol is a complex dispersed system of particles suspended in the atmosphere, both of anthropic origin (e.g. industrial emissions, traffic) and as a natural background (marine aerosol,

[8]This effect is particularly disturbing for the TRIBIL measurements, that we performed on the DEFEL beamline (see Chapter 2 where the production of pulsed beams produced just by fast deflection of the beam ions is described).

volcanic eruptions, soil dust). It has a strong influence over a wide variety of phenomena, from health effects to climate. The study of aerosol is very useful for air quality check and for the identification of the pollution sources. The beamline at LABEC [9] has few beam transport and monitoring elements that are sufficient to obtain the desired beam features. Small magnetic steerers are present for beam adjustments along the x and y directions, while focusing relies just on the pre-switching quadrupoles. A diagnostic station equipped with a quartz and a Faraday cup is located about 1 meter before the target, both to control the beam shape and its position and to measure the current beam. A mechanical fixed collimator is then used to define the final beam size, i.e. the spot on the target, typically 1 mm x 2 mm. Measurements are made with the target in air by extraction of the beam through a 500 nm thick $Si_3N_4$ window. The targets are filters, on which aerosol has been collected using proper "sampling stations" that are placed at the most disparate aerosol collection sites - urban areas, industrial environments, remote sites - during sampling campaigns. Detectors are available around the targets to perform PIXE and PIGE as routine, and occasionally particle back scattering and forward scattering measurements.

### 1.9.2 The external microbeam line

The microbeam line located at -30° after the switching magnet is dedicated to perform microbeam measurements on targets placed outside the vacuum line. The microbeam facility [10] is used when an elemental analysis over a small area (i.e. high spatial resolution) is required. The line is equipped with a strong focusing system (a doublet of magnetic quadrupoles, very close to the end of the beamline), so that it is possible to obtain a beam spot, extracted in air through ultra-thin $Si_3N_4$ windows (100 or 200 nm thickness), of less than 10x10 $\mu m^2$ on the target. The facility is also designed to perform x-y scans over a small area of the sample, obtained by changing the impinging beam position over the target through magnetic fields, perpendicular to the beam direction, generated by ferrite-cored coils. Multi-analysis can be performed by placing detectors for PIXE, PIGE, IL, and so on. By the use of dedicated acquisition softwares that associate the beam position to the radiation energies detected (which in turn correspond to the different target atoms and nuclei in the target), maps of the elements distribution over the scanned area can be reconstructed with high space resolution, still keeping the target out of the vacuum environment. If scanning through a larger area is needed, a system has been installed that moves the sample in front of the static beam and reproduces the mapped area [10].

### 1.9.3 The pulsed beam line (DEFEL)

The beamline after the output port at -20° of the switching magnet is equipped with a number of devices designed to deliver to the final target a pulsed beam, starting from the continuous beam accelerated by the Tandem. This is the beamline on which I have worked for the measurements of my PhD; thus, it will be described in particular detail later, in Chapter 2.

### 1.9.4 The scattering chamber beamline

This beamline, at the +10° output of the switching magnet, allocates at its end a large vacuum chamber where particle detectors are placed at many forward and backward angles with respect to the point of incidence of the beam on the target. It was initially designed to perform measurements of non-Rutherford elastic scattering cross sections of low-Z ions such as protons on low-Z materials, when nuclear forces come into play in addition to the Coulomb repulsion, and more or less strongly affect the actual interaction probability. The knowledge of the actual cross section is needed to obtain quantitative results from particle elastic scattering measurements. The final setup in this chamber however has not been completed and at the moment this beamline is not used.

### 1.9.5 The general purpose in-vacuum IBA beamline

A beamline at the +30° output port of the switching magnet is available, with a final vacuum chamber where any kind of targets can be inserted for IBA measurements, when placing the target in vacuum is not a problem, or in-vacuum measurements are even really needed in order to avoid the energy straggling problems in the external beam setups. Indeed, although the very thin window and the close distance of the targets from the beam exit window keep these effects often negligible also in the external beam lines, on some occasions a very good energy definition is required, e.g. when performing accurate cross sections measurements as a function of beam energy, or when a high depth resolution is required in back scattering spectrometry measurements. In these cases the measurements must be performed with the target in vacuum, using this beamline. Here, too, the detector system is adequate for PIXE, PIGE and particle back- and forward-scattering experiments. The line itself is equipped with standard beam-driving systems (small magnetic steeres) and a magnetic quadrupole doublet (not a strong-focusing one however) for a precise geometrical definition of the beam direction and size, which is particularly necessary in most of the experiments here performed. A monitoring station equipped with a quartz viewer and a Faraday cup is also installed just before the final measurement chamber.

### 1.9.6 The "Cultural Heritage" beamline

Another external beam line, very similar to the one above described dedicated to the measurements on aerosols, is available at +45° to perform compositional measurements on objects of interest for Cultural Heritage problems (from paintings, to written documents, to ceramics, metal artifacts, etc.). The beamline transport and monitoring elements are the same as in the aerosol beamline; the final collimator before beam extraction, which defines beam size on target, is however usually smaller, with typical beam size on target from 1 mm to 300 $\mu$m. Smaller sizes cannot be obtained by collimation without producing scattering effects and "halos" of the beam; when a smaller beam size is required, therefore, the measurements are performed at the dedicated microbeam line where a strong focusing system is installed, as described above. The measurement setup also includes detectors for

PIXE, PIGE and backscattering measurements, but the sample holder here is mounted on a movable x-y stage with large travel excursions and good load capacity, in order to allow the measurements also on large and heavy objects.

# CHAPTER 2

# THE PULSED BEAM FACILITY

The pulsed beam facility (DEFEL) was first built in the old Van de Graaff accelerator in Florence [1]. After the Van de Graaff accelerator was substituted by the 3 MeV Tandetron at LABEC laboratory, the pulsed beamline was transferred to the new facility and improved [2]. DEFEL was built with the idea of producing a pulsed beam with a very well defined and short duration, and where the average number of particles per bunch could be varied at will. The operating principle consists in a fast transverse deflection of the continuous beam of the accelerator, thus allowing it to be transmitted beyond a narrow slit - placed some meters downstream the deflection - only for a short time lapse (of the order of few ns or less). The adjustments of the beam intensity and of the size of the slit allows the creation of a pulsed beam with a variable and finely controllable number of particles in each pulse. The repetition rate can be selected from single shot to some kHz.

Because of the possibility of an excellent time definition of the transmitted pulse, as well as space definition, and of the possibility to create bunches of variable average number of ions, the facility can be exploited for a large number of applications. The facility can be set to deliver an average of one ion per pulse (or even less), for example in order to probe radiation damage by releasing even very low controlled doses to materials. On the other hand, by increasing the beam current, bunches up to thousands of ions can be obtained with a larger and larger total energy per pulse delivered to the target. Being this energy always an integer multiple of the one of the single ion, typical applications are those of tests of response linearity [11] of detectors and associated electronics, even as a function of the interaction point [12]. The timing performance of detectors and electronics can also be investigated [13]. Other applications are the direct measurement of energy loss and of the straggling in thin material layers, and, as mentioned above, radiation hardness tests with accurate dose check. Recently, one of the studies performed at DEFEL, in which I participated, has been about material modifications, more precisely diamond implantation with finely controlled doses [14]. Parallel to this thesis, another work has been carried out making use of the DEFEL beamline. Published recently [15], this work, which I was also taking part to, had as objective to calibrate the signal intensity a micro-channel plate (MCP) detector, which operates allowing the transmission of the beam, through the use of a silicon diode stopping the beam downstream. Calibration curves were produced for a variety of ions (protons, oxygen, carbon, lithium). In this way, in the future, it will be

possible to deliver known doses to targets by using only the MCP as an online detector that tells the number of ions the target received. By a homemade software it is possible to block the beam when the desired dose has been reached.

Understanding how the DEFEL beamline works and knowing how to use it in the proper way for the measurements performed for this thesis was a big part of the work. This beamline is very versatile in the ways of how it can be operated to give the kind of beam one needs. This flexibility was exploited in this work, as it will be presented in the following Chapters. For these reasons a detailed description of the beamline from the mechanical and electronic point of view will be given in this Chapter, as well as the main characteristics of the pulsed beam obtained.

## 2.1 GENERAL VIEW OF DEFEL

Figure 2.1 shows a sketch of the beamline, along with its main electronics. Slits 1, 2, and 3 are motorized slits used to select the central part of the beam. Tantalum apertures are placed along the beam line; apertures 1 and 3 are 4.5 mm (horizontally) x 19 mm (vertically) and aperture 2 is 4 mm (horizontally) x 10 mm (vertically). Apertures 1 and 3 have been introduced both for limiting the beam so it enters only the zones of uniform field of the deflectors, and at the same time for protecting the isolating support of the plates against accidental hitting of the beam (especially during beam focusing and alignment operations). Aperture 2 acts as a beam stopper during the predeflector operation. Monitor Stations 1, 2 and 3 are motorized rotating platforms used for diagnostic purposes during the setup stage. Vacuum systems 1, 2, 3 and 4 are high vacuum pumping stations. A doublet of magnetic quadrupoles, inside which the deflector is located, is also installed in the beamline.

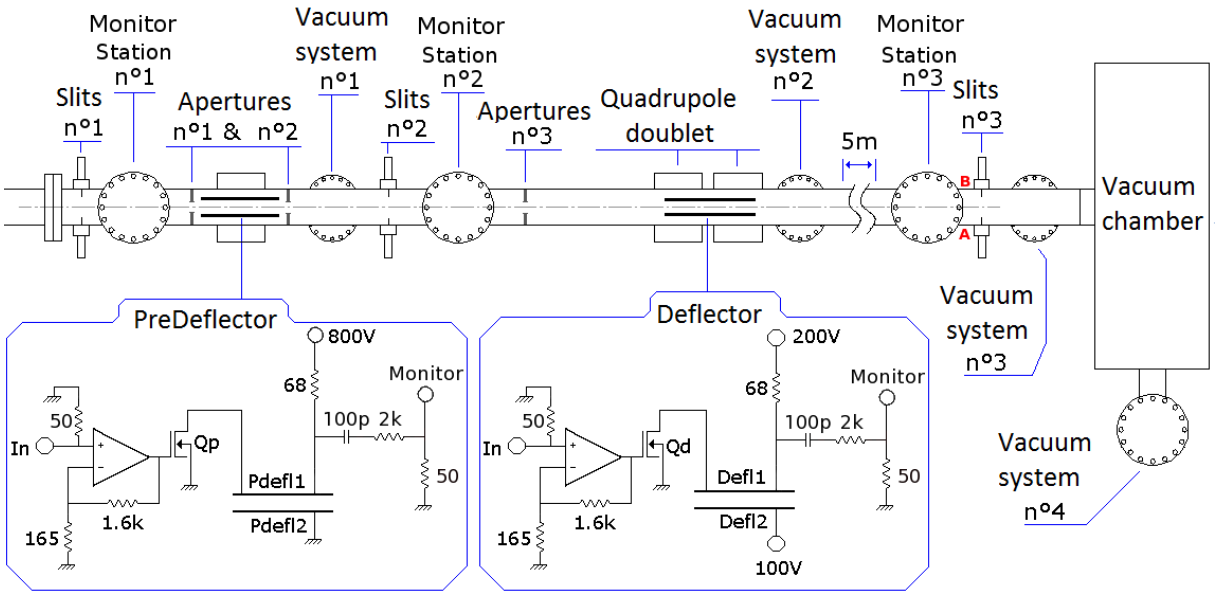


**Figure (2.1).** Schematic of the DEFEL beam line structure together with the driving electronics of the deflecting devices.

As mentioned in Chapter 1, after the acceleration of the ions, on the high energy side

of the Tandem, the beam is focused by means of a doublet of electrostatic quadrupoles. The beam is then deflected to the desired beam line by the switching magnet. Before the switching magnet, motorized slits are used to select the core of the beam, finding the right compromise between the beam size and the amount of current intensity needed for the measurement. This is performed by acting on the pre-switching slits and monitoring the beam at the first monitor station of the beam line. There, a rotating platform makes it possible to measure the beam current thanks to a Faraday cup, or to visualize the beam by inserting a quartz in the beam path and remotely observing its luminescence by a camera.

Slits 1 are used to better select the central part of the beam to enter the predeflector. Slits 2, placed after the predeflector, are antiscattering slits and are initially adjusted at the same aperture as slits 1. Being a constraint for the beam path, Slits 2 stop a large part of the particles accidentally scattered by the predeflector plates from reaching the measurement chambers along uncontrolled paths. Slits 1 are adjusted again observing the beam (position and current) at Monitor 1. One step at a time one makes sure that no element is stopping the beam. The next step is to let the beam pass through the first diagnostic station (moving the rotating platform in such a way that no beam viewing or measuring element is inserted along the beam trajectory) and be transmitted to Monitor 2. At this point, one has the possibility to work with the first X-Y steeres installed in the beamline, that are not shown in Figure 2.1. They are placed between the predeflector and Monitor Station 2, and are used to make sure the beam is centered. Also, slits 2 can be finely adjusted while monitoring the beam. After this procedure it is time to let the beam pass through Monitor Station 2 and reach Monitor Station 3. At this stage, the beam is once again placed in the center, if needed, by the use of a second pair of X-Y steerers placed between the deflector and Monitor 3. The magnetic quadrupoles are now used to focus the beam. Once "optimized" the beam condition at Monitor Station 3, the next step depends on the experiment.

## 2.2 THE ELECTROSTATIC DEFLECTORS

The DEFEL chopper system consists of two electrostatic deflectors. The reason for using two deflectors instead of one, which alone would already work as a chopper, will be explained below in this paragraph. Both deflectors are made of two plates (60 cm long, 20 mm wide, 2 mm thick) parallel to the beamline, 5 mm apart from each other. Predeflector and deflector act at a right angle with respect to one another. The predeflector deflects the beam horizontally and the deflector vertically. The first one that the beam encounters is the "predeflector", whose driving electronics can be seen in Figure 2.1. In the stationary state, the mosfet Qp (BUK 454-800V) is off, so a voltage $V_d$=800 V is applied to the upper plate while the lower plate is kept at ground potential. In this configuration, the ions are deflected in such a way that they are then stopped at the position of aperture 2. The "Monitor" output is used as a trigger signal, which is a pulse obtained by the upper plate voltage transition.

A clock signal is then sent to the input IN of an operational amplifier (see Figure 2.1) with a frequency that can be set from 0 to few kHz. When a pulse is applied to IN, the mosfet is quickly brought to conduction and the voltage on the upper plate drops almost to ground. In this configuration with both plates at ground the beam is allowed to pass in a continuous mode downstream and continue traveling along the beamline to the deflector. The time period during which the beam is allowed to pass in a continuous mode before the upper plate voltage is restored to 800 V can be set approximately from 800 ns to 5 $\mu$s. The choice for this time depends on the velocity of the ions.

The driving electronics of the second deflector, or just deflector, is similar to the one of the predeflector, as can be seen in Figure 2.1. The differences are the mosfet used, in this case a Qd (IRF 9610) that is faster than Qp, and the amplitude of the deflecting voltages applied to the plates. In the stationary case the deflector upper plate is kept at +200 V while the bottom one is kept at +100 V. In this configuration, the beam is deflected downwards to position A in the slits 3 in Figure 2.1. When a clock signal is sent to the input IN of the operational amplifier, the upper plate is sent to ground and the beam is deflected upwards to position B in slits 3.

If the predeflector is not deflecting the beam, the abrupt voltage transition between the deflector plates produces a fast sweep of the beam across slits 3, allowing a bunch of particles to enter the measurement chamber. To achieve this goal, the voltage transitions on the predeflector plates are properly synchronized with those on the deflector. Figure 2.2 shows the driving signal of the deflector starting during the one of the predeflector and ending a few microseconds after the predeflector transition to the stationary state. The synchronization takes into account also the transit time of the particles from the predeflector to the deflector (for instance, about 41.5 ns/m for 3 MeV protons).

As mentioned above, in principle one might also operate using just the deflector (as by the way had been done in the first version of DEFEL at the old accelerator, since the overall beamline length was much shorter). However, there are advantages from having now added in the setup also the predeflector, which has two purposes. Firstly, it reduces the possible radiation background created by the beam being stopped near the measurement chamber even in the time periods during which the beam is not transmitted to the target ("beam-off" time). This might negatively affect the quality of the results, even greatly, depending on the kind of measurements being performed; with the predeflector, stopping the beam for most of the "beam-off" time at A2 instead of A or B - i.e. much farther than would happen if the deflector only were present - the radiation background around the measurement chamber is drastically reduced. Secondly, the presence of the predeflector inhibits the beam from passing through the final slits during the return transition of the deflector pulse. This automatically allows the bunch to be created only by the falling voltage transition of the deflector, which is intrinsically faster due to the driving electronics.

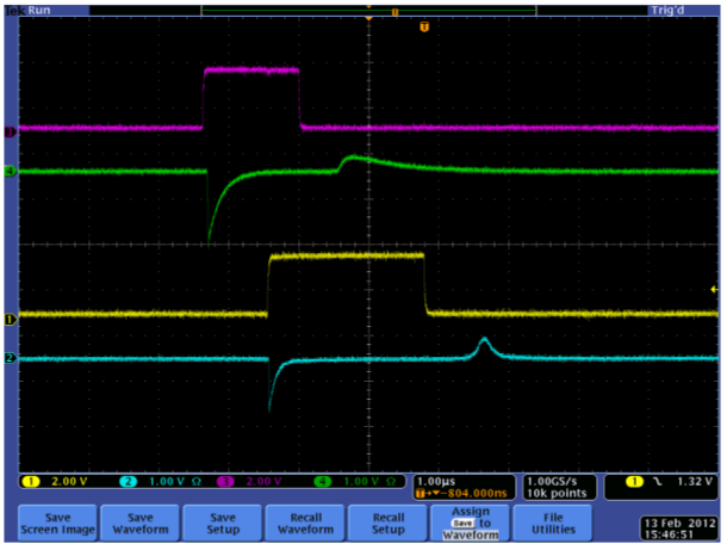


**Figure (2.2).** Synchronization of the predeflector and deflector pulses. The predeflector driving (pink) and monitor (green) starts before the deflector driving (yellow) and monitor (blue) signal.

## 2.3 PULSED BEAM FEATURES

Usually, inside the measurement chamber additional elements are used to verify that the beam is correctly entering the chamber and to choose the right configuration for the final slits 3. Besides the diagnostic devices already presented, some experiments require the knowledge of the bunch average multiplicity once the deflectors are put to operation. For that, a photodiode detector can be placed in front of the pulsed beam path. Since the charge collection time of the detector is much longer than the pulse duration, each bunch produce an energy release in the detector that is seen as a single event. The average multiplicity per bunch can be adjusted in various ways, by acting on the aperture of slits 3 or the current intensity, which in turn can be varied by acting on the slits upstream along the DEFEL line, or even - within certain limits - by changing the settings at the ion source or in the beam transport at low-energy and at high energy before the switching magnet.

After setting beam transport at best one sets the chopper system in the ON mode. When performing time-resolved luminescence, which has been the main goal of my work during my PhD, it is important to know the duration of the excitation. This parameter and the average particle multiplicity of the bunches are related to many fixed and variable parameters. If three assumptions are made, one can calculate the duration of the transmitted pulse in a relatively simple manner. These assumptions are: the beam as far as the deflector is concerned has negligible dimensions and travels along the deflector axis; the voltage transition is “instantaneous” (in practice, shorter than the time of travel of the particles along the deflector’s length – e.g., for 3 MeV protons, about 20 ns) and its propagation time along the upper plate is negligible; the electric field inside the plates is uniform, no border effects are considered.

Under these assumptions, the ion motion inside the deflector can be described by simple expressions. Since the electric field in the deflector is directed along y, the motion

along x is uniform with $x(t) = v_b t$. The relevant motion happens along the y axis. It is possible to start by considering only the two extreme states, corresponding to when the electric field is steadily downwards (negative potential difference) or upwards (positive potential difference). In the first state, the deflector upper plate is at $V_d$=200V and the lower one at +100 V, so the electric potential difference is -$V_d$/2. In the second, the upper plate is brought to ground and the difference is $V_d$/2. The motion within the deflector is represented in the two cases by the following equation:

$$\ddot{y} = \frac{\pm q V_d}{2md}, \tag{2.1}$$

where $m$ is the ion mass, and $d$ is the distance between the deflector plates. The plus or minus signals correspond to deflections upwards and downwards, respectively. If t=0 is the instant when the ion enters the deflector, and considering the conditions $\dot{y} = 0$ and $y(0) = 0$, it is possible to write:

$$\dot{y}(t) = \frac{\pm q V_d}{2md} t \tag{2.2}$$

and

$$y(t) = \frac{\pm 1}{4} \frac{q V_d}{md} t^2 \tag{2.3}$$

The minimum exit height is given at time $t_t$, that is the ion traveling time inside the deflector. In this case:

$$y_{out}^{(min)} = \frac{-1}{4} \frac{q V_d}{md} t_t^2 \tag{2.4}$$

Instead, the maximum exit height is given by:

$$y_{out}^{(max)} = \frac{1}{4} \frac{q V_d}{md} t_t^2 \tag{2.5}$$

For an ion to hit A or B it must have crossed the entire deflector, so in the intermediate cases (particles within the deflector at the moment of the voltage transition) the y excursion is comprised between the limits. Thus, the total deflection takes a time $t_t$. Once out from the deflector, the ion proceeds along a linear path starting from a height $y(t_t)$ and at an angle $\alpha$, with respect to the beam pipe axis, given by:

$$tan\alpha = \frac{\dot{y}(t_t)}{\dot{x}(t_t)} \tag{2.6}$$

The y position on the final slits 3 is given by:

$$y_{slit} = y(t_t) + L tan\alpha \tag{2.7}$$

where L is the distance between the end of the deflector and the final slits. Replacing $t_t = l/v_x = l\sqrt{m/2E}$, where $l$ is the length of the deflector plates, and calculating $y_{slit}$ maximum and minimum, by subtracting one from the other it is possible to find the distance between the two stationary hitting points A and B:

$$D = \frac{qV_d}{4dE} l(l + 2L) \tag{2.8}$$

The average transverse beam velocity $v_T$ on slits 3 is then given by:

$$v_T = \frac{D}{t_t} = \frac{qV_d(l + 2L)}{4d} \sqrt{\frac{2}{mE}} \tag{2.9}$$

The actual motion of the beam spot from A to B is more complex than the uniform motion assumed in this simplified description. However, such description is a reasonable first approximation, which well keeps into account the parameters on which particle multiplicity per bunch and pulse duration depend on. To calculate the mean number of ions per bunch n as a function of the apparatus parameters one can start by writing:

$$n = \frac{1}{e} \int_{t_i}^{t_f} I dt. \tag{2.10}$$

The transit time across the final slits 3 is: $t = s/v_T$, so $n$ can be written as:

$$n = \frac{I}{e} \frac{s}{v_T}, \tag{2.11}$$

where I is the beam current. Substituting $v_T$, the following expression can be written:

$$n = \frac{4sdI}{e^2 V_d(l + 2L)} \sqrt{\frac{mE}{2}}. \tag{2.12}$$

Apart from the fixed geometrical parameters ($l$, $L$, $d$) and from the particle mass $m$ and energy $E$, $n$ depends on the aperture of the final slits $s$, the deflector voltage $V_d$ and beam current $I$. A precise control over these three parameters is possible, so a fine control on the mean number of ions per bunch is possible.

The ions will pass across the final slits 3 for a time that depends on their aperture compared to $D$ and on the finite size of the beam spot there. If $h$ is the beam diameter, the bunch total duration $T$, to a first approximation, is given by:

$$T = \sqrt{\frac{mE}{2}} \frac{4d(s + h)}{eV_d(l + 2L)} \tag{2.13}$$

So far the voltage falling time on the upper plate of the deflector was considered negligible. Instead, both predeflector and deflector upper plate take a time to make the transition that is of few ns for the deflector, and around 40 ns for the predeflector. Substantially, the system behavior is analogous to the instantaneous transition, with only a short additional time $\Delta t$, because the transition is anyway fast relative to the transit time of the ions inside the deflector.

As already mentioned, the mean number of particles per bunch depends on the elements of the beamline (such as slits and deflector voltage) and on the features of the beam (current, energy, mass). Once these parameters have been fixed, when on pulsed mode, the actual number of ions per bunch will follow a Poisson distribution. This characteristic is a consequence of the statistical distribution of the ions in the original beam

and can be verified by placing a Si detector (Hamamatsu 3590) in the beam path. As already mentioned, the signal amplitude is proportional to the bunch multiplicity, as can be seen in Figure 2.3 on the left, which shows a shaped photodiode output seen with an oscilloscope. An example of a Si detector output spectrum can be seen in Figure 2.3 in the middle, which shows that equally spaced peaks are clearly visible corresponding to particle bunches of different multiplicity. For this reason, an energy spectrum taken from a Si detector constitutes a direct measurement of the distribution of the number of ions in each bunch. Figure 2.3 on the right shows as an example the Poisson fit of the ions multiplicity distribution in the beam bunches obtained from a pulsed beam of 7.5 MeV 7 $Li^{2+}$ ions. In this case the mean number of ions per bunch was of approximately 3.8.

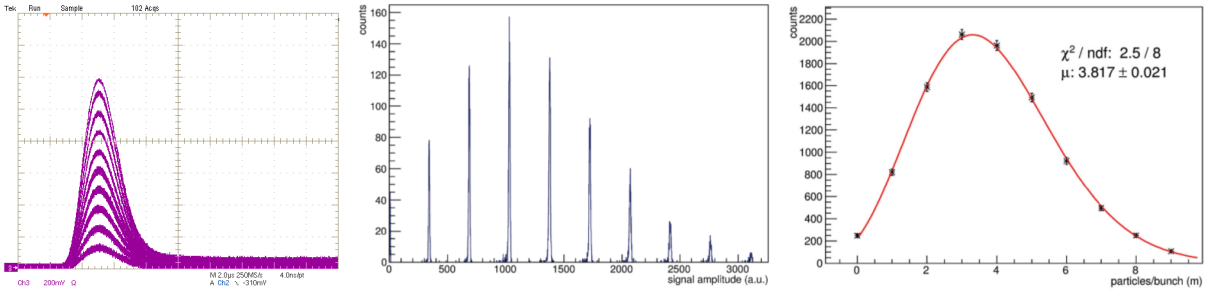


**Figure (2.3).** On the left: Si detector output seen with an oscilloscope showing the proportionality of the signal to the bunch multiplicity. On the middle: Si detector output spectrum. On the right: Poisson fit of the ions ($Li^{2+}$) distribution with a mean number of ions per bunch of approximately 3.8.

The time resolution of the chopper has been measured in a previous work [16], and since then the system has not been changed. The timing signal for the deflector transition from off to on mode is obtained by the monitor signal derived from the upper plate voltage transition. The measurement of the time interval between the deflector transition and the signal generated by a silicon detector was related to the bunch energy. As it can be seen in Figure 2.4 in the left, the time interval presents an asymptotic trend for high bunch multiplicity, reaching 18 ns. The time interval distribution, which is a measurement of the time resolution of the system, is shown in Figure 2.4 on the right for high bunch multiplicity. The FWHM in this case was of 400 ps. Since the results are also dependent on the electronic configuration, it is possible to say that the DEFEL time resolution alone is surely better than 400 ps.

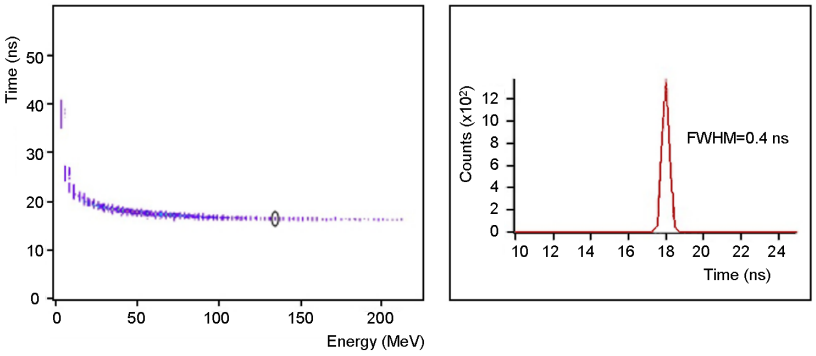


**Figure (2.4).** Time interval versus energy released (left). On the right, distribution of the times for the energy value corresponding to the circle in the left figure. Taken from [16].

# CHAPTER 3

# TIME-RESOLVED ION BEAM INDUCED LUMINESCENCE IN MINERALS

Luminescence is the emission of light from any substance and occurs from electronically excited states. Since this work applied the time-resolved luminescence technique to the study of lapis lazuli, this chapter focuses on luminescence in minerals. But it is important to point out that luminescence applications are extensive. This technique can be used during material modification with ions beams in order to monitor the creation of intrinsic defects [17], [18]. It can also be applied to the study of gemstones [19], [20], also helping to differentiate natural from synthetic analogous [21], or even discriminate between similar gemstones [22]. Moreover, it can be applied to medical areas [23] and crystal field studies [24].

A luminescent mineral is a solid that converts certain types of energy into electromagnetic radiation with energy over and above that from thermal radiation. The luminescent mineral consists of a host lattice and luminescent centers (impurities or defects). Luminescence techniques are very sensitive towards imperfections and structural changes in materials. Each type of emission site, impurity or structural defect, will have a different emission spectrum and different decay lifetime, that can additionally have different temperature dependence. The sites are often sensitive to the excitation energy and to the ionization rate, which means that different conditions can reveal different components of the possible luminescence processes [25]. The luminescence emission is also sensitive to the long range interaction with neighboring ions [26]. This high sensitivity can be both a problem and a bonus. On one hand it means that every sample will differ to some extent, even nominally pure ones [27]. On the other hand it can offer an excellent tool to quantify differences between samples.

Many are the possible sources of excitation to perform luminescence analysis. If the excitation source are photons the process is termed photoluminescence. Luminescence resulting from excitation with electrons is termed cathodoluminescence. These techniques have been applied to the study of minerals and they have been able to characterize hundreds of minerals [28]. The technique where one uses ion beams as the excitation source is termed in different ways in the literature. Ion beam induced luminescence (IBIL) or ionoluminescence (IL) are some of the terms found.

IL offers some advantages and complements the techniques where other excitation

sources are used. One of the main advantages is that with IL one can vary the ion energy and mass to change the depth profile of the excitation process. With IL it is also possible to vary the rate of energy deposition along the ionization track. With this in mind, one of the most attractive characteristics of IL is the vast possibilities for probing a target [17].

Luminescence measurements can be performed in two ways: steady state or time-resolved. Steady-state measurements are performed by constantly irradiating the target and at the same time recording the emission spectrum. Instead, time-resolved measurements are performed exposing the target to an excitation pulse and recording the temporal behavior of the luminescence intensity after the excitation is switched off. Each luminescence site has a different decay lifetime that is a characteristic of the site and the temperature [29]. The decay time or lifetime is the mean time that the luminescence center spends in the excited state prior to its return to the ground state. Time-resolved measurements are very powerful because they can separate variants of a particular type of defect, revealing overlapping features that would not be seen by only steady state data.

This chapter will expose the mechanisms behind luminescence in minerals, starting from the interaction between ions and matter. A brief description of the instruments involved in this technique will be given. Since time-resolved ion beam induced luminescence (TRIBIL) is a technique that is not explored by many facilities and authors, the description of time-resolved measurements will begin with luminescence measurements in general. In this way, different techniques and their limitations will be presented. Some of the applications of IL and TRIBIL to the study of minerals and other materials will also be exposed. The theory and mathematics behind the application of the technique will be limited to the interest of this work.

## 3.1 INTERACTION BETWEEN IONS AND MATTER

Charged particles penetrating matter will interact with electrons and nuclei in the material through electromagnetic forces [30]. The result of these interactions is the transfer of the particles energy to the medium. The energy deposition is described by the linear stopping power $dE/dx$ which gives the energy transfer per path-length of a particle along its trajectory. The energy loss of a particle traveling through a material is due to a series of collisions with the electrons (electronic stopping power) and the nuclei (nuclear stopping power) in the target [30], [31]. Both stopping powers increase with decreasing energy until they reach a maximum value, and thereafter decrease. The total stopping power is the sum of both components. Nuclear stopping increases when the mass of the ion increases and it can be larger than electronic stopping at low energy. The nuclear stopping component is very small at ion energies above 200 keV/amu, with a typical value being below 1% of the electronic stopping [32]. Therefore, for ions of a few MeV, the nuclear stopping contributes only to the very end of the stopping curve.

Whereas the individual electronic collisions do not lead to significant deviations of the projectile flight direction from its original one, this is not the case for nuclear collisions. Hence, for projectiles with dominant nuclear energy transfer, the particles will follow a

zig-zag movement until they come to rest. This gives rise to a spatially extended "damage" distribution. Since nuclear interactions lead to a significant transfer of kinetic energy to the target atom, the latter may be displaced from its original positions, and structural defects may thus be created.

In contrast, projectiles with dominant electronic energy transfer follow a straight flight path. Electronic energy transfer occurs because a charged particle traversing a medium will interact with the electrons of the material through Coulomb forces. The interaction can result either in the raise of electrons to a higher-lying shell within the atoms of the material (excitation), or in the removal of the electron from the atom (ionization). The energy that is transferred to the electron must come at the expense of the charged particle, and its velocity is therefore decreased as a result of the encounter. Moreover, it is possible that electrons, after having left their parent atom, will have sufficient energy to create further ions. These electrons represent an indirect way by which the charged particle energy is transferred to the material. The range of these electrons is small compared with the range of the incident energetic particle, so the ionization is still formed close to the charged particle track. Electronic energy transfer, if sufficiently small, does not show any remarkable damage effect in metallic targets. Only upon very high electronic energy transfer by heavy ions, structural changes are created. Instead, electronic energy transfer often plays a dominant role in insulators, where it may lead to the formation of structural defects, to radical formation, to bond breaking, or to the formation of novel bonds [33].

## 3.2 ION BEAM INDUCED LUMINESCENCE IN SOLIDS

Luminescence is the emission of light from any substance due to electronic transitions from excited states to the ground state or other state with lower energy [34]. Luminescence in solids can be understood in terms of the band scheme [35], [36]. Since atoms in minerals influence each other strongly, the energy levels of individual atoms are combined and form the bands, namely energy zones filled by electrons (Figure 3.1). The highest filled band, the valence band, is separated from the lowest empty band, the conduction band, by an energy gap $E_g$. Variations due to lattice defects and impurities occur in the energy bands, producing local electronic energy levels (traps or activators) in the normally forbidden region between the conduction and valence bands. If these levels are unoccupied, electrons moving in the conduction band may enter these centers.

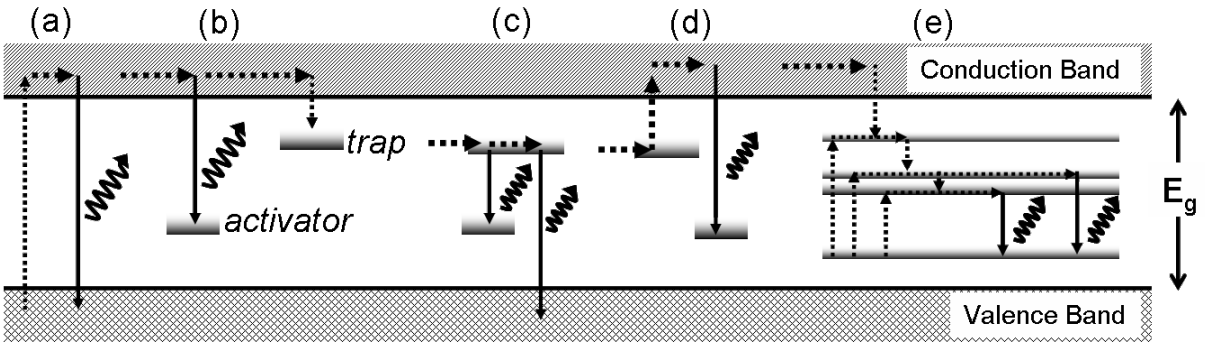


**Figure (3.1).** Band-scheme of luminescence in solids. Each process is explained in the text. The up dashed arrows correspond to energy absorption due to an incident particle. The full down arrows correspond to the emission of light while the down dashed arrows correspond to non radiative recombinations.

As a result of the absorption of energy of a penetrating particle in the material, the energy of an electronically excited state may be lost in a variety of ways. A radiative decay is a process in which the excitation energy is released as a photon. A more common fate is non-radiative decay, in which the excess energy is converted into thermal motion of the environment.

Concerning the radiative recombinations, in solids they can be divided into two types: intrinsic and extrinsic [37]. Intrinsic luminescence originates from inter-band transitions (Figure 3.1a). After the electron excitation from the valence band to the conduction band, recombination of this electron with a hole in the valence band generates a photon, the energy of which corresponds to the band gap $E_g$. Extrinsic luminescence has its origin in lattice defects or impurities. The excited electron may also recombine with an activator, with the consequent luminescence emission, or a trap, with the consequent electron capture, within the forbidden gap (Figure 3.1b). Following trapping of an electron, luminescence can occur through direct recombination of electrons from a trap with an activator or with a hole in the valence band (Figure 3.1c). Not only, a trapped electron can also be released to the conduction band by additional stimulation (heat or light), followed by radiative recombination with an activator (Figure 3.1d). Another type of radiative recombination is when electrons of defect ions, after excitation, recombine with the ground state of the ion with luminescence emission (Figure 3.1e);

As just described, IL signals are related to the emitting atoms, in practice to the energy levels of their external valence electrons. IL is very sensitive to the chemical state (valence), and the local symmetry of the emitting atom, as well as to the covalence character of the bonds it forms inside the material and the spatial symmetry of the crystalline lattice in which that atom is located. IL is especially sensitive to the presence of certain elements, such as d-transition metal ions and rare earths [38]. It can not only discriminate between different types of defect sites, but can reveal subtle variants of such lattice structure. High resolution spectra will show wavelength shifts caused by changes in local crystal fields, or couplings between impurities and other defects. Shifts caused by rare earth ions require high spectral resolution to be detected. Much larger shifts are seen for ions such as Mn and Cr [38]. These examples show that IL is helpful in mineral and impurity identification.

Non radiative return to the ground state can also occur through several processes. Thermal quenching is the reduction in luminescence intensity at higher temperatures. Another possibility to return to the ground state is by transfer of the excitation energy from an excited center $A^*$ to another center $B$. The energy transfer may be followed by emission from $B^*$ and species $A$ is then said to sensitize species $B$. However, $B^*$ may also decay non radiatively and in this case species $B$ is said to be a quencher of the $A$ emission. It can also happen that there is an overlap between an emission band and an allowed absorption band. For instance, $A^*$ decays radiatively and the emission band vanishes at the wavelengths where $B$ absorbs strongly. Moreover, there can be the energy transfer between two identical ions. In a lattice of $A$ ions there is no reason why the transfer should be limited to local effects. The excitation energy can go far from the site where the absorption took place. If this happens and the excitation energy reaches a quenching site, the luminescence will be quenched (concentration quenching).

The parameters that account for the luminescence efficiency of a material are the luminescence lifetime and the quantum yield. The quantum yield is the amount of emitted photons relative to the number of absorbed particles. Defining $k_r$ the emission rate of an excited state, and $k_{nr}$ the non-radiative decay rate to ground state, the quantum yield $Q$ can be expressed as follows:

$$Q = \frac{k_r}{k_r + k_{nr}}. \tag{3.1}$$

The lifetime is determined by the mean time an excited state takes to return to the ground state. It can be written as:

$$\tau = \frac{1}{k_r + k_{nr}}. \tag{3.2}$$

## 3.3 PHOTOMULTIPLIER TUBE

This paragraph recalls, for the sake of clarity and completeness, the main features of the photomultiplier tube (PMT) used in this thesis. As is well known, a photomultiplier tube consists of a photocathode and a series of dynodes placed in vacuum that are the amplification stages (Figure 3.2). A PMT can be considered as a current source, with the output current proportional to the detected light intensity. This device is capable of detecting individual photons. The detection of light is based on the photoelectric effect. Photons arriving in the front window of the PMT cause the ejection of electrons from the photocathode. Quantum efficiency is the number of photoelectrons emitted from the photocathode divided by the number of incident photons. The photocathode is held at a high negative potential, typically from -1000 to -2000 V. The dynodes are also held at negative potentials that decrease toward zero along the chain. Because of the potential difference between the photocathode and the first dynode, the ejected electrons (primary electrons) are accelerated and focused onto the first dynode where each electron will release a quantity of electrons through secondary emission. The secondary electrons are

focused and accelerated to the next dynode and this process is repeated, so an avalanche of secondary emissions increases the number of electrons until the anode. Each photoelectron from the photocathode results in a final burst of $10^4$ to $10^6$ electrons, which can be detected as individual pulses at the anode.

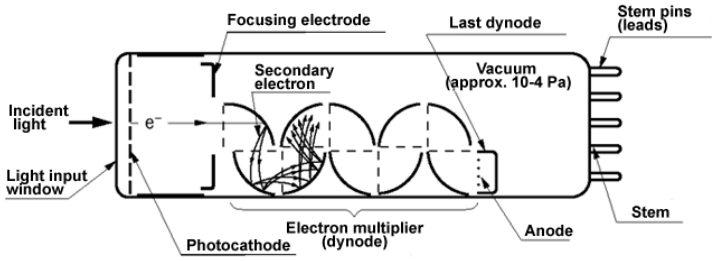


**Figure (3.2).** Schematic view of the main components of a PMT.

One of the important characteristics to be considered of PMTs is their spectral response. The sensitivity of a PMT depends upon the incident wavelength. The spectral response is determined by the type of transparent material used for the window, and the chemical composition of the photocathode. Another important feature is its time response. There are three main timing characteristics of PMTs: the transit time, the rise time and the transit time spread. The transit time is the time interval between the arrival of a photon at the cathode and the arrival of the amplified pulse at the anode. The rise time is the time required for the PMT anode signal to rise from 10 to 90 % of its final level. The transit time spread is determined by the transit time variation in the PMT, i.e., the scatter around the average transit time. The transit time spread results from the different geometric paths that the electrons can take from the photocathode to the anode. The photoelectrons can originate from different parts of the photocathode, or can have different trajectories from the same region of the photocathode, and also the electrons ejected from the dynodes can take slightly different geometric paths through the PMT.

## 3.4 TIME-RESOLVED MEASUREMENTS

During the years different types of luminescence centers have been studied by non time-resolved luminescence and identified in minerals, using photoluminescence, cathodoluminescence and X-ray luminescence techniques [39], [40], [41]. However, most emission spectra of minerals contain overlapping features of several types of luminescence centers. Some time-resolved luminescence techniques have been applied to minerals with interesting results, as for example, laser-induced time-resolved luminescence, which has shown that minerals have decay times ranging from nanoseconds up to milliseconds [42]. Time-resolved luminescence, specially the shape of the luminescence decay after the excitation is switched off, can provide information concerning static or dynamic processes inside the material. However, in spite of its powerful features, the literature for TRIBIL applied to the study of minerals, or any other material, is scarce.

The meaning of the decay time or lifetime, as briefly introduced previously, is related

to the transition probability of an excited state to the ground state. Considering a simple case of a material containing one type of emission center, if the material is excited with an "infinitely sharp" pulse, the population $n$ of emission centers in the excited state decays according to:

$$\frac{dn(t)}{dt} = (k_r + k_{nr})n(t), \tag{3.3}$$

where $n(t)$ is the number of excited centers at time $t$ after excitation, $k_r$ is the radiative decay rate and $k_{nr}$ the non radiative decay rate. Since the emission (radiative or non radiative) is a random event and each excited center has the same probability of emitting in a given period of time, assuming an initial population of luminescence centers in the excited state $n_0$, the solution of the equation is an exponential decay:

$$n(t) = n_0 e^{-t/\tau}. \tag{3.4}$$

When performing time-resolved luminescence measurements one is observing the luminescence intensity $I(t)$ versus time, which is given by the probability of return to the ground state with emission of a photon: $I(t) = k_r n(t)$. Substituting the number of excited centers for the luminescence intensity and integrating, the exponential expression for a single exponential decay is found:

$$I(t) = I_0 e^{-t/\tau}. \tag{3.5}$$

where $\tau = 1/(k_r + k_{nr})$ is the luminescence lifetime.

The average time a luminescence center remains in the excited state can be calculated by averaging t over the intensity decay:

$$\langle t \rangle = \frac{\int_0^\infty tI(t)dt}{\int_0^\infty I(t)dt} \tag{3.6}$$

Substituting equation 3.5 in equation 3.6 one finds that for a single exponential decay the average decay time is equal to the lifetime.

This is no more true for more complex decay laws. As an example, the return to the ground state can be delayed by subsequent stages through a temporary capture of free electrons and holes by shallow electron and hole traps (Figure 3.3). Shallow traps can capture electrons and holes and act as a reservoir supplying luminescence for a more or less lengthy time. The luminescence process can be conditioned by the temporary capture by traps, by the presence of traps with different depths and by possible repeated trappings (diffusion). This is why the time behavior of the decay of complex materials can be of an extremely complicated nature and cannot be described by simple expressions. For example, as to diffusion processes, the decay curve can be governed by a stretched exponential. If different impurities are involved the decay will take the shape of multi-exponentials. Instead, intrinsic luminescence, i.e., band-to-band recombination, usually shows a behavior of the type $I(t) = I_0/t^2$.

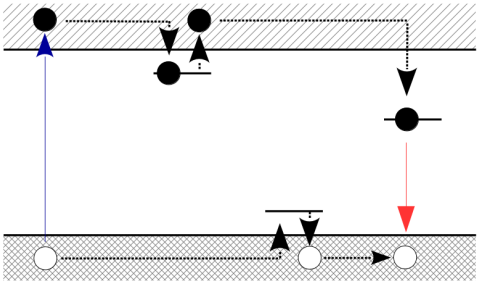

**Figure (3.3).** Diffusion process due to capture and giving off of electrons and holes by shallow traps.

Multiple processes can be present simultaneously. This work will not tackle a profound discussion about the mathematical treatment of these cases. However, it is possible to understand intuitively how different ways to probe a target can maximize or minimize the effects of such processes; for example, the case where two parallel recombination channels occur: bimolecular (intrinsic) recombination of free electron-hole pairs (band-to-band recombination) and monomolecular (extrinsic) recombination of impurity atoms. During weak excitations, basically all the absorbed energy is radiated in the form of monomolecular impurity luminescence. Thus bimolecular emission is substantially weaker than monomolecular emission. This can be understood considering that for weak excitations the density of electron-hole pairs is low and it is difficult for the electrons and holes to find one another to recombine. Almost all the photoelectrons are trapped at the impurity centers, which subsequently return to the ground state emitting an extrinsic luminescence photon. One can also think that for weak excitation condition not all impurity atoms are brought into the excited state. In other words, the number of all available events of impurity recombination is much larger than the density of excitation events per second. This makes it easy to understand what happens during strong excitation: in the latter case, bimolecular luminescence increases and swaps roles with monomolecular luminescence because the extrinsic radiative recombination channel becomes saturated.

What can be defined as weak and high excitation depends on the material. It is important also to point out that when working with high excitation, also new luminescence centers might appear. When analyzing experimental data, the decay shape can suggest a basic idea or a hint about the process behind the examined luminescence emission. However, the significance of the time equation that might reproduce the luminescence behavior should not be overestimated. For example, if a decay curve can be fitted by four exponentials it does not necessarily mean that four different luminescence centers are involved in the emission.

## 3.5 LUMINESCENCE LIFETIME MEASUREMENTS

Some techniques for time-resolved luminescence measurements, using for example ultrashort laser pulses, are well diffused in the scientific and industrial community. However, only few laboratories adopt the use of ion beams as the excitation source for their studies. In this section, a brief description of possible techniques to be used for TRIBIL will be given: the first is the one chosen for our work (the details of the setup will be presented

in the dedicated Chapter 4 of this thesis). The second is another technique also employed for TRIBIL measurements, reported in the literature from other laboratories.

### 3.5.1 Direct imaging of the luminescence response

The simplest set-up to study luminescence decay is by direct imaging of the luminescence response [43]. It consists of directly connecting the output of a single-channel detector, usually a photomultiplier, to a sampling device such as an oscilloscope or an analog-to-digital converter. Obviously, in order to record, in this way, the decay of the luminescence in time, either a continuous excitation beam must be chopped or a excitation source directly supplying sufficiently short pulses must be used. Since the character of luminescence decay may be strongly dependent on the emission wavelength, the decay curves $i_\lambda(t)$ of a quasi-monochromatic luminescence signal are usually measured after inserting a monochromator or at least narrow-band interference filters in front of the detector. The next step consists in analysing the measured curves $i_\lambda(t)$.

Although the method of direct decay imaging looks very simple in principle, its practical implementation challenges the quality of the instrumentation and the experimenter knowledge of the limits of applicability of the method: the direct measurement of the luminescence response may be easy to apply only for studies of relatively slow decays, $\tau \geq 0.1 - 1\mu s$.

The experimentally determined luminescence time response $R_\lambda(t)$ is given by a convolution of the actual time response $i_\lambda(t)$ (i.e. the luminescence response to an infinitely short excitation pulse) with the temporal profile of the excitation pulse $L(t)$ measured by the same detection system as that used to obtain $R_\lambda(t)$:

$$R_\lambda(t) = \int_0^t L(t - t')i_\lambda(t')dt' \tag{3.7}$$

If the duration of the excitation pulse $L(t)$ happens to be comparable to the decay times of the luminescence response $i_\lambda(t)$ the actual luminescence response must be therefore determined via deconvolution of the above relation.

### 3.5.2 Time-Correlated Photon Counting

Time-correlated photon counting is based on the statistical character of luminescence photon emission [44], [45]. To perform such an experiment, two requirements must be satisfied: the luminescence intensity must be very low to enable the arrival of single photon to be recorded; a high number of photons must be detected to obtain conclusive statistics. This means that the accumulation of the entire rise-decay curve may take from minutes up to hours. Basically, the arrival times of single photons are recorded (e.g., the time when a pulse appears at a photomultiplier output) considering the moment when the excitation pulse was emitted as the time origin $t = 0$.

The essential part of this apparatus is a time-to-voltage converter. The converter is initiated by the excitation pulse at time $t = 0$ (start pulse) and begins to generate a DC voltage linearly increasing in time. The voltage rise is stopped by a stop pulse coming

from the photomultiplier. The resulting voltage amplitude is proportional to the time decay between $t = 0$ and the stop pulse. This method is mainly applied to the detection of luminescence kinetics at the time-scale of $\approx 10^{-6} - 10^{-10}$ s.

In the literature, single ion and single photon coincidence techniques can be found [44], [46], [45], [47], where they are used for both the reconstruction of the luminescence decay curve and the luminescence spectra resolved in time. The latter consists in registering the emission spectra after predefined delays after the excitation event. In few words, these experiments use a monochromator to select a wavelength range in which photons are detected by a PMT or a MCP (Microchannel Plate)-PMT. The start signal generated by the output of the photon detector is sent to a time-to-amplitude converter, as well as the stop signal (properly delayed) given by an ion detector positioned in the beam path. By recording the intensity of light detected as a function of the time difference between start and stop signal it is possible to reconstruct the rise-decay curve.

## 3.6 LAPIS LAZULI

Since LABEC has a long reputation on the study of works of art, as well as archaeology, it seemed natural to apply the new setup for TRIBIL to the provenance study of lapis lazuli. This stone is a very heterogeneous material, as it will be presented in this Chapter. Working with lapis lazuli is not a straightforward task, since as deep as one goes into acquiring information about this stone, it reveals itself more and more complex. But it is this complexity that made and still makes several physicists, geologists, archaeologists and professionals of other areas in science to study this stone that has fascinated ancient civilizations to the point it was considered to have religious meaning [48].

Here, a brief description of this stone from the mineralogical and geological point of view will be given. A summary of previous works applied to the study of lapis lazuli will be presented. Among several techniques applied to the provenance study of lapis lazuli, a focus will be given to the ones concerning IBA techniques, specially IBIL. Finally, the raw samples used in this work will be presented.

### 3.6.1 Mineralogy and Geology

The lapis lazuli is a stone of very variable composition, presenting different shades of blue with white and golden veins (Figure 3.4). Its dark blue color comes from lazurite, which is its main mineral constituent with chemical formula $(Na,Ca)_8(AlSiO_4)_6(SO_4,Cl,S)_2$. The $SO_4$, S, and Cl quantities are variable. Lazurite is found in marble as a product of contact metamorphism. Other accessory minerals can be present such as K-feldspars, calcite ($CaCO_3$), wollastonite ($CaSiO_3$), and diopside ($MgCaSi_2O_6$). It usually also contains grains of pyrite ($FeS_2$) which gives the rock golden veins or spots [49]. The colour of lapis lazuli can vary from intense marine blue to violet blue, but lighter blue and greenish varieties are also sometimes found.

Lapis lazuli has a long history as an ornamental stone. It has been found in artifacts of some of the oldest known civilizations in the Middle East, Asia and Europe. Evidence

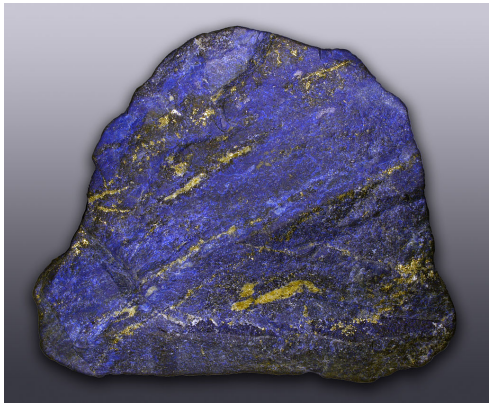

**Figure (3.4).** High contrast view of a lapis lazuli stone showing its different shades of blue, crossed by white and golden veins.

of its first use comes from excavations at the Indus Valley Civilization (what today is northeast Afghanistan, Pakistan and northwest India), where a lapis lazuli pearl was found on what was probably the pendant of a necklace, dated from about 7000 B.C. [48] on the basis of the archaeological context. Further discoveries show that its trade was organized since the beginnings of the urban civilizations in the Ancient East. Lapis Lazuli is documented to have been diffused throughout Mesopotamia, Iran, Central Asia and Egypt by the end of the fourth millennium B.C. It was used for jewelry and ritual objects, and as a material for inlays, seals, and tablets. One of the most impressive objects found in Mesopotamia is the Standard of Ur (Figure 3.5), approximately 4500 years old, found in the tombs of Ur (located in what is today lower Iraq). In Egypt, objects in lapis lazuli were found in ancient tombs dating from 3100 B.C. Tutankhamun's mummy has eyebrows and areas around the eyes that are inlaid with lapis lazuli [50]. It was also used in Egypt in the form of powder in cosmetics, as eye shadow, and as a pigment in paintings. From Egypt the use of lapis lazuli expands to the Mediterranean basin, reaching ancient Crete, Greece and Italy, as well as the Extreme Orient with objects found in China [51]. In the Middle Ages lapis lazuli fell almost in disuse being however still sometimes employed as a pigment for illuminations in manuscripts. It takes again a more extensive place in the Renaissance being used both as a pigment ("ultramarine") for paintings and in the decoration of sculptures like cups, bowls and urns, until when an inexpensive synthetic substitute was developed by J. B. Guimet in 1826 [52]. The historical importance of its trade is due to the fact that lapis lazuli is a rare stone coming only from a few deposits on Earth.

Lapis lazuli is a rare stone owing to the geological conditions in which it can be formed. Georgina Herrmann (1968) [53] discusses the numerous possible sources of this stone traded in Ancient East. In her work she considered the Badakhshan region (today Afghanistan), the Pamir Mountain range in Tajikistan, Lake Baikal in Russia, Iran, and Egypt. Although there is historically documented evidence for the existence of a lapis lazuli source in Iran and Egypt, a physical evidence is still nonexistent [53], [54]. The Badakhshan source is the most widely accepted out of all, as the main source of lapis lazuli in the Ancient East. Hermann arrived at this conclusion considering that: the

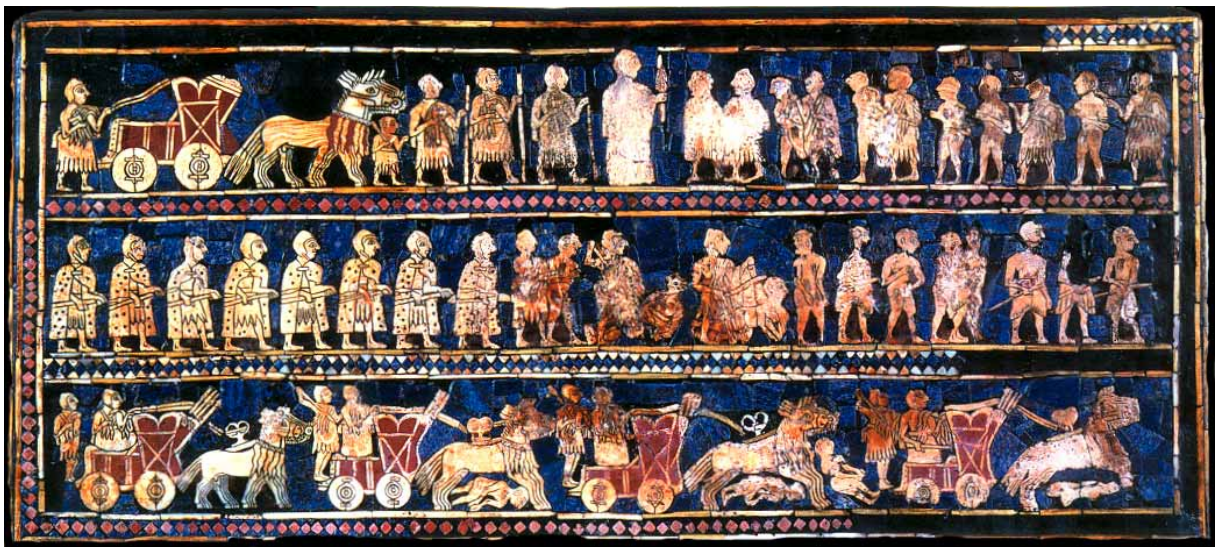

**Figure (3.5).** Photograph of one side of the so called Standard of Ur: object made with lapis lazuli found in Mesopotamia, dated to be approximately 4500 years old. Its dimensions are 21.6 cm x 49.5 cm.

Pamir source, although not much further away from Mesopotamia than Badakhshan, is of very difficult access, being located at 5 km up in the mountain next to a glacier; the Lake Baikal source is far from Mesopotamia and the lapis in the mines is of poor quality.

In Chile, the Coquimbo Region is the only known source of lapis lazuli. Although reference is sometimes made to another Chilean deposit at Vicuña Mackenna Mountain near Antofagasta [55], [56], this material has been identified as another stone with similar aspect, dumortierite, by Canut de Bon in 1991. The Chilean lapis lazuli is considered in this work because of its possible use in ancient times in South America. There are also other quarries like the Italian Mountains of Colorado and Cascade Canyon in California, USA [57]; Brazil [58]; and others. These are not considered in this work since they are exploited only in recent periods.

### 3.6.2 Provenance Studies

Due to its heterogeneous nature, identifying the provenance of lapis lazuli is a challenging task. There are several studies in the literature focused on geo-sourcing through the identification of distinguishable molecular markers in different natural lapis lazuli stones and pigments. Other studies focused on distinguishing between natural and synthetic origins. It is important to take into account that in a complex material like lapis lazuli it is unlikely that only one marker or one technique can be sufficient to unequivocally distinguish among different provenances. Moreover, some markers are "stronger" because they are a peculiar characteristic of a provenance, while some others can just give an indication whether a sample can or cannot come from a certain provenance. For example, the appearance of an element can indicate a certain origin, but the lack of this element is not sufficient to identify any origin. The studies that focus on finding "markers" to distinguish lapis lazuli from different origins are usually limited by two main factors. One is that the number of samples analyzed is small, which is due both to the preciousness and rarity of the material, and also to the localization of the mines, sited in impervious

places very difficult to reach. The other is that there is a lack of precise geographical information for many specimens archived in museums or private collections, and this fact makes most of them inadequate to be a safe reference for a provenance study [59], [60], [61].

Various approaches have been used to identify chemical fingerprints for lapis lazuli from different regions of the world [62], [63], [64], [65], [66]. The literature from earlier works is vast but not always easily accessible. Here a few examples of the first studies that tried to find markers that can discriminate lapis lazuli from different origins will be given.

Starting from the late 60's, Hermann in 1968 published that using Optical Microscopy (OM), X-Ray Fluorescence (XRF) and Optical Spectroscopy, it is not possible to distinguish between Afghan and Siberian lapis lazuli. Keisch in 1972 claimed that by performing Isotope Mass Spectrometry it was possible to distinguish Afghan lapis lazuli from artificial ultramarine, Chilean and Siberian provenances thanks to a difference on the isotope ratio of sulphur ($S^{32}/S^{34}$). In the late 80's, Borelli [60] and Cipriani [61] published their work based on OM on thin sections, Scanning Electron Microscope with Energy Dispersive X-ray Spectrometry (SEM-EDX) and X-Ray Diffraction (XRD). Their work resulted on a mineralogical characterization of the samples, recognizing all the different minerals present in a rock and an evaluation of how diffuse they are in the sample. This analysis shows for the first time a distinctive marker for the Chilean provenance: the presence of wollastonite as accessory mineral, while both in the Afghan and in the Siberian lapis lazuli it is replaced by diopside. Focusing only on the mineral lazurite and performing SEM-EDX, they also showed that Cl is not detectable in Chilean and Afghan lazurite, but it was detected although in low concentration in Siberian ones. Next, Atomic Absorption Spectroscopy performed by Casanova in 1989 showed an indication that samples from Ural Mountains and Afghanistan contained a larger concentration of Ba and Sr than those from Pamir Mountains and Pakistan. Fourier Transform Infrared Spectroscopy (FTIR) has also been applied, and the proposed marker is an infrared band at about 2340 $cm^{-1}$ that was found in lapis lazuli of Afghan origin [67]. More recently, Zöldföldi applied Prompt Gamma Ray Activation Analysis (PGAA) to the origin study of lapis lazuli [68] and showed that, when considering the concentration of the elements Cl and S, samples from Afghanistan and Lake Baikal have low Cl/Si ratios while the samples from Chile and Ural show higher ones, which might appear in partial contradiction with the above quoted works by Borelli and Cipriani. Still in the work by Zöldföldi, samples from Afghanistan are reported to show higher S/Si ratio than those from Lake Baikal.

Although with some results that suggest useful markers, the techniques mentioned above are usually applied in a destructive or invasive manner. More specifically, either a sample has to be picked up from the object of interest or even transformed in the form of powder. When considering works of art, one has to keep in mind that, because they are valuable, non-destructive investigations are preferable if not the only option. IBA techniques not only are non-destructive and non-invasive, but they also provide the possibility for in air measurements. Ion beam analysis works applied to the study of lapis

lazuli have been published over the last few years. In the following a summary of the works published in the last years that are more relevant for this thesis will be given.

A micro-PIXE study focused on lazurite and diopside [69] showed that Chilean stones present a lower quantity of K in lazurite with respect to the other provenances. Afghan samples present a higher quantity of Ti, V and Cr in diopside. Concerning lazurite, stones from Afghanistan showed a higher quantity of K and lower quantity of S. Lapis lazuli from Taijikistan have a higher quantity of As in lazurite. The presence of Ba in in some inclusions of lazurite, and higher quantities of Sr in lazurite in Siberian samples, were confirmed. Instead, when focusing on pyrite, another study [70] showed that pyrite contains high levels of Ni in Afghan lapis lazuli. In samples from Tajikistan, the results showed high quantities of Ca. The element Se was found in pyrite in Chilean stones and Siberian samples contain only Ni as trace element in pyrite.

Several groups also applied IBIL to the provenance questions [3], [71],[72]. A broad band in the far red region, around 780 nm, was seen by Calusi [3] in some Afghan samples, and was attributed to Fe-related impurities, already detected by cathodoluminescence [73]. Instead, a band around 750 nm was reported by [71] and attributed to the presence of $Ti^{3+}$ impurities. The band around 450 nm was seen in all stones by all the authors, and is usually correlated to the silicate matrix, seen also by photoluminescence [74], [75], [76]. An emission around 580 nm seen from the Asian samples, which also appears in cathodoluminescence (CL) measurements [77], is usually attributed to $Mn^{2+}$ activation of diopside. The strongest markers found, which seem to discriminate the Chilean lapis lazuli from the Asian ones, are a yellow band around 560 nm and an orange band around 620 nm. They can be ascribed to the mineral phase wollastonite, whose luminescence is also activated by $Mn^{2+}$ ions. The fact that Chilean lapis lazuli is distinguished by the presence of wollastonite was already reported by the destructive techniques mentioned above, as well as the fact that Asian samples, instead, are characterized by the mineral phase diopside.

Altogether, the works mentioned above provided indeed some indications about the origin of lapis lazuli. What defines a strong marker however is the fact that it is always observed, without sample dependence, in one sample origin and never in the others. With this in mind, the only strong marker found so far seems to be the bands at about 560 and 620 nm in Chilean lapis lazuli, which discriminate this provenance from the Asian samples. Since other strong markers were not yet found to discriminate other origins, we thought it would be worth to test the powerful TRIBIL technique to further investigate the origin of lapis lazuli.

### 3.6.3 The Lapis lazuli Samples

Lapis lazuli samples used in this work are from Afghanistan (three samples), Chile (three samples), Myanmar (two samples), Taijikistan (two samples) and Siberia (four samples, two from the south and two from the north of the Baikal lake). The stones from the first three provenances are from the Istituto Nazionale di Fisica Nucleare (INFN) of Turin. The

samples from Taijikistan and Siberia are from the Museum of Natural History of Florence. These are raw samples where one side was polished to be used for IBA measurements. In the following, photos of the samples will be shown in Figures 3.6-3.10.

It is possible to see that the samples are significantly different among them, also visually. Dark lines (golden) that can be seen in the pictures are pyrite inclusions. Each sample is named in a way that the country of origin comes first and a catalog number secondly, for example, AFG11, where AFG corresponds to Afghanistan. This is how the stones will be recalled along the thesis.

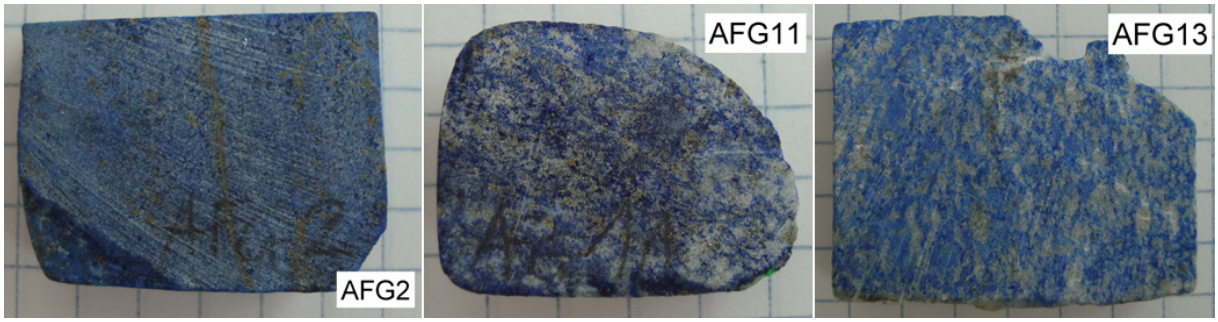


**Figure (3.6).** Samples from Afghanistan used in this work, labeled as: AFG2 (left), AFG11 (center), and AFG13 (right).

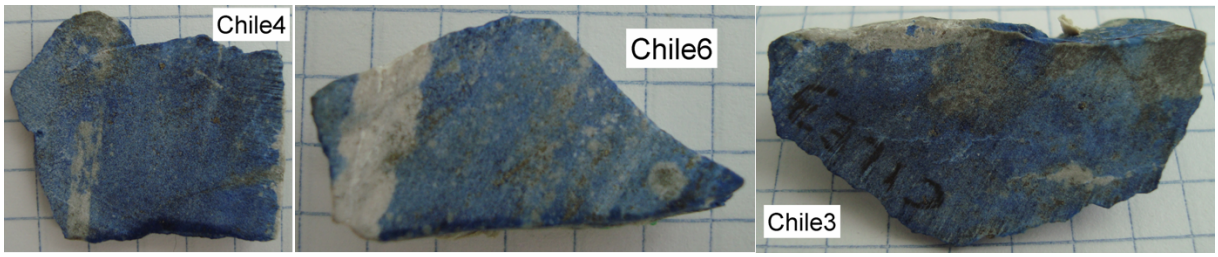


**Figure (3.7).** Samples from Chile used in this work, labeled as: CHILE3 (left), CHILE4 (center), and CHILE6 (right).

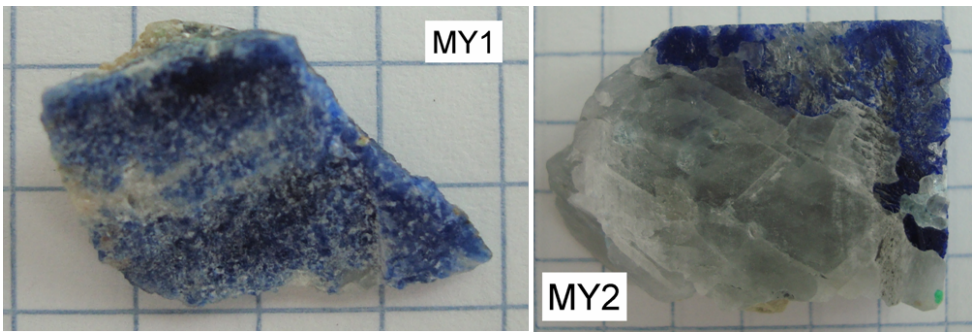


**Figure (3.8).** Samples from Myanmar used in this work, labeled as: MY1 (left), and MY2(right).

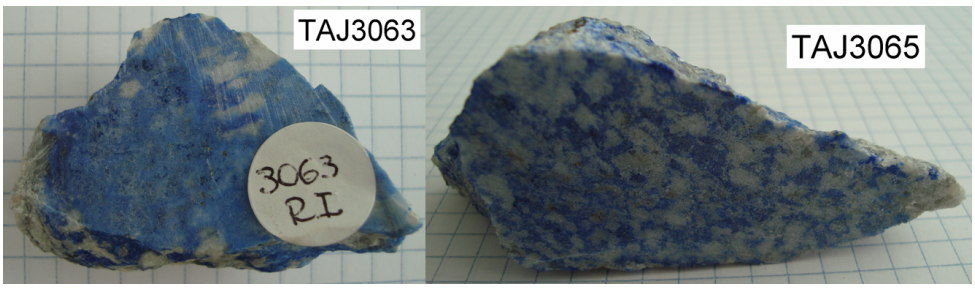


**Figure (3.9).** Samples from Tajikistan used in this work, labeled as: TAJ3063 (left), and TAJ3065 (right).

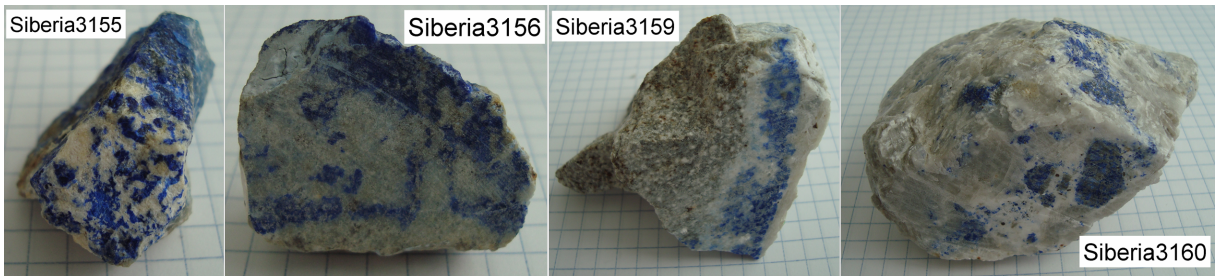


**Figure (3.10).** Samples from Siberia used in this work, labeled as: SIBERIA3155 (left), SIBERIA3156 (center/left), SIBERIA3159 (center/right), and SIBERIA3160 (right).

# CHAPTER 4

# INSTRUMENTS AND METHODS

In this chapter the experimental setup will be described regarding the instrumentation placed inside the measurement chamber (detectors, diagnostic elements), the acquisition system, and the data analysis method; the latter two have been developed on purpose during my PhD work. This was the first time a setup was installed for time-resolved measurements at LABEC of a material with unknown timing response (as was the case for the lapis lazuli samples, which were studied as a the first application of the overall system, extensively presented in the second part of this dissertation). In order to probe different features of the materials under investigation different measurements were performed changing the irradiation parameters, which will also be described in this chapter. Besides the materials studied for the specific application, standard $CdWO_4$ and BC-408 scintillators with known luminescence decay times were also irradiated to characterize the system and check its performance. These two specific scintillators were chosen because of their largely different timing response to irradiation: indeed, $CdWO_4$ is characterized by long luminescence decay times and BC-408 by much faster decay times.

## 4.1 MEASUREMENT SETUP

In this section the experimental setup inside the vacuum measurement chamber of DEFEL will be described. Also, a basic description of the beam transport in the DEFEL beamline, until inside the chamber, will be given. Basically, the setup configuration consisted of a vacuum chamber, where the samples to be investigated are placed in front of the beam path; a photomultiplier tube, the characteristics of which will be described in the following; an optical fiber to collect the luminescent signal from the sample and send it to a spectrometer outside the chamber through appropriate vacuum feedthroughs; and diagnostic elements (Faraday cup, a quartz and a camera). Here, a detailed description of each of these devices and their purposes will be given.

The samples to be analysed were polished and placed in a sample holder in a way that their polished sides faced the direction of the incident beam. The sample holder is a sort of shelf allocating more samples: to avoid breaking the vacuum for each measurement session, it is attached to motorized linear stages inside the measurement chamber. These linear stages can be remotely controlled and allow us the movement of the shelf in the x and y directions in order to place the different samples on the desired position for their

analysis. The positions can be memorized so that it is possible to accurately return to previous measurement positions.

For the time-resolved measurement a photomultiplier tube (PMT) from Electron Tubes / 9256KB was used. The PMT was placed facing the samples at an angle of approximately 135° to the beam direction (Figure 4.1). Some of the important features to consider on a phototube, such as time response, wavelength range and gain were already presented in Chapter 1. Since the application of TRIBIL to lapis lazuli was being performed for the first time, information such as the intensity of light one could expect was not known a priori. The decision to place the PMT inside the measurement chamber comes with the fact that from the first attempts we made, we realized that it was not possible to collect enough light with an usual optical fiber (600 $\mu$m diameter) for time resolved measurements: the light had too low an intensity. For this reason, a large collection area was needed. The PMT chosen for the measurements has an active diameter of 46 mm. The model used in this work has a high gain of 0.5x10$^6$ A/lm.

The choice of the PMT was also suggested by the specific application to lapis lazuli that we had in mind. For example, since among the luminescence characteristics of lapis lazuli that are well known are the main emission bands of its composing minerals, around 450, 560 and 580 nm [3], it was important for our purposes that the spectral range of the overall detection system covered these bands. The PMT Electron Tubes / 9256KB spectral range is 290-680 nm, with enhanced green sensitivity. As it can be seen in Figure 4.2, at the peak, around 400 nm, its quantum efficiency is of 28%. The timing responses, too, are optimal for time-resolved measurements. Considering a delta pulse, the rise time of the PMT signal is 4 ns, the FWHM of the signal is 6.5 ns and the transit time is 40 ns.

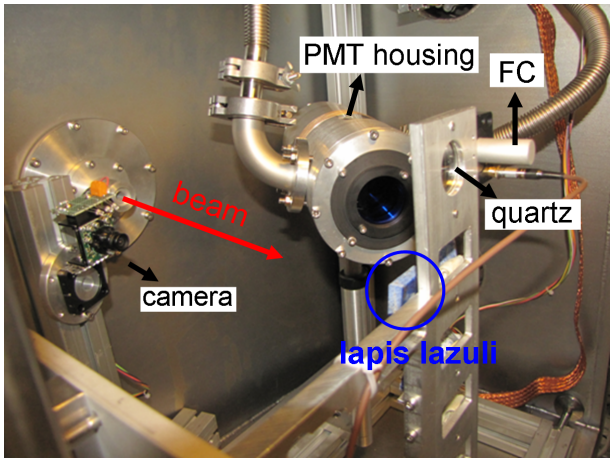


**Figure (4.1).** Experimental setup inside the measurement chamber used for the experiments performed with lapis lazuli.

In-vacuum measurement at the DEFEL chamber were usually performed at a pressure of $10^{-4}$-$10^{-5}$ mbar. To perform in-vacuum measurements, the PMT was housed in a vacuum-tight box made of aluminum. Two leak-tight ducts connected the PMT box to ambient pressure by a flange in the wall of the measurement chamber. A continuous flow of air at ambient temperature was maintained through the ducts to cool the PMT and keep it at working temperature. The power and signal cables were accessible by passing

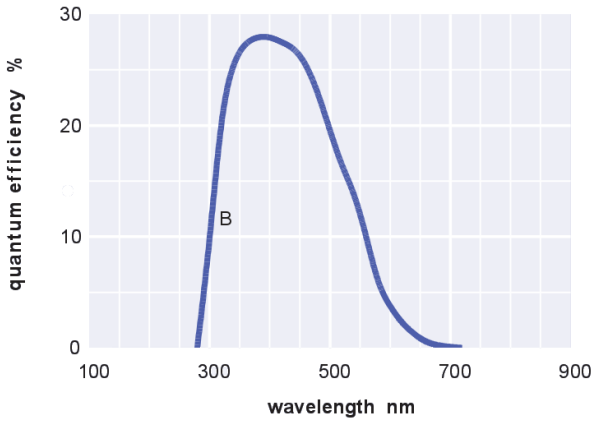


**Figure (4.2).** PMT spectral response curve.

them through one of the ducts. Because of the dimensions of the PMT housing and the geometry of the chamber, the center of the PMT window distance to the samples was around 5 cm. In order to perform wavelength discrimination, it was possible to place optical filters in front of the PMT window by a filter holder that was fixed in the PMT aluminum housing.

Measurements of steady-state luminescence (i.e. under a continuous beam) were also performed, where the collection of the luminescence signal was made by placing an optical fiber (Ocean Optics/QP600-UV-VIS) facing the samples. Since the measurements were carried out while time-resolved measurements were also being performed, the optical fiber was placed at a distance of approximately 20 cm from the stones. This large distance is a consequence of the measurement chamber internal geometry. Also, in this way, the PMT could be positioned as close as possible to the samples. The optical fiber was sent to a dedicated flange, where it was connected to another optical fiber outside the in-vacuum measurement chamber. The other extremity of the external optical fiber was coupled to a spectrometer (Ocean Optics/USB2000+).

Next, the alignment procedure and the positioning of the several elements inside the chamber will be described. A key element in the setup is a quartz placed in another position on the same sample holder as the target. The center of the beamline can be known thanks to a fixed laser outside the chamber that is permanently installed to point to the theoretical center of the beamline. At the end of the beam transport, the beam is deflected so as to coincide with the laser hitting point. The first step, once the sample holder had been placed, was to take the position of the quartz corresponding to when the laser hits its center. When the position is taken, a mark is made on a computer screen of the quartz center. If desired, with this mark it is then possible to take the samples positions corresponding to the areas to be irradiated. This is done by moving the linear stages until the desired area is in coincidence to the screen mark, and then the positions are memorized.

The alignment of the PMT is important so that the collection of light is optimized. This procedure was also done by the use of the quartz. With the quartz in the center, another laser pointer is placed on top of the PMT housing, in such a way that the laser

beam is parallel to the PMT axis. The PMT is rotated until the laser points to the center of the quartz. Finally, the PMT is translated vertically by a distance equal to the difference between its axis and the laser beam. This procedure is performed attempting to place the PMT as close as possible to the samples, obviously taking care of not "screening" the beam path or preventing the movement of the linear stages. The alignment of the optical fiber was done similarly, also with the use of a laser pointer.

The procedure of transporting the beam will now be presented in a basic way so the reader can visualize the total work behind the measurements. After closing the measurement chamber and the vacuum has reached its operating value, one needs to ensure that the beam is able to enter the chamber. Not only, the beam must hit the center of the quartz when this is positioned at the center of the beamline. For these purposes, diagnostic elements are installed inside the measurement chamber. A camera is positioned in such a way that it has a clear view of the quartz when placed in the beam line center position. Besides, a Faraday cup is also installed in the motorized stages. After the beam has been transported until the last Faraday cup of the DEFEL beamline, as described in the previous Chapter, the beam is allowed to pass through a final diagnostic station in a continuous mode. The final slits are usually kept wide open so one is certain the beam is not being blocked. With the quartz center positioned on the beamline axis, it is possible to center the beam by deflecting it using the second steerers of the DEFEL beamline. Once the beam has been centered, the final slits must be closed to an aperture that depends on the requirements of the experiment.

In order to monitor the width adjustment procedure of the final slits, the Faraday cup is positioned in the beam path. The final slits of the DEFEL beamline have four independent movements, two in the horizontal and two in the vertical directions. To be sure that the center of the beam is being selected, each of the movements is operated at a time. By attempting to close in a symmetrical manner while monitoring the beam current, it is possible to select the center of the beam. Of course, after this is performed it is necessary to return the quartz to its position in the beam path to verify that the beam is still centered.

Again, the procedure of transporting the beam inside the measurement chamber was here presented in a basic way. Often, it is not straightforward, and one needs to operate by successive approximations, using the deflection elements more than one time or even returning to the beam transport in the first part of the beamline, or to the low energy side of the accelerator.

## 4.2 ACQUISITION SYSTEM

The time-resolved measurements performed for this work are based on the idea of direct "imaging" of the luminescence signal. Each time a bunch of particles hits the luminescent target, a light emission occurs. The emission has a certain duration and a decay shape that evolves with time, even after the beam bunch duration. Each time photons are detected and converted into secondary electrons, the PMT gives a signal at its output

that is proportional to the amount of photons detected. The PMT works in a way that its output reproduces the evolution in time of the luminescence emission. With this in mind, the anode output of the PMT detector was directly digitized as representative of the trend of luminescence vs. time.

The whole acquisition system is controlled by a VMEbus (VersaModular Eurocard bus). Only a brief description of the VMEbus system will be given without entering into details since it is a known standard, certainly not developed as a part of the work of this thesis. It is a high-speed and high-performance bus system with a powerful interrupt management and multiprocessor capability. The advantages of the VMEbus are that it is able to provide speed of operation combined with flexibility and accessibility for development and also for running embedded applications. It is based on a scalable and flexible computer backplane bus interface (Figure 4.3). The backplane consists of a printed circuit board on which the card connectors are located. The cards or modules are the printed circuit boards that carry the required hardware to implement the functionality required on the system. The modules are accessible by assigning each of them a different address.

The VME controller, placed on the first slot of the VME (black slot in Figure 4.3) is an Emerson CPU (model 7100) equipped with 2 Gigabit Ethernet controllers. Every time the VME controller is switched on the operational system, which has as one of its functions the CPU memory management, is requested and loaded via TFTP (Trivial File Transfer Protocol) through an Ethernet connection. A NFS (Network File System) server is used to record data during measurements through an Ethernet connection with the VME for online analysis, and it can be accessed by the user computer through another Ethernet connection in order to display data in real time avoiding traffic on data link.

The analog-to-digital converter (ADC) used in this work is a CAEN/V1720 VME module. The ADC can be programmed by giving its base address to the CPU. Analog-to-digital converters can be of two types: peak sensing or sampling ADCs. In the former, the maximum of a voltage signal is digitized. In this work, instead, the latter type was used, which produces many sampled points for each detector signal. Here, "sampled point", as well as the word sample used in the following, refers to a "piece" of the analog signal from the PMT. Important features of the CAEN/V1720 include: resolution of 12 bit; sampling rate of 250 MS/s, i.e., the ADC digitizes one sample every 4 ns; full scale voltage range of 2 Vpp. Thus, its least significant bit (LSB), i.e., minimum change in voltage required to guarantee a change in the output code level is LSB=$2V/2^{12}$ which is 0.488 mV.

The digitizer functions are set by a program that I wrote in C++, which is loaded in the VME-CPU. Each of the functions is accessible by a specific address in the memory, for example, choosing the input channel to be used or the sign of the signal to be digitized. Each function can be programmed by setting the bits of its address to "0" or "1". The ADC has several functions and I will now describe the most relevant ones that have been used for the data acquisition.

The acquisition trigger was set to be external. This was chosen so that only the signals in coincidence with the arrival of the bunch of ions on the target would be digitized.

**Figure (4.3).** On the left the VME crate and on the right the ADC used in this work.

For this purpose, the monitor signal shown in the electronics in Figure 2.1 was taken. The monitor output gives a pulse at each deflector or predeflector transition from off to on mode, and vice-versa. The monitor signal is sent to a discriminator module, which produces a NIM signal each time the signal amplitude exceeds a given threshold. A negative discriminator, i.e., a discriminator that accepts only negative signals is used, so that only the first transition from off to on mode is considered. Figure 4.4 shows a complete scheme of the acquisition setup.

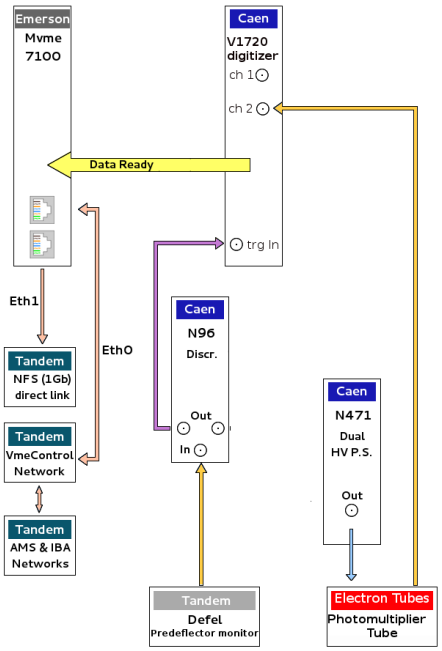


**Figure (4.4).** Scheme of the acquisition system.

Concerning time-resolved measurements, the digitization time window length is an important parameter to set, for the entire signal to be digitized. But one has also to keep in mind that the wider is the time window the larger is the time the ADC takes to process the data and store it. A compromise must be chosen to optimize the measurement time without losing important parts of the signal. V1720 has in its register several different buffer lengths (the window length can be set from approximately 4 $\mu$s to 4 ms). Of course,

if there is the interest in digitizing a signal that lasts more than 4 ms, one can digitize different parts of the signal separately and add them together in further data processing. In this thesis different time windows were used and they will be specified in the results section.

Once chosen the time window, the PostTriggerSettings were adjusted (Figure 4.5). This function requires the number of samples to memorize after the trigger signal. It can also be thought in terms of dividing the whole time window in two parts, chosing the fractions to digitize prior to and after the trigger (the former, in order to know the "baseline" over which the beam-induced luminescence signal rises).

For a better understanding a brief description of how the buffer works will now be given. The data stream is continuously written in a circular memory buffer. When a trigger occurs, the Field Programmable Gate Array (FPGA) writes further N samples and freezes the buffer that then can be read via VME. The acquisition can continue with no dead-time in a new buffer. In this work, the PostTriggerSettings were set in order to have enough samples for the baseline calculations before the trigger, without losing important signal information. For that, the time window must be chosen a little longer than the actual signal duration. For each trigger a waveform is digitized and saved in a binary file for post processing.

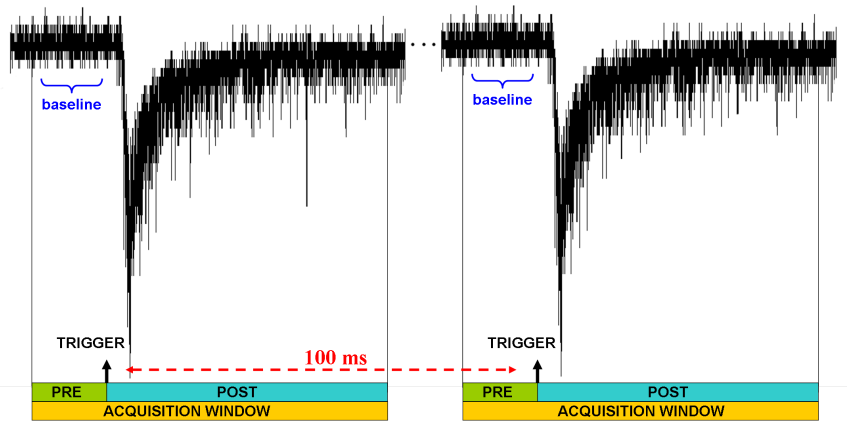


**Figure (4.5).** Representation of how the PostTriggerSettings function works. Only the digitized samples that are within the acquisition window are saved for analysis. This function is used to allow one to control the number of samples available for the baseline calculation.

## 4.3 IRRADIATIONS

For the application to the provenance study of lapis lazuli (see Chapter 5 for a discussion of the obtained results) irradiations were performed in several types of configuration in the attempt to find differences between stones from different origins that would not be seen otherwise. Protons of 3 MeV (produced by the Duoplasmatron source of the Tandetron) and carbon ions of 10 MeV (by the sputtering source) were used.

In order to know the ions range in lapis lazuli, and the possible origin of the luminescence seen from the stones, SRIM calculations were performed considering the two main minerals in lapis lazuli that are lazurite and diopside. Figure 4.6 shows the results of

these simulations. As it is expected, 3 MeV protons have a much longer range inside the minerals (≈90 $\mu$m for lazurite and ≈60 $\mu$m for diopside) than 10 MeV carbon ions (≈6 $\mu$m for both lazurite and diopside).

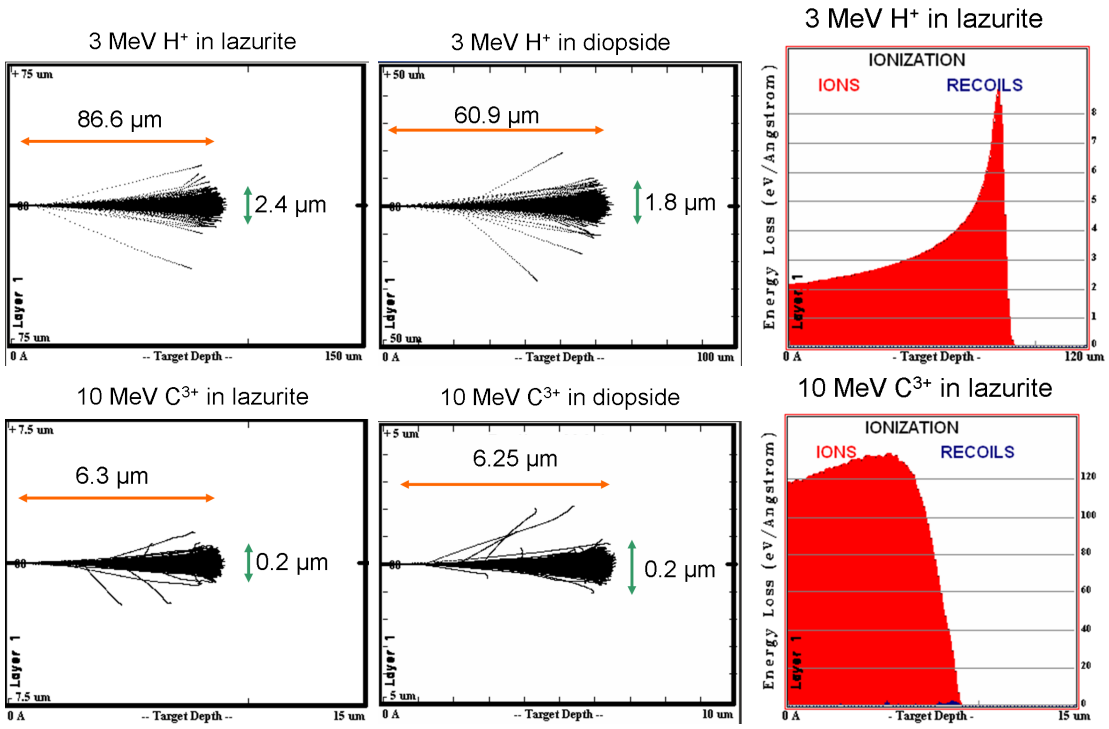


**Figure (4.6).** Ions ranges of 3 MeV protons and 10 MeV $C^{3+}$ in lazurite and diopside.

As it was mentioned in Chapter 3, the emission is often dependent on dose and dose rate. The competition between faster and longer decay times depends on the irradiation time. Longer irradiation times emphasize longer decay times, while short pulse duration emphasizes the shorter components. Here, the different setups used in this work will be described.

In order to characterize the system and comprehend the meaning of the results two standard scintillators with different known lifetimes were irradiated under different conditions prior to the measurements on the lapis lazuli samples. Measurements were performed with 3 MeV protons (using several settings of DEFEL) on $CdWO_4$ and BC-408 (Bicron) scintillators. $CdWO_4$ scintillators are known to have rather long decays: lifetimes of 0.4, 0.9, 6 and 14 $\mu$s had been observed e.g. by Fazzini [78]. Other authors had identified some of these lifetimes [79]. Instead, the commercially available BC-408 scintillator is known to have a fast main component of 2.1 ns. Irradiations tests consisted in irradiating the scintillators with different beam currents and using both predeflector and deflector, as well as only the predeflector, in order to change the irradiation time. The parameters used in each irradiation will be reported along with the results in the next chapter.

Wavelength discrimination was achieved by placing optical filters in front of the PMT window in some of the irradiation sets. The filters used had a large bandwidth (about 100 nm). Narrower-band filters were also checked, but they were not eventually adopted because in the configuration presented in this work a large amount of light was lost and the statistics was insufficient to draw any conclusion.

Concerning the beam features, it is important to point out that the beam diameter was of approximately 3 mm. As it was already mentioned, DEFEL was initially built to deliver a beam that might be as small as hundreds of micrometers when the slits aperture was kept small, and few ions per bunch if the beam current had low intensity. In the case of this application to lapis lazuli, there was however the need for high beam current intensity and small beam size simultaneously. Unfortunately, in the DEFEL line it is difficult to focus an intense beam to very small dimensions, and the only practical way to have sufficient intensity per bunch is to keep a large slit aperture. The drawback, with such large beam when irradiating a sample like lapis lazuli, is that it is most probable that the luminescent emission is a result of the decay of different minerals. In contrast to what has been performed in previous works using the micro beamline, with DEFEL in the present configuration it is therefore not possible to safely select a single mineral phase to be irradiated. Nevertheless, the waveforms acquired can be considered as an average emission of the material and be used to look for differences among them.

The beam pulse frequency periodicity can be adjusted by changing the frequency to which the deflectors make their transition from off to on mode. In all sets of irradiation, the pulse frequency was set to 10 Hz, which means every 100 ms a bunch of particles hit the target and a waveform was digitized. It was verified that this time period was large enough so the luminescence decays would not overlap resulting in the start of a new irradiation while there was still significant emission from the previous one. The reason to set a pulse frequency and not irradiate the sample with single shots comes with the fact that more than one waveform must be acquired per irradiated area when working with the direct imaging of the luminescence decay (see Chapter 3). In this way, noise is reduced and statistical calculations can be performed.

The first set of irradiation to be described is the one performed using only the predeflector and protons of 3 MeV. As it was already mentioned in a previous chapter, the predeflector is the first deflecting element of the DEFEL beamline. When in operation, this device allows the beam to be delivered downstream during a short period of time. Setting the irradiation time to 1 $\mu$s, the lapis lazuli stones were irradiated with three different beam current intensities: 4, 20 and 60 nA. For each beam current, six areas per sample were visually chosen attempting to irradiate different colored zones and trying to check possible differences in the time patterns of light emission for the different irradiated areas. These irradiations were performed both with and without wavelength discrimination. For the former, two filters were used separately: one with a bandwidth of about 100 nm (FWHM) centered at 450 nm, and a high-pass with a cutoff at 495 nm.

Another mode of irradiation to be described, performed in more than one area per sample, was carried out using both predeflector and deflector and 3 MeV protons. This configuration was chosen in the attempt to deliver shorter pulses and analyze the fast components of the emission decays. Usually, as described in Chapter 2, the predeflector upper plate voltage is set to 800 V while the upper plate voltage of the deflector is set to 200 V. This configuration was changed for the measurements on the lapis lazuli stones since under those conditions no emission was detected, meaning the delivered dose was

not sufficient to result in detectable luminescence by the instruments and method used. For this reason, the predeflector voltage was kept at 800 V, but the one of the deflector was set to 70 V. The choice of voltage was made considering the lowest voltage that would completely deflect the beam. As it was described in Chapter 2.3 (eq. 2.13), the bunch duration is:

$$T = \sqrt{\frac{mE}{2}} \frac{4d(s+h)}{eV_d(l+2L)} \tag{4.1}$$

where $d$ is the distance between the deflector plates (5 mm), $l$ is the distance between two plates (0.6 mm) and $L$ is the distance between the deflector exit and the final slits (10 m). Considering a beam of protons of 3 MeV, $V_d$=70 V, the beam diameter $h$ of 3 mm and the final slits aperture $s$ of 2 mm, the bunch duration comes out to be approximately 17 ns.

The measurements with short pulses using both deflectors were performed without wavelength discrimination. The reason for that is that when attempting to use optical filters the luminescence signal had insufficient intensity to be used for our analysis. This can be understood considering that optical filters decrease significantly the intensity of light reaching the photocathode, both because their transmission efficiency is only around 50% and because wavelength selection itself already decreases the overall intensity by definition. The luminescence intensity in our case was not high enough to overcome these limitations.

Finally, irradiations were performed with 10 MeV carbon ions and a beam current around 50 nA. Irradiations with carbon ions, which had never been attempted previously on the DEFEL line, were carried out using only the predeflector, set to an irradiation time of approximately 1 $\mu$s. The reason for using heavier ions is their short range in the materials. Indeed, it is known that lapis lazuli is not completely transparent to its own light emission. Being composed of several minerals, each one with its own grade of transparency, photons coming from deeper layers can suffer absorption. Carbon ions were used in the attempt to produce higher ionization in the near surface volume than obtained with protons. Moreover, the behavior of the luminescence signal acquired with protons and heavier ions could be compared. Wavelength discrimination was done by placing a 500 nm high-pass optical filter in front of the PMT window.

The setup for the steady-state measurements was already described in the previous section. The acquisition of the spectra was performed by the use of the software SpectraSuite that communicates directly to the spectrometer through USB connection. The acquisition time per spectrum was of 100 ms, and for each spectrum the dark signal was subtracted. The spectral responsivity of the entire system, which consisted of optical fiber-flange-optical fiber-spectrometer, was evaluated with an Ocean Optics LS1-CAL Tungsten Halogen light source of known emittance spectrum. By measuring the lamp spectrum with our system, and having the real spectrum of the lamp, we calculated the calibration spectrum, which was used to normalize all the collected spectra from lapis lazuli.

Concerning data recording, since we were dealing with relatively large files, all data was firstly memorized as binary files (that can be of hundreds of MB to some GB), that are faster to be written and smaller, so that acquisition was not slowed down. To be read and analyzed, the transformation of the binary data into decimal and its analysis was performed using the software framework Root [80] and programs that I wrote in C++ on purpose for this work. In the next paragraph the description of how data were processed and analyzed will be given.

## 4.4 DATA ANALYSIS

As a "set of irradiation" we mean the set of digitized waveforms per area irradiated, given a particular irradiation configuration (beam current, deflector features, ion species). The quantity of waveforms acquired per set of irradiation was not fixed during the time this work was carried out. Starting from 200 waveforms, the number increased until 5000 when the signal showed low intensity. For every set, all the digitized waveforms were averaged and the standard error of the mean of each digitized sample was calculated [1]. The baseline was calculated with the first 400 signal samples before the trigger and subtracted from the overall signal.

As it was explained above, irradiations were performed in several different ways. The analysis of the results was performed taking into account only the signal behavior after the excitation was switched off, i.e., when the beam was deflected and blocked. This was accomplished by knowing the irradiation time, and by visualizing the luminescence behavior. For a better understanding, Figure 4.7 shows the example of a luminescence signal (baseline already subtracted) acquired in this work (in black) and the trigger signal (in red). In this example, the luminescence signal was obtained irradiating only with the predeflector during approximately 1 $\mu$s. The trigger signal represents the predeflector upper plate transition from off to on mode (negative impulse) and from on to off (positive impulse). Both the luminescence and the trigger signal were normalized to the maximum intensity for better visualization. As it can be seen in Figure, when the bunch of ions arrive at the target (first predeflector transition) the luminescence begins to increase until the second transition of the predeflector. At this point, with the beam deflected, the luminescence decreases. Figure shows the blowup of the luminescence signal: the coincidence between the second transition and the start of luminescence decrease is indicated by the green cursor.

[1] Again, the word sample in this case is not to be confused with the target sample. Instead, it means the digitized signal after a certain time from the trigger.

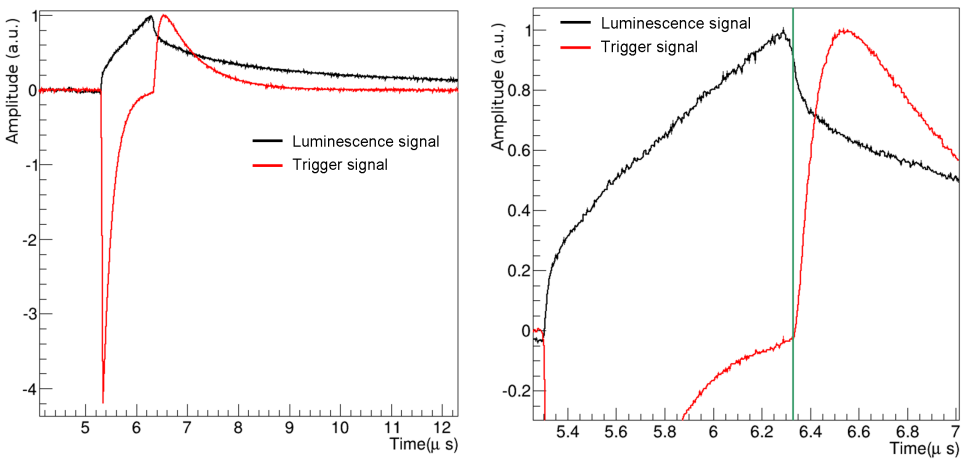


**Figure (4.7).** An example of a luminescence signal (black) plotted together with the trigger signal (red), where the decrease of the emission can be seen to coincide with the second transition of the trigger signal when the excitation is switched off.

# CHAPTER 5

# RESULTS

In this chapter the results obtained during the development of this work will be presented, including irradiation tests with known scintillators (BC-408 and $CdWO_4$) and measurements with lapis lazuli. As far as we know, this was the first time that a TRIBIL study was performed on lapis lazuli. In the attempt to increase the possibility of finding markers that could discriminate lapis lazuli from different origins, several irradiation setups were exploited by changing the beam current, ion species and the luminescence wavelength detected. Concerning lapis lazuli results, most of the decay curves could be described by a sum of exponential decays, and indications of possible provenance markers were found. However, not all the decay curves could be described by simple expressions, and some features observed in the results both from the known scintillators and lapis lazuli still need to be investigated more in depth with further experiments.

## 5.1 STANDARD SCINTILLATORS RESULTS

Even though DEFEL operation and features are well known, irradiation of standard scintillators (BC-408 and $CdWO_4$) were performed in order to better comprehend the relationship between beam characteristics, the luminescence emission and the digitized signal. The results of these measurements will be presented in this paragraph because they "inspired" the measurements performed with lapis lazuli. By using a fast scintillator as BC-408 that has a main decay component of 2.1 ns, it was possible to confirm the characteristics calculated for the excitation pulse when using both deflector and predeflector. With a 3 MeV proton beam of 3 mm diameter, 2 mm of final slits aperture, and the deflector voltage set to 200 V the pulse duration time can be estimated from the simplified expressions presented in Chapter 2, coming out to be ≈4 ns. As it can be seen in Figure 5.1, the actually observed rise time for the pulse (shown in black), taking the time for the signal to increase from 10 to 90% of its maximum, is ≈12 ns. Considering the finite time of the voltage transision, the uncertainty for the digitized signal given by the sampling time interval (which is 4 ns), the PMT time response, and the short decay time of the scintillator that influences the luminescence shape even during excitation, the observed value appears to be reasonable. For comparison, the signal acquired setting the deflector to 70 V, which corresponds to a longer duration of the excitation pulse, is shown in in red in the same Figure. Since in this case, the rise time is also around 12 ns, we

can conclude that the overall response of our system is mainly determined by limitations of the photomultiplier and the digitizer. So, it is possible to see that changing from 200 V to 70 V the upper plate voltage of the deflector, the shape of the digitized temporal response does not change, except for a gain in the luminescence intensity that increases more than three times. For this reason, in order to increase the luminescence intensity in the measurements performed with lapis lazuli, the deflector voltage was set to 70V.

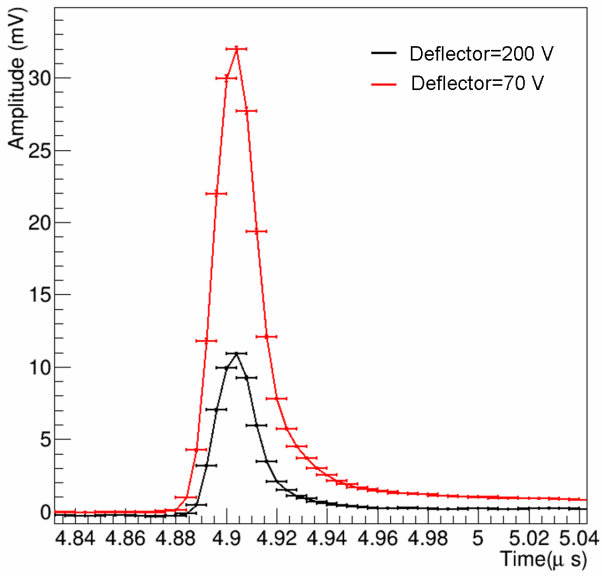


**Figure (5.1).** BC-408 luminescence signal obtained by irradiation with the deflector upper plate set to 200 V (black) and 70 V (red). The lines are only shown as a guide for the eyes.

In order to test the setup, measurements were also performed with $CdWO_4$, which is a scintillator with longer decay times compared to BC-408. The short irradiation consisted in bombarding $CdWO_4$ with 3 MeV protons, a beam current of 2.6 nA[1] and setting the deflector upper plate to 70 V (irradiation time about 10 ns). The decay after the excitation pulse was well fitted with two exponentials, as it can be seen in Figure 5.2 on the left, shown in log scale. The two decay times found were approximately $\tau_1 = 5\mu s$ and $\tau_2 = 14\mu s$, which are in agreement with the lifetimes found in the literature [79]. The faster lifetimes that are sometimes reported in the literature were not observed. $CdWO_4$ results are particularly important because it is a standard scintillator with lifetimes that are of the order of those expected for the lapis lazuli stones studied in this work, since minerals have decay times of the order of microseconds [36]. When irradiating $CdWO_4$ with 30 pA during 800 ns (using only the predeflector) (Figure 5.2 on the right, in log scale) the exponential fit reveals approximately the same lifetimes as obtained with short irradiation.

[1]A higher current was required because of the lower efficiency of $CdWO_4$ compared to BC-408.

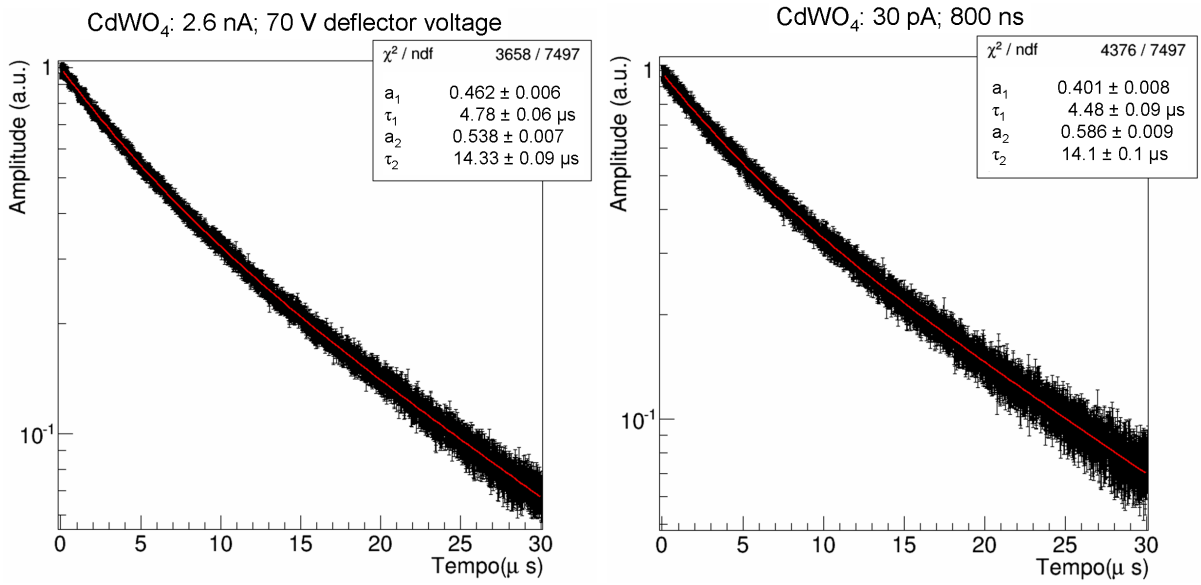


**Figure (5.2).** Exponential fit of the luminescence decay of $CdWO_4$. On the left the irradiation was performed with a beam current of 2.6 nA and setting the deflector upper plate to 70 V (short excitation time). On the right, a much lower beam current of 30 pA was used and the excitation time was increased to about 800 ns (using only the predeflector). Plots are shown in log scale.

## 5.2 LAPIS LAZULI RESULTS - DEFLECTOR

In this section, the results obtained by irradiating lapis lazuli with short ion pulses using both predeflector and deflector will be presented. For these measurements, no wavelength discrimination was performed, the deflector upper plate voltage was set to 70 V, protons of 3 MeV were used and the beam current at the final Faraday Cup of DEFEL was 100 nA. Up to three areas per stone were irradiated. Figure 5.3 shows as an example three normalized decays curves from an Afghan sample (AFG2) where it is possible to see the luminescence intensity after the arrival of the bunch on the target, increasing until reaching a maximum, and subsequently decaying after the excitation was switched off. The circle in red represents the time arbitrarily chosen as the beginning of the luminescence decay, to which all waveforms intensities were normalized. The curves that will be shown later in this section contain only the information after this time.

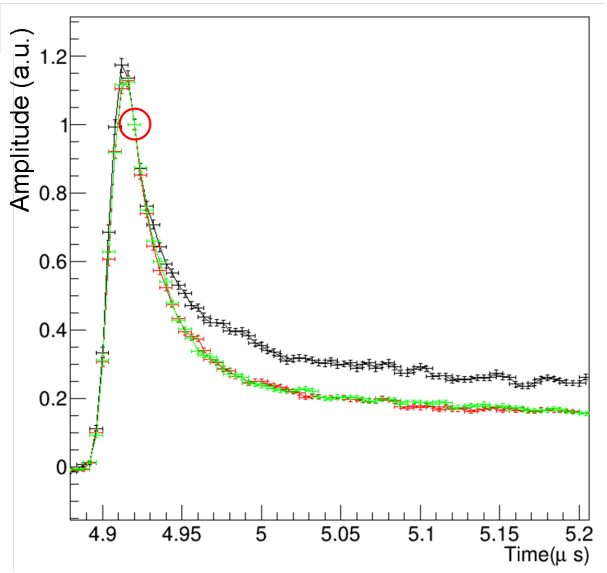


**Figure (5.3).** Luminescence rise and decay from AFG2. Different colors represent different irradiated zones of the sample. The curves are normalized to an arbitrary time (red circle) chosen as $t = 0$ after the excitation was already switched off.

The normalized luminescence decays of lapis lazuli samples from Afghanistan, Chile, Myanmar, Tajikistan and Siberia can be seen in Figures 5.4, 5.5, 5.6, 5.7 and 5.8. In each graphic, different areas of the same sample are numbered and shown in different colors. One of the first aspects of the decay curves one notices is that in some samples the signals present more homogeneous results than in others. This is expected since lapis lazuli is a very heterogeneous material, and its luminescence decay is the result of the excitation of different minerals in different concentrations. For this reason, we were firstly interested in finding a different lifetime component in the temporal behavior of lapis lazuli luminescence. Therefore, only the lifetimes must be considered, because the weight of each lifetime component is influenced by the concentration of the emission center. It is true that the contribution of each decay component might also be used as a possible marker to distinguish different origins; however, due to the limited number of irradiated areas taken in this irradiation setup, we considered that a study with this approach would lack meaning in this set of results. Instead, this parameter will be used in this Chapter when presenting other results.

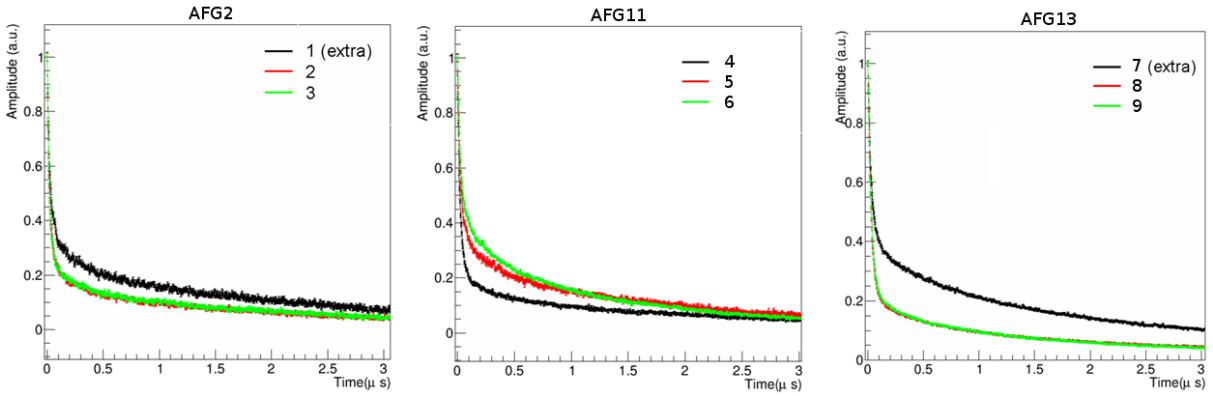


**Figure (5.4).** Normalized luminescence decay curves from Afghan samples (AFG2 on the left, AFG11 on the middle and AFG13 on the right) obtained by irradiating the samples with 3 MeV protons, 100 nA beam current and setting the deflector upper plate voltage to 70 V.

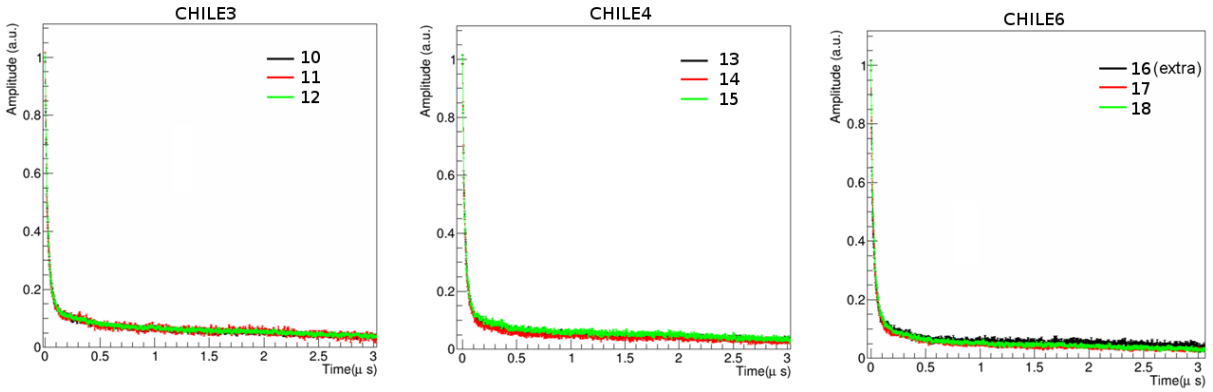


**Figure (5.5).** Normalized luminescence decay curves from Chilean samples (CHILE3 on the left, CHILE4 on the middle and CHILE6 on the right) obtained by irradiating the samples with 3 MeV protons, 100 nA beam current and setting the deflector upper plate voltage to 70 V.

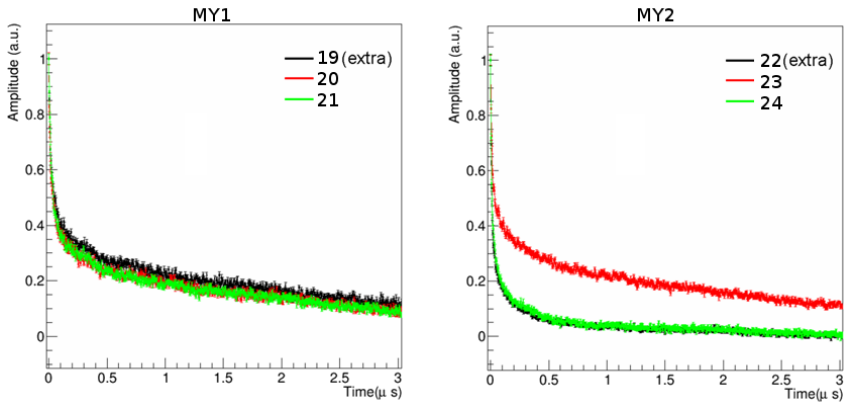


**Figure (5.6).** Normalized luminescence decay curves from Myanma samples (MY1 on the left and MY2 on the right) obtained by irradiating the samples with 3 MeV protons, 100 nA beam current and setting the deflector upper plate voltage to 70 V.

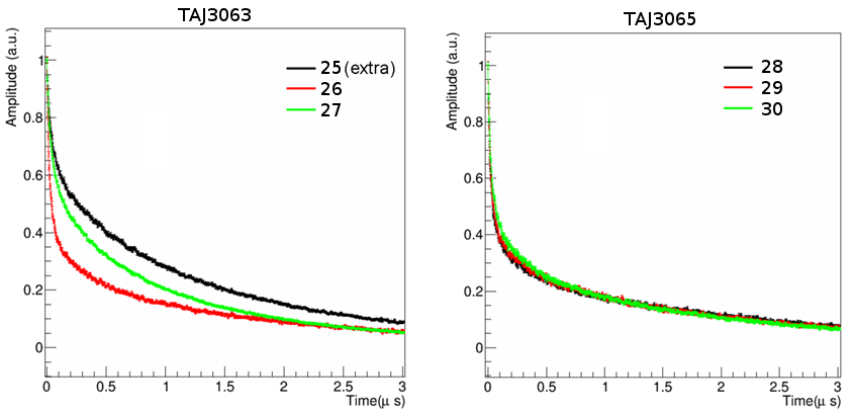


**Figure (5.7).** Normalized luminescence decay curves from Tajikistani samples (TAJ3063 on the left and TAJ3065 on the right) obtained by irradiating the samples with 3 MeV protons, 100 nA beam current and setting the deflector upper plate voltage to 70 V.

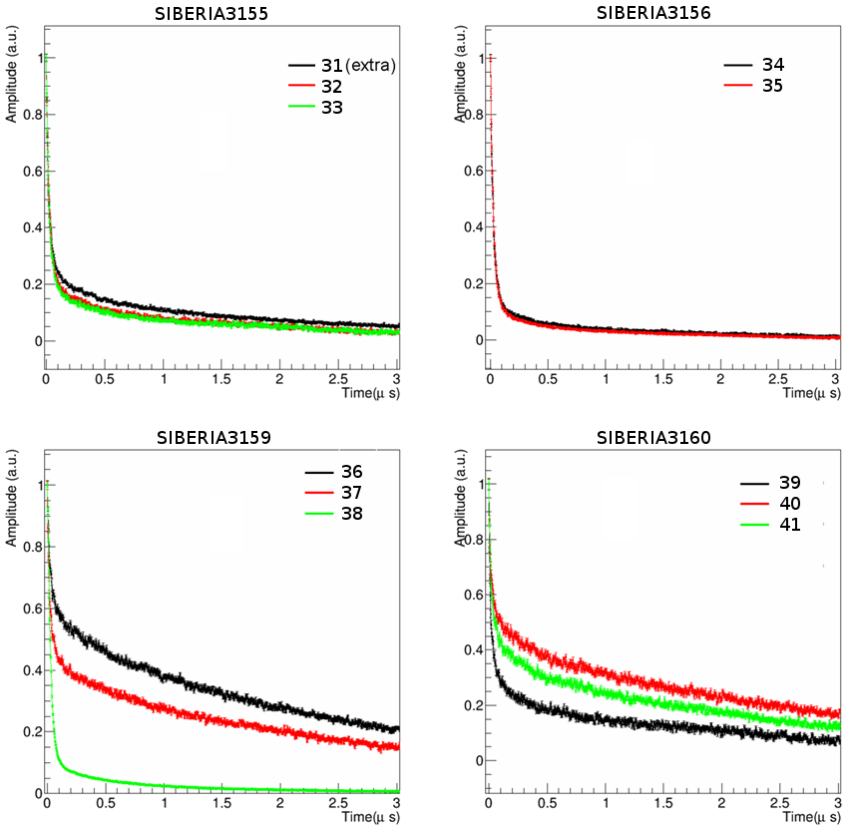


**Figure (5.8).** Normalized luminescence decay curves from Siberian samples (Siberia3155 on the top left, Siberia3156 on the top right, SIBERIA3159 on the bottom left and SIBERIA3160 on the bottom right) obtained by irradiating the samples with 3 MeV protons, 100 nA beam current and setting the deflector upper plate voltage to 70 V.

Attempting to see whether the luminescence decay curves obtained in this set of irradiation had a relationship with the luminescence wavelength spectrum, for all areas irradiated, except the ones indicated by "extra" in Figures 5.4-5.8, the luminescence spectrum was also obtained. Since in order to obtain the luminescence spectra the samples must be irradiated in a countinuous mode for a period of time that is longer than the ones used for time-resolved measurements, we were concerned about the effects of this longer

irradiation to the luminescence decay. For this reason, the luminescence decay of sample Siberia3159 (chosen arbitrarily among the other samples) was acquired before and after an exposure of 1 minute to the beam in continuous mode. The beam current was 90 nA and the luminescence decay was obtained setting the deflector upper plate voltage to 70 V. Figure 5.9 shows the results of the test for the luminescence before (black) and after (red) the long irradiation. On the left it is possible to see a decrease of the maximum luminescence intensity of approximately 35%, which might be the result of the destruction of luminescence centers due to long exposure to the beam. However, as can be seen on the right of Figure 5.9, when normalized to when the excitation was switched off the curves overlap, meaning that no significant changes on the shape of the luminescence decay were observed as a consequence of the long exposure to the beam.

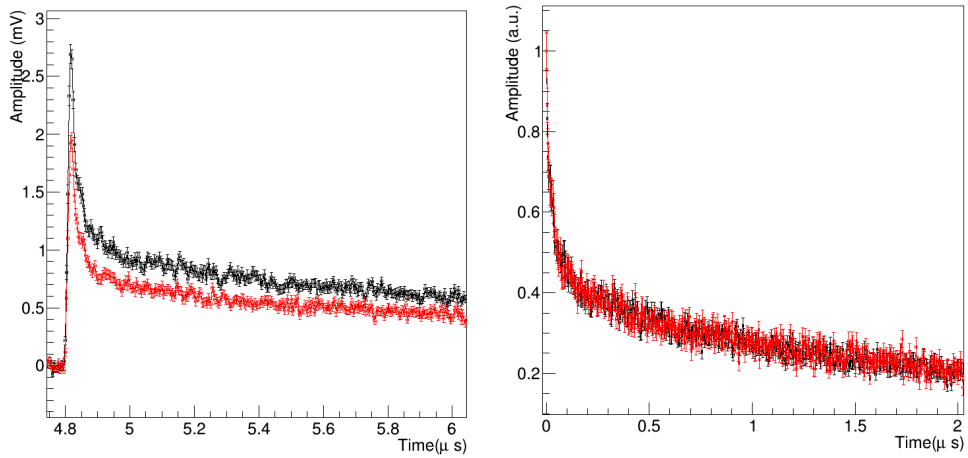


**Figure (5.9).** Luminescence emission from SIBERIA3159 before (black) and after (red) an exposure of 1 minute to a 3 MeV protons beam with beam current of 90 nA. The decays were obtained setting the deflector upper plate to 70 V. On the right only the normalized decays after the excitation was switched off are shown.

Figure 5.10 (AFG), 5.11 (CHILE), 5.12 (MY), 5.13 (TAJ) and 5.14 (SIBERIA) show the luminescence spectrum of each of the areas irradiated. For each sample, the curves of the same color as the ones from Figures 5.4-5.8 represent the same irradiated area[2]. The emission spectra here presented will be considered only in a qualitative manner, attempting to find clear correlations between the spectra and the decay curves.

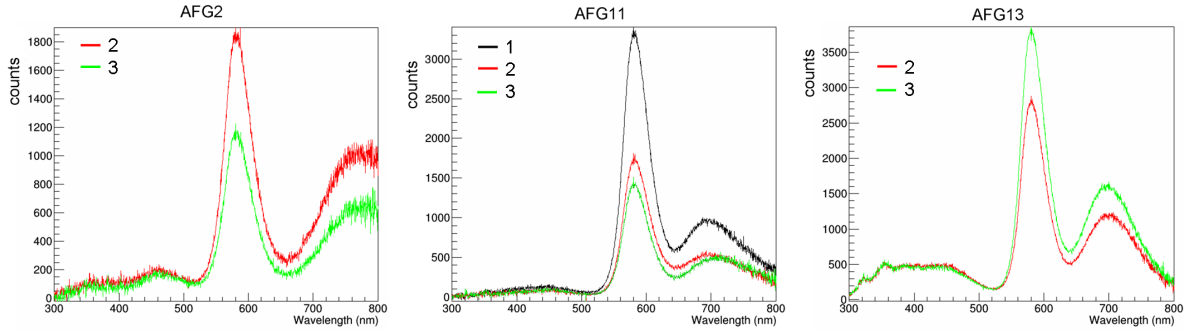


**Figure (5.10).** Emission spectra taken from samples from Afghanistan (AFG2 on the left, AFG11 on the middle, and AFG13 on the right).

[2]Actually, for not all irradiated areas a corresponding spectrum was taken.

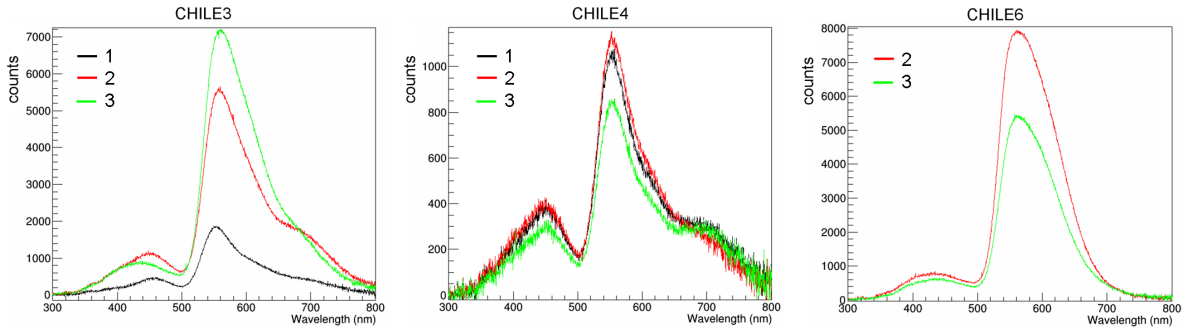


**Figure (5.11).** Emission spectra taken from samples from Chile (CHILE3 on the left, CHILE4 on the middle, and CHILE6 on the right).

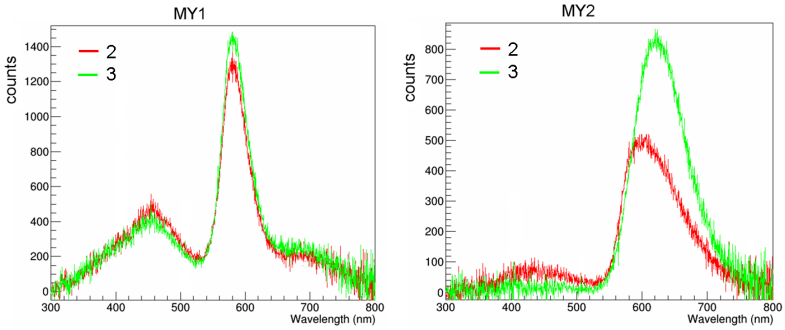


**Figure (5.12).** Emission spectra taken from samples from Myanmar (MY1 on the left and MY2 on the right).

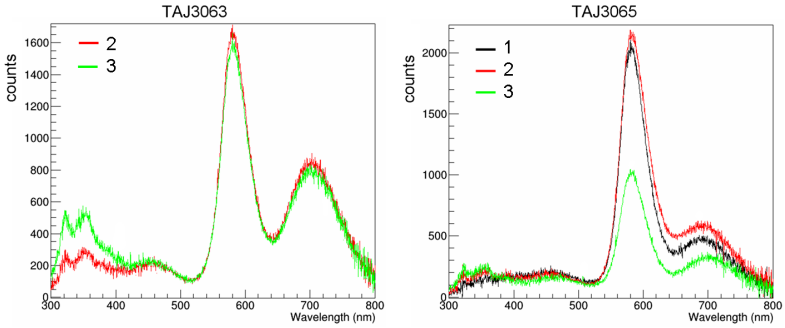


**Figure (5.13).** Emission spectra taken from samples from Tajikistan (TAJ3063 on the left and TAJ3065 on the right).

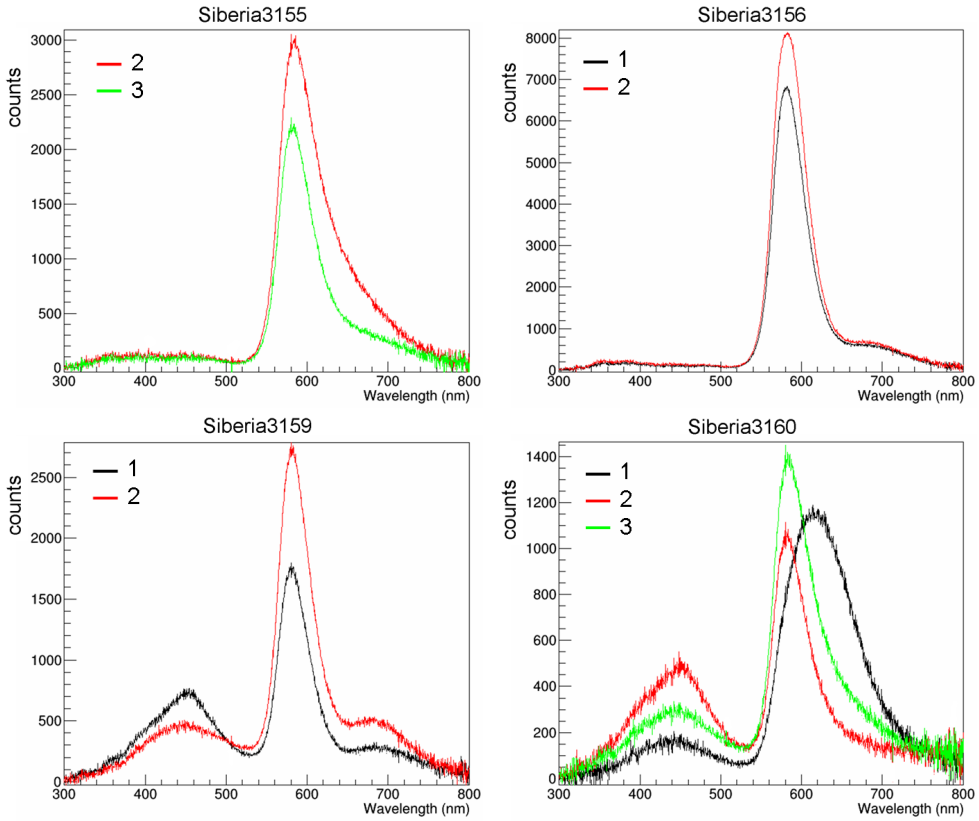


**Figure (5.14).** Emission spectra taken from samples from Myanmar (SIBERIA3155 on the top left, SIBERIA3156 on the top right, SIBERIA3159 on the bottom left, and SIBERIA3160 ont he bottom right).

In order to try and draw some conclusion about correlations between the spectra (just shown) and the luminescence decay curves reported in Figures 5.4-5.8, it is important to keep in mind that, since in the latter no wavelength discrimination was performed, several features in the luminescence decays are influenced by, for example, the different sensitivity of the PMT detector to photons of different wavelengths. For example, when looking at the emission spectrum of CHILE3 at Figure 5.11, qualitatively it is possible to see that the irradiated areas show different contributions in wavelength to the emission, even though its decay curves in Figure 5.5 seem to overlap. Instead, considering the TAJ3063 sample, the luminescence spectrum in green shows that the corresponding irradiated area exhibited a more intense emission in the 320-360 nm range, while all other emission bands remained the same. In this case, the luminescence decays showed that the green curve in fact presents a larger contribution of a component that might indeed be associated to the more intense emission seen in the spectra.

In order to know whether a more quantitative relationship can be found between the luminescence temporal behavior and the luminescence spectra, and to find differences between samples of different origins, the decays were fitted with multi-exponential functions. For example, Figure 5.15 shows the decay curve from AFG11. On the left the decay is shown in log scale, where four components might be visually suggested. In this case a fit with four exponentials provide results in reasonable agreement to the experimental data. In Figure 5.15 on the right a blow-up of the first 200 ns is shown. The fourth component contributes very little to the overall luminescence emission. Because of the

scarce statistics of these long lifetime components, in the following, when comparing the results, the lifetimes components are considered in the analysis only if they contributed to at least 5% of the overall emission.

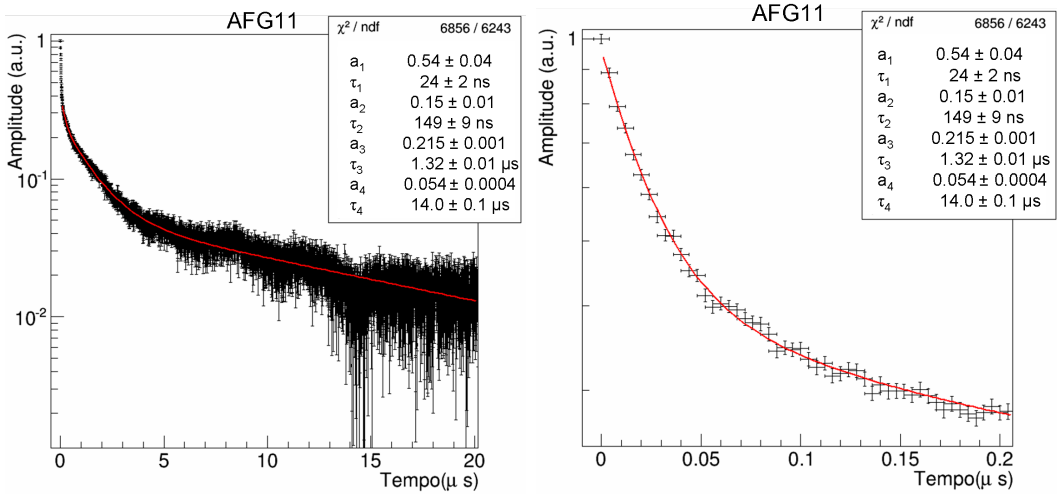


**Figure (5.15).** Example of a luminescence decay taken from AFG11 in log scale. On the left, the whole four-exponential fit performed is shown. On the right the blow-up of the first 20 ns is shown. The curve was obtained by irradiation with 3 MeV protons, beam current of 100 nA and setting the deflector upper plate to 70 V.

Multi-exponential fits were performed to all the curves in Figure 5.4-5.8 and the lifetimes found were separated in four groups: tens of nanoseconds (group 1); hundreds of nanoseconds (group 2); few microseconds (group 3) and tens of microseconds (group 4). Figure 5.16 shows the results for the four groups: Group 1 at top left, Group 2 at top right, Group 3 at bottom left and group 4 at bottom right. As already mentioned, Group 4 does not contain all the luminescence decays because only the components that contributed to at least 5 % of the total decay were considered. As can be seen in Figure 5.16, the lifetime results do not form clusters of values in the graph. If this were the case, finding possible markers using TRIBIL would be more straightforward than what we actually obtain with the measurements. As it was presented in Chapter 3, the only fact that a luminescence decay can be fitted with a four-exponential equation is not sufficient to affirm that four luminescence centers are involved in the emission process. We can not know for sure that the lifetime spread found in our results is in fact due to different luminescence centers or simply a statistical dispersion of the results. It is clear, from the results, that working with a heterogeneous material such as lapis lazuli and trying to find differences between stones from different origins, but still very similar, involves also searching for subtle indications. For this reason, for the results presented in Figure 5.16, the average of all decay times within a group was calculated and represented by the black horizontal line. The maximum and minimum limits considering the standard deviation of the results are shown by the dashed red lines. In the first group, the lifetimes that stay considerably out of the average range are the ones from TAJ3063, curve 25 and 27, and one from MY2, curve 24. For the second group, the ones most distinguishable from the others are MY2, curve 23, Siberia3156, curves 34 and 35, TAJ3063, curve 27, and Siberia3159, curves 34,

35 and 38. The third group is particular because in this case a new component was found in some of the curves. While most curves were fitted with four exponentials, some of them could only be well fitted if a fifth component was added. The curves that presented a fifth component were from AFG13, curves 7, 8 and 9, TAJ3063, curves 25 and 27, and Siberia3159, curve 36. Even though group 4 contains less information than the others, for completeness it will be considered. In this group, the times that ended up out of the average region are found for AFG2, curve 1, and Siberia3160, curve 40.

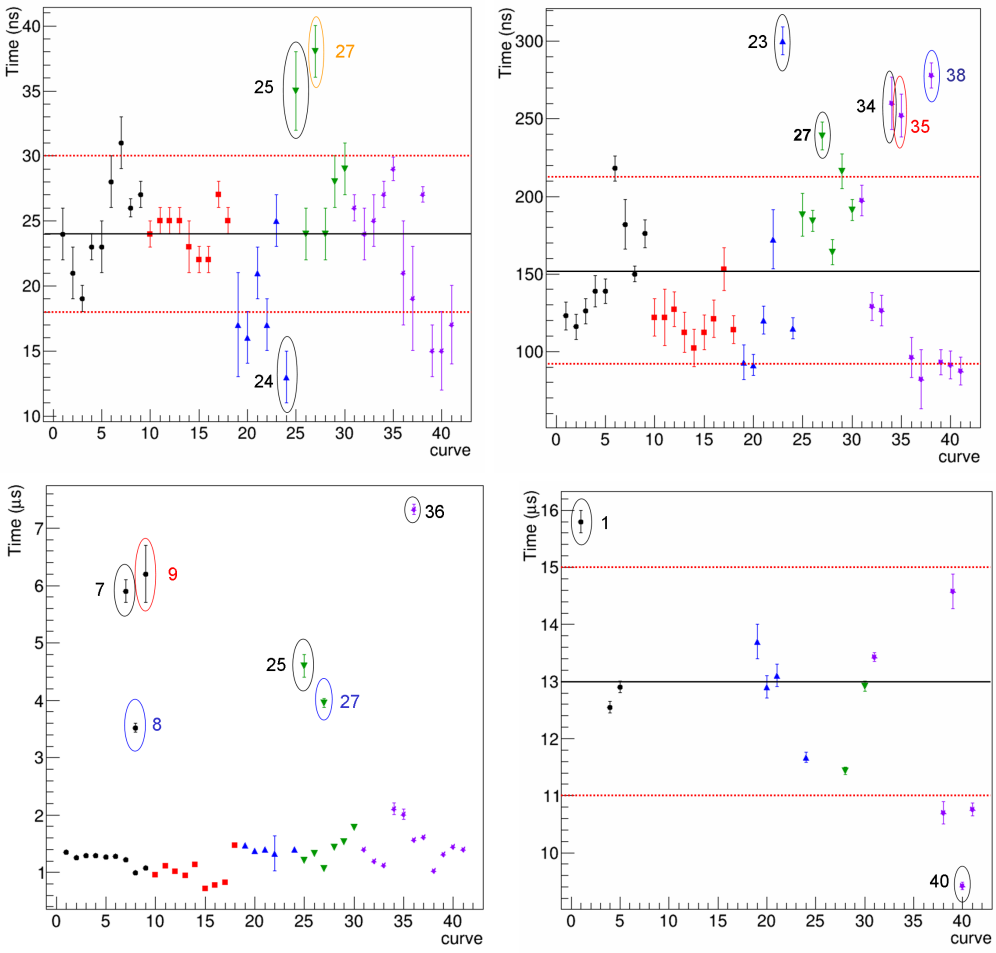


**Figure (5.16).** Lifetimes obtained by fitting the decay curves of Figures 5.4-5.8 with a sum of four exponentials. The results are separated in four groups. Group 1 (top left) contains the lifetimes whose values are of the order of tens of nanoseconds, group 2 (top right) contains those of the order of hundreds of nanoseconds, group 3 (bottom left) contains those of few microseconds and group 4 (bottom right) contains those whose values are of the order of tens of microseconds.

The amount of information collected, as can be seen, is very large. However, unfortunately, as a whole only some weak indication might be obtained from the classification of the lifetime components. No conclusive arguments can be established to discriminate the provenance, although some hints may be given: for example, some irradiated areas in the Tajikistan origin samples showed considerably higher short lifetimes component (first group), and additional components in the third group; and Chilean samples lifetimes remained always within the limits of the average range calculated for each group, with very little dispersion in the measured values. It is also confirmed that the three analyzed areas in AFG13, which from the point of view of the luminescence spectra had shown

an “anomalous” behavior, have decay lifetime values distinctly different from the other Afghan samples.

Concerning the latter issue (relationship between decay lifetimes and emission spectra), a more detailed study must be performed. In general we have seen that the variables to work with were too many in our set of measurements, and simplifications should be made, as for example, attempting to perform wavelength discrimination in the TRIBIL measurements.

## 5.3 LAPIS LAZULI RESULTS - PREDEFLECTOR

Next, the results obtained with the longer exposures (≈1 $\mu$s) using only the predeflector will be presented. Irradiating the samples with 3 MeV protons, measurements were performed with and without wavelength discrimination; the former were carried out by the use of two optical filters separately: 450±50 nm and a high pass at 495 nm. Three beam currents were used: 4, 20 and 60 nA. This paragraph will be separated considering the filter and the beam current. However, the irradiated zones in lapis lazuli were always the same (see Figures 5.17-5.21). The zones were selected by looking at the sample through a micro-camera and the criterion for the selection depended on the sample. For example, Figure 5.17 (left) shows the AFG2 sample with the selected areas to be irradiated. This sample visually appears with relatively homogeneous areas (at variance with other samples where blue and white regions are present); however, it contains a lot of pyrite traces visible as dark spots. Since pyrite is known to present no luminescence emission, the irradiation areas were chosen attempting to optimize the luminescence signal by selecting less pyrite as possible. Samples such as the Chilean ones (Figure 5.18), on the other hand, visibly contain distinguishable white and blue areas, so the selection of the irradiation regions was performed attempting to hit only blue or only white areas.

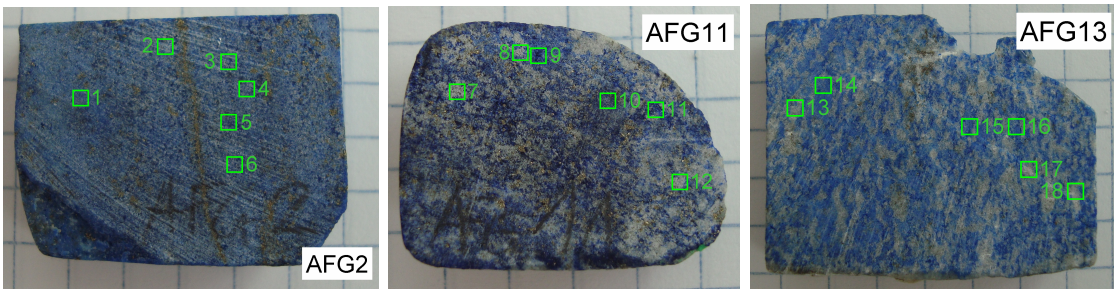


**Figure (5.17).** Indication of the measurement points taken from the samples from Afghanistan: AFG2 (left), AFG11 (middle) and AFG13 (right).

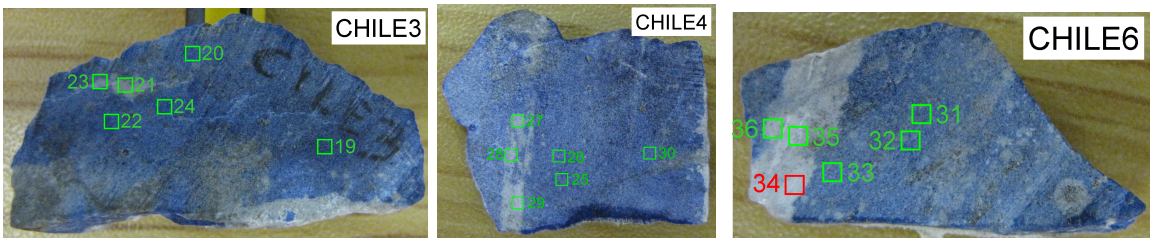


**Figure (5.18).** Indication of the measurement points taken from the samples from Chile: CHILE3 (left), CHILE4 (middle) and CHILE6 (right).

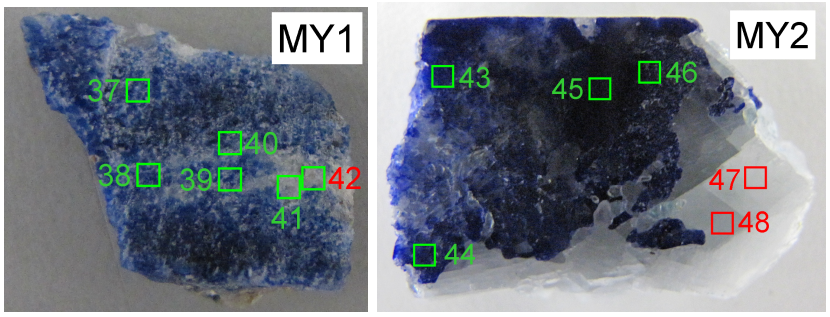


**Figure (5.19).** Indication of the measurement points taken from the samples from Myanmar: MY1 (left) and MY2 (right).

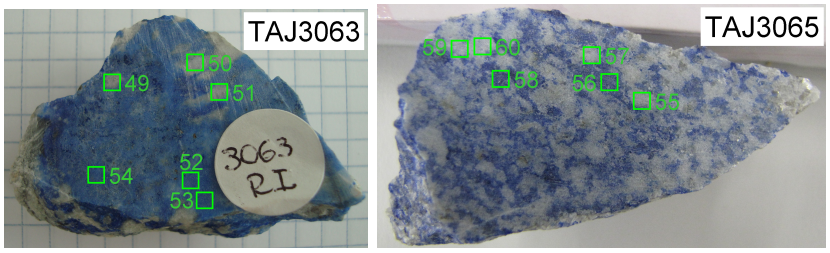


**Figure (5.20).** Indication of the measurement points taken from the samples from Tajikistan: TAJ3063 (left) and TAJ3065 (right).

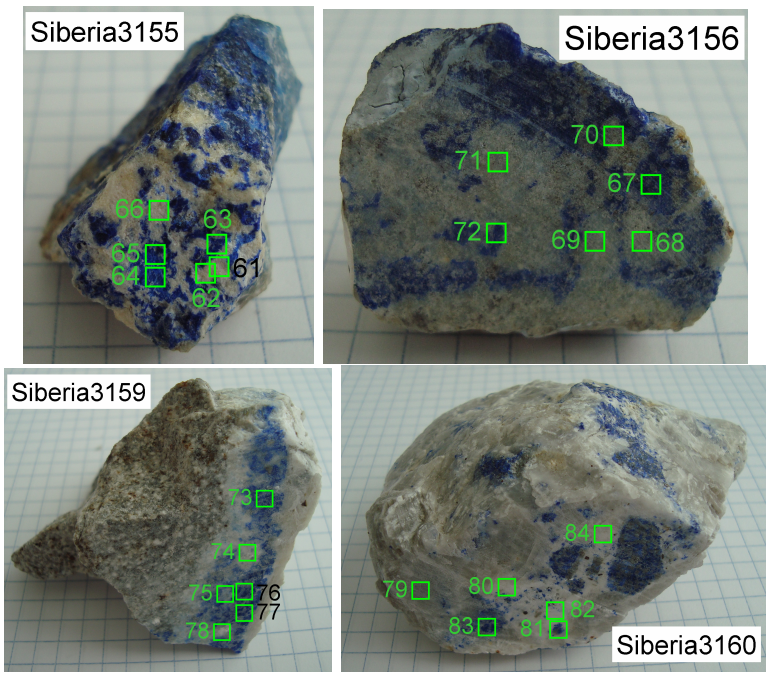


**Figure (5.21).** Indication of the measurement points taken from the samples from Siberia: SIBERIA3155 (top left), SIBERIA3156 (top right), SIBERIA3159 (bottom left) and SIBERIA3160 (bottom right).

We were interested in knowing whether the overall luminescence decay from lapis lazuli had any relationship to the irradiated area on the sample (blue or white zone). The reason for this question was that, if this was indeed the case, it would simplify the study by decreasing the number of variables involved in the measurements, so one could compare results from similar areas. In order for us to know whether the emission was dependent on the irradiated area, the luminescence decay of all points were initially taken without wavelength discrimination. Examples of the results can be seen in Figure 5.22 where the normalized decays after the excitation was switched off are shown on top and the non-normalized rise and decay can be seen on the bottom for the AFG2, CHILE6 and TAJ3063 samples. From Figure 5.22 it is possible to see that the decays obtained from AFG2 and CHILE6 are relatively in good agreement, i.e., the curves overlap each other in each sample, seeming to have similar overall decay shapes. The result for the AFG2 sample is in conformity to the physical appearance of the stone, which seems to be more homogeneous concerning color. Instead, CHILE6 and TAJ3063 show some clear blue and white zones and even so the decays from CHILE6 seem to be similar independent on the color of the zone irradiated, whereas TAJ3063 show some differences that do not seem to have a relationship to the color of the irradiated zone. When looking at the maximum intensities, both curves from CHILE6 that showed higher luminescence intensity (curve 34 and 35) come from white areas in the sample, but another white area (curve 36) showed a luminescence maximum similar to the ones from blue areas. Similarly, from the curves that showed higher luminescence intensity from TAJ3063 (curves 49, 51 and 54), two of them come from white zones (49 and 51) and another white zone (curve 50) instead showed a luminescence intensity like the ones from blue zones. Thus, it is not possible to say that white and blue areas show differences in emission neither in the decay nor in the

luminescence intensity

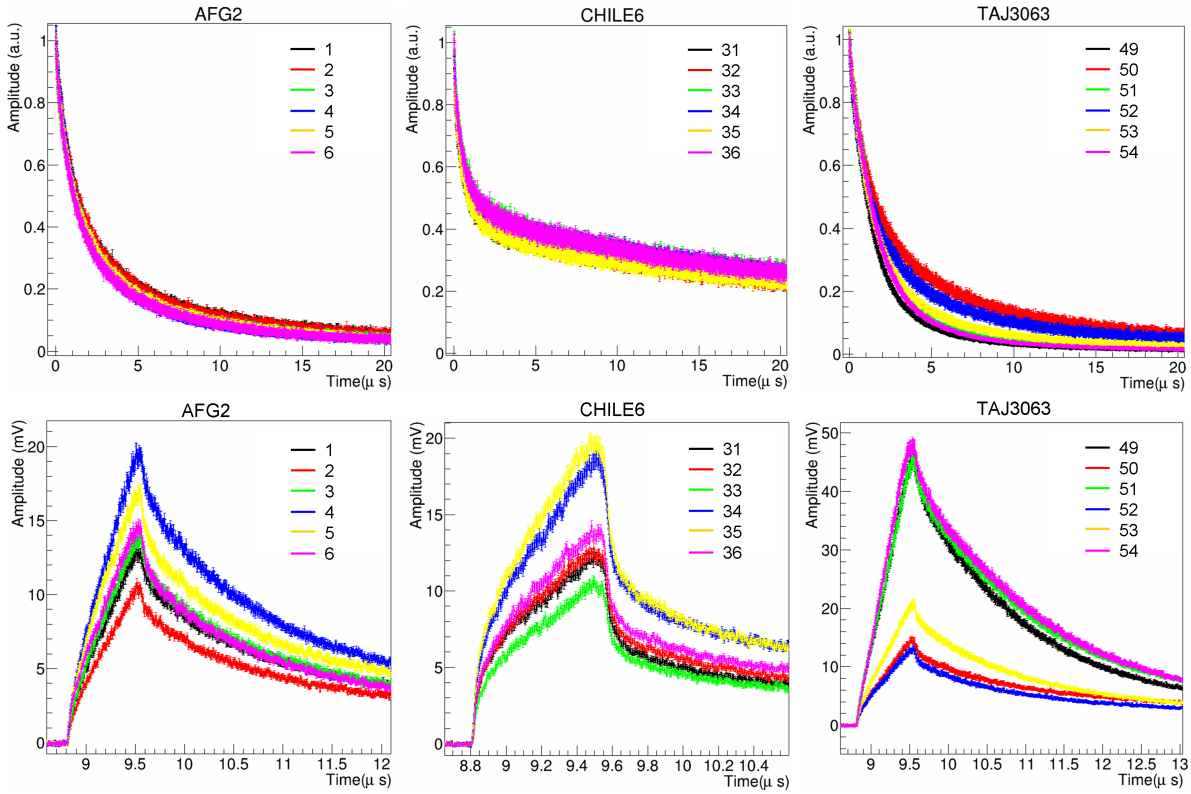


**Figure (5.22).** Normalized luminescence decays taken without wavelength discrimination, irradiation time of 1 $\mu$s and a beam current of 4 nA are shown on top: AFG2 on the left, CHILE6 in the center, and TAJ3063 on the right. The same curves are shown on the bottom without normalization and with a blow-up of the signal during excitation.

Next, the results obtained using the 450±50 nm optical filter and a beam current of 4 nA will be presented. For clarity, all normalized decay curves are shown in Figures 5.23-5.27 and numbered according to the areas to which they are related. Some curves might seem to have higher uncertainty on the results but this is barely a consequence of the normalization, since some signals are more intense than others.

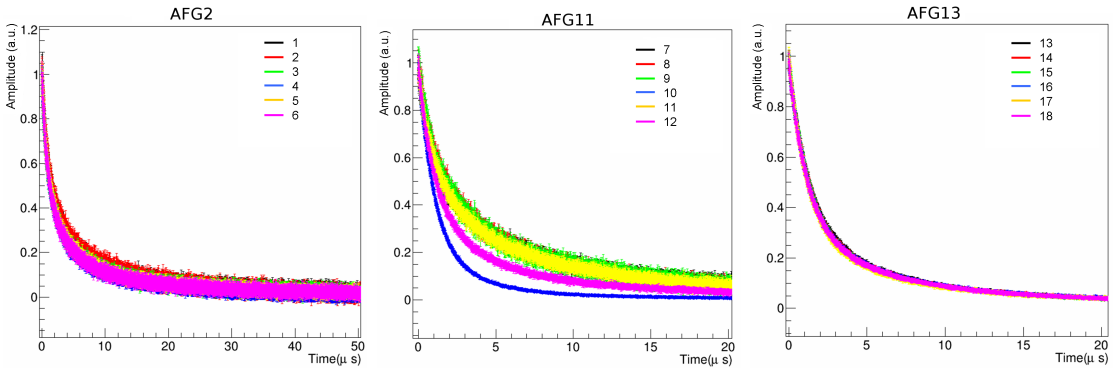


**Figure (5.23).** Normalized luminescence decay curves from AFG2 (left), AFG11 (middle) and AFG13 (right) obtained by irradiating the samples with 3 MeV protons, a beam current of 4 nA and an irradiation time of approximately 1 $\mu$s. Wavelength discrimination was performed with a 450±50 nm optical filter.

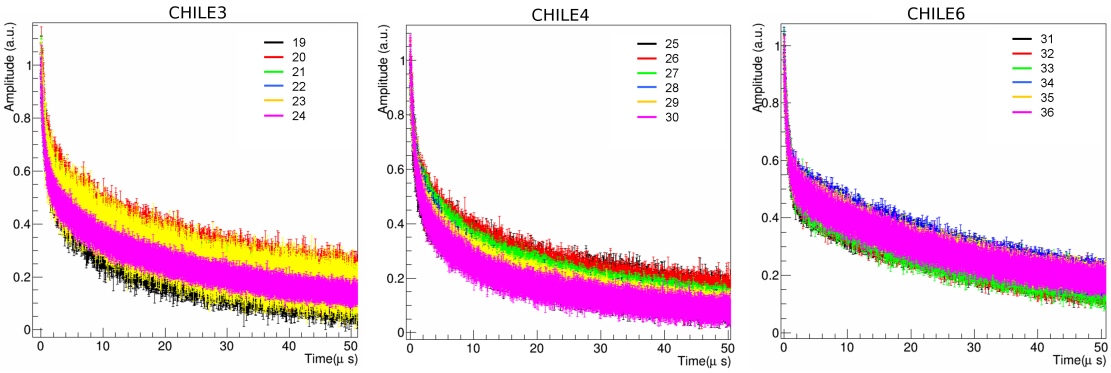


**Figure (5.24).** Luminescence decay curves from CHILE3 (left), CHILE4 (middle) and CHILE6 (right) obtained by irradiating the samples with 3 MeV protons, a beam current of 4 nA and an irradiation time of approximately 1 $\mu$s. Wavelength discrimination was performed with a 450±50 nm optical filter.

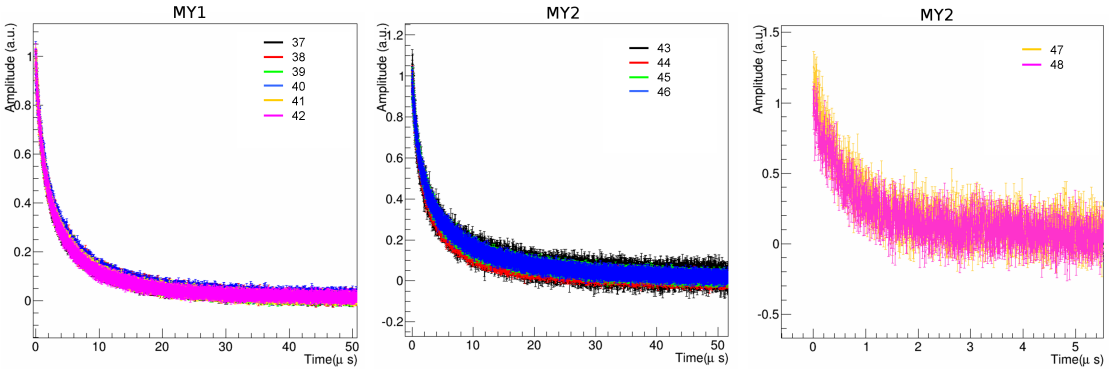


**Figure (5.25).** Luminescence decay curves from MY1 (left), MY2 (middle and right) obtained by irradiating the samples with 3 MeV protons, a beam current of 4 nA and an irradiation time of approximately 1 $\mu$s. Wavelength discrimination was performed with a 450±50 nm optical filter.

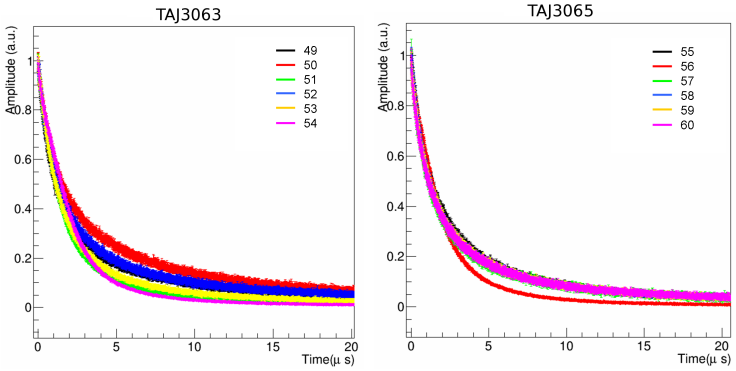


**Figure (5.26).** Luminescence decay curves from TAJ3063 (left) and TAJ3065 (right) obtained by irradiating the samples with 3 MeV protons, a beam current of 4 nA and an irradiation time of approximately 1 $\mu$s. Wavelength discrimination was performed with a 450±50 nm optical filter.

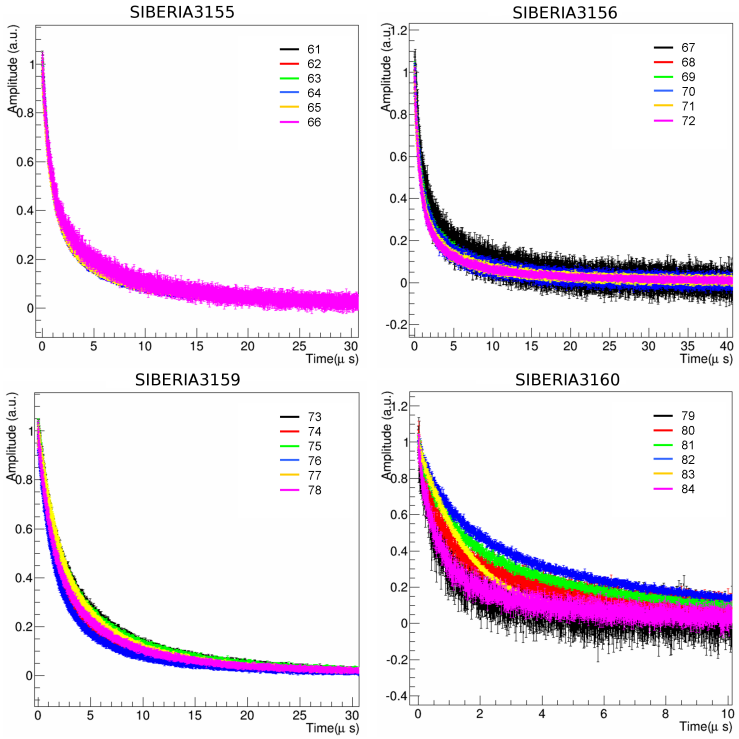


**Figure (5.27).** Luminescence decay curves from SIBERIA3155 (top left), SIBERIA3156 (top right), SIBERIA3159 (bottom left) and SIBERIA3160 (bottom right) obtained by irradiating the samples with 3 MeV protons, a beam current of 4 nA and an irradiation time of approximately 1 $\mu$s. Wavelength discrimination was performed with a 450±50 nm optical filter.

In order to know whether in this case the luminescence possesses a relationship with the irradiated zone, here again the non-normalized rise-decay emissions of AFG2, CHILE6 and TAJ3063 are shown in Figure 5.28. Also in this case, it seems that the results are independent on the color of the zone irradiated. Indeed, the differences in emission seen for the CHILE6 sample, where areas of different colors were irradiated, are no so relevant, while curves from blue zones from TAJ3063 (54, 52 and 53) show very different intensities. It is possible that, since the stones are so heterogeneous and choosing homogeneous areas can be confusing for the naked eye, a region that might seem blue can contain layers of other minerals above or below.

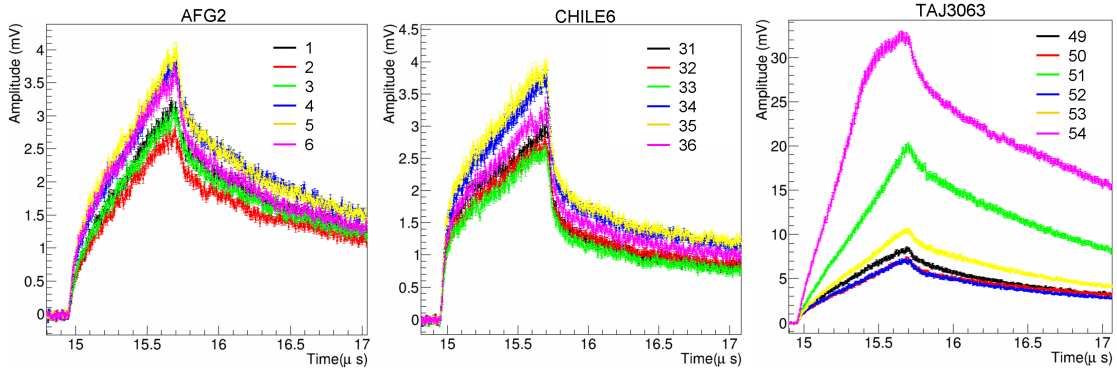


**Figure (5.28).** Luminescence emission (rise-decay) from AFG2 (left), CHILE6 (middle) and TAJ3063 (right). Irradiations were carried out with 3 MeV protons, 4 nA of beam current and excitation time of 1 $\mu$s. Wavelength discrimination was performed with a 450±50 nm optical filter.

Concerning the shape of the luminescence decays shown in Figures 5.23-5.27, most of

the curves can be fitted by a sum of exponential decays (up to 5 exponentials). Figure 5.29 shows an example given by AFG13, curve 16. As can be seen, in this case four exponential components are sufficient for a good fit. By performing the fitting procedures on most of the decays obtained in this set of irradiation, the lifetimes obtained were divided in three groups; group 1 contains the lifetimes that stayed on the range 0-1.5 $\mu$s, group 2 contains the range between 1.5-9 $\mu$s and group 3 contains the lifetimes longer than 10 $\mu$s. In the results shown in the following, in some cases more than one lifetime component can be within the same group, so that the overall number of points that will be reported below in Figure 5.31 (as well as later in Figures of similar analysis) can be larger than the total number of irradiated zones in the samples from each origin. In all cases, only the components that contributed to at least 5% of the total decay were considered.

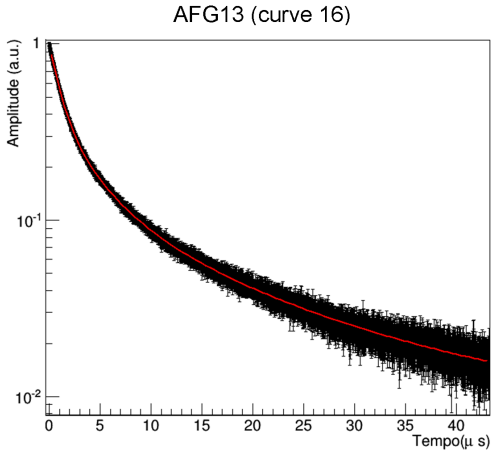


**Figure (5.29).** Normalized luminescence decay from AFG13 (curve 16) in log scale, well fitted with a sum of four exponentials.

Some curves obtained from TAJ3063 show a behavior that can not be described by a multi-exponential decay. Figure 5.30 shows the curves from TAJ3063 in log scale at the first 20 $\mu$s on the left, and the first 5 $\mu$s on the right. As can be seen clearly in the pink curve, the decay starts with a slower component that does not allow to reproduce the whole decay by a simple sum of exponential decays. We observe that this curve was just the one that also showed a different behavior during the excitation period (Figure 5.28 on the right). This effect will be discussed later in this paragraph. For the moment, we will concentrate on the other decays where this effect is not observed.

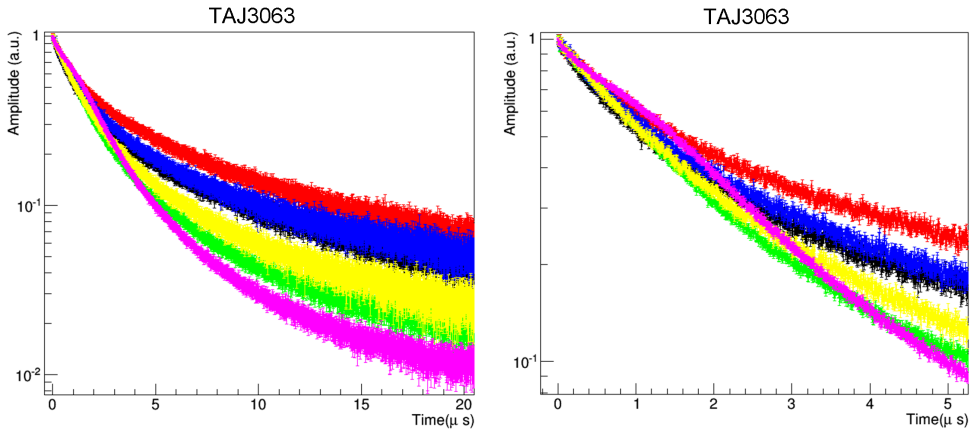


**Figure (5.30).** Normalized luminescence decay from TAJ3063 in log scale. On the right the blow-up of the first 5 $\mu$s is shown.

Figure 5.31 shows the results of the first group, where different colors represent different lapis lazuli origin, and different shades of the same color represent different stones from the same origin. It is possible to see the large spread in the results, even within the same stone, the reason for which is still under discussion. The different lifetimes found could be in fact related to different emission centers, or simply related to variations of the same emission center, or even related to the data analysis procedures. As it was presented in Chapter 3, the fact that a sum of five exponentials represent the decay shape of an emission does not necessarily mean that five emission centers are involved in the luminescence decay. To overcome this issue, as previously done for the decays after short irradiations, here too we calculated the average lifetime within each group (black line) with its standard deviation (dashed red line). The only sample origin whose lifetimes have relatively small spread was Chile. Samples from Afghanistan, Myanmar, Tajikistan and Siberia showed lifetimes above the "average range", and samples from Tajikistan and Siberia also presented lifetimes below the average range. Similarly to what was seen with the results obtained with short pulses (paragraph above), AFG13 showed results significantly different from the other Afghan samples.

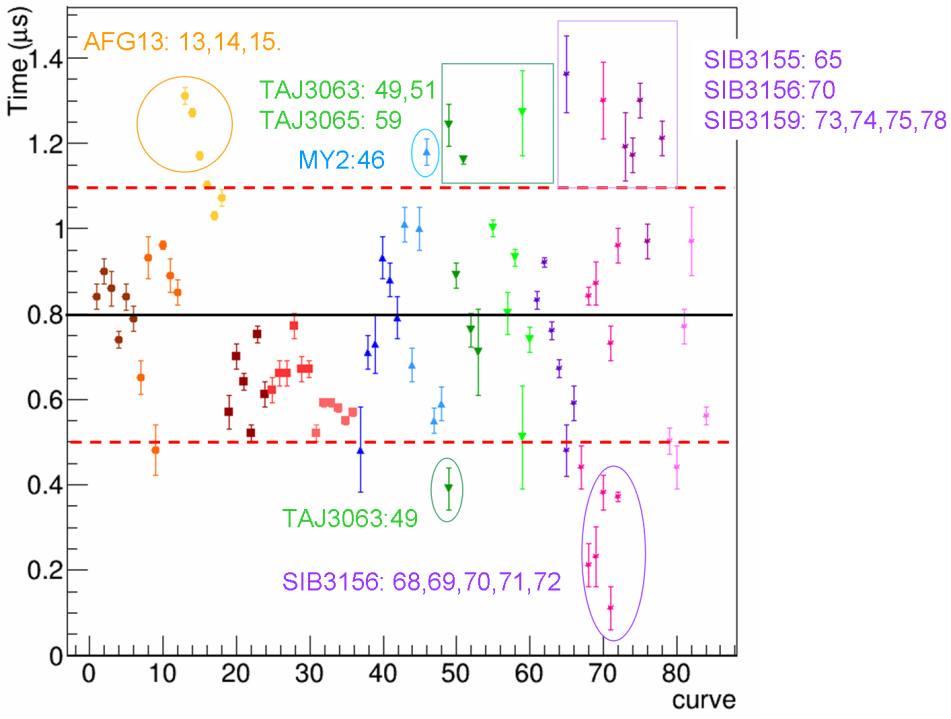


**Figure (5.31).** Lifetimes within the 0-1.5 $\mu$s range (group 1) from all decay curves that could be fitted with a sum of exponential decays. Different colors represent lapis lazuli from different origins: yellow (Afghanistan), red (Chile), blue (Myanmar), green (Tajikistan) and violet (Siberia). Different shades of the same color represents a different stone from the same origin.

Figure 5.32 shows the results of the second group and Figure 5.33 of the third group. In the former, the origins that gave results outside the average range were Chile, Myanmar, Tajikistan and Siberia (above the average), and Myanmar and Siberia (below the average). In the latter, it is clear that Chilean samples have a slower component that contributes substantially to the luminescence decay.

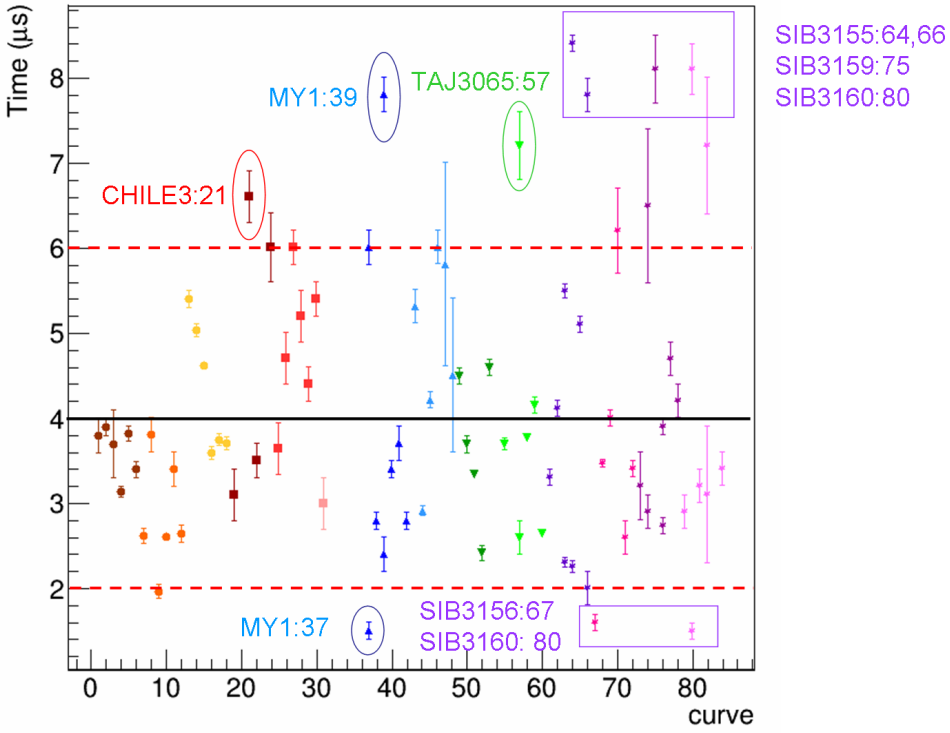


**Figure (5.32).** Lifetimes within the 1.5-9 $\mu$s range (group 2) from all decay curves that could be fitted with a sum of exponential decays. Different colors represent lapis lazuli from different origins: yellow (Afghanistan), red (Chile), blue (Myanmar), green (Tajikistan) and violet (Siberia). Different shades of the same color represents a different stone from the same origin.

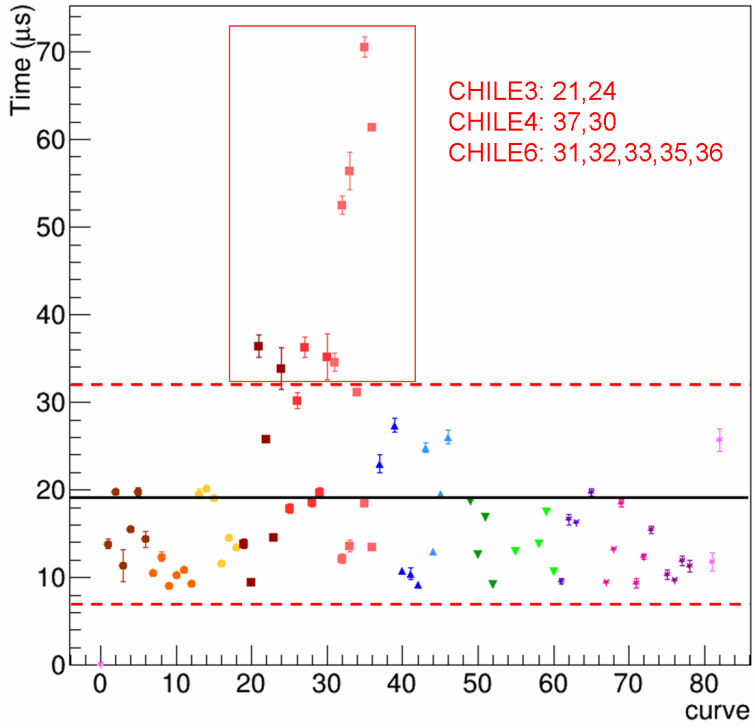


**Figure (5.33).** Lifetimes slower than 10 $\mu$s (Group 3) from all decay curves that could be fitted with a sum of exponential decays. Different colors represent lapis lazuli from different origins: yellow (Afghanistan), red (Chile), blue (Myanmar), green (Tajikistan) and violet (Siberia). Different shades of the same color represents a different stone from the same origin.

The next results to be presented concern the measurements performed in the same way as the ones shown above, i.e., using only the predeflector to deliver a pulse of approximately 1 $\mu$s and an optical filter with a bandwidth at 450±50 nm, irradiating the same areas as already shown in Figures 22-26. The difference was in the beam current used of 20 nA. We have thus seen that the temporal behavior of luminescence decay of lapis lazuli, in the bandwidth of 450±50 nm, change when increasing the beam current while maintaining all other parameters the same.

We have seen that when irradiating the samples with 20 nA, a sort of "plateau" shows up in some curves, with more or less evidence. To better comprehend, Figure 5.34 shows the rise and decay of the signals obtained from CHILE6 and AFG2, without wavelength discrimination, irradiated with a beam current of 20 nA. Notwithstanding the similar maximum intensities of the curves, in CHILE6 the effect is not observed, while it is seen in all the curves from the AFG2 sample.

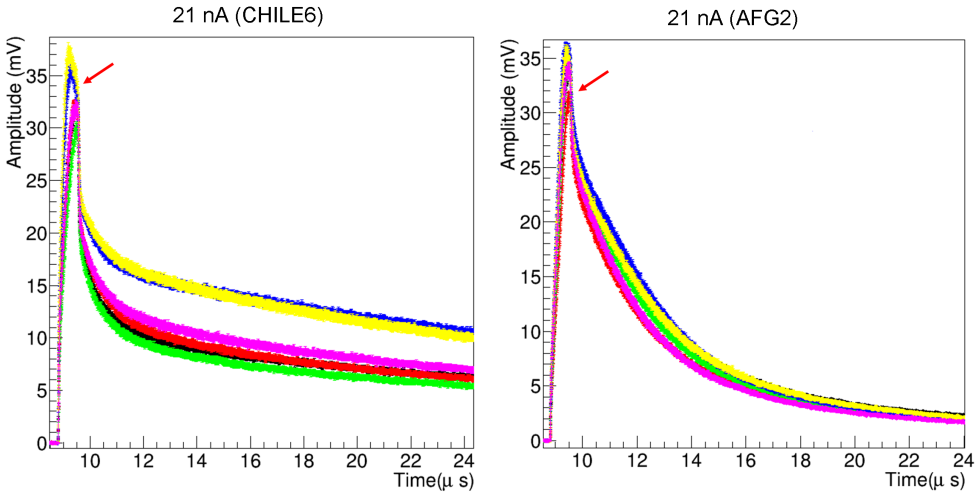


**Figure (5.34).** Luminescence rise and decay from CHILE6 (left) and AFG2 (right) obtained by irradiating the sample with a beam current of 20 nA during 1 $\mu$s. No wavelength discrimination was performed. The red arrow indicates the instant the excitation is switched off.

In order to have a better insight into this behavior, we went back to the standard scintillators (BC-408 and $CdWO_4$) and submitted them to a simple test. Figure 5.35 shows the signals obtained from BC-408 (top) and $CdWO_4$(bottom) by irradiation with several beam currents during 800 ns. If the presence of the "plateau" in the signals was a PMT artifact, we would expect it to appear after a certain working threshold, for example, at high luminescence intensities. As can be seen, in the case of the results obtained from BC-408, the plateau appears certainly only when the luminescence peak was higher than 150 mV. Instead, the results from $CdWO_4$ show that already at 30 mV of the luminescence peak the decay signal presented the plateau, which indicates that it is not a threshold in the luminescence peak to produce malfunctioning - if any - of the PMT. It is to be noted that, in a similar way, also the luminescence behavior of the lapis lazuli samples observed in Figure 5.34 does not depend on the luminescence peak intensity during excitation.

A further consideration can be done considering the signal behavior during the excitation phase of the two scintillators. Both BC-408 (top right) and $CdW0_4$ (bottom right)

show one or more peaks, indicated by the black arrows, increasing with increasing beam current, and at different times; then, still during excitation, these signals decrease (this is much more evident for BC-408) until the excitation is switched off, indicated by the red arrow. The shape of the decay curve, after the excitation is switched off, seems to be related to the signal behavior during excitation. This might indicate that the plateau behavior on the results comes from real recombination process in the material.

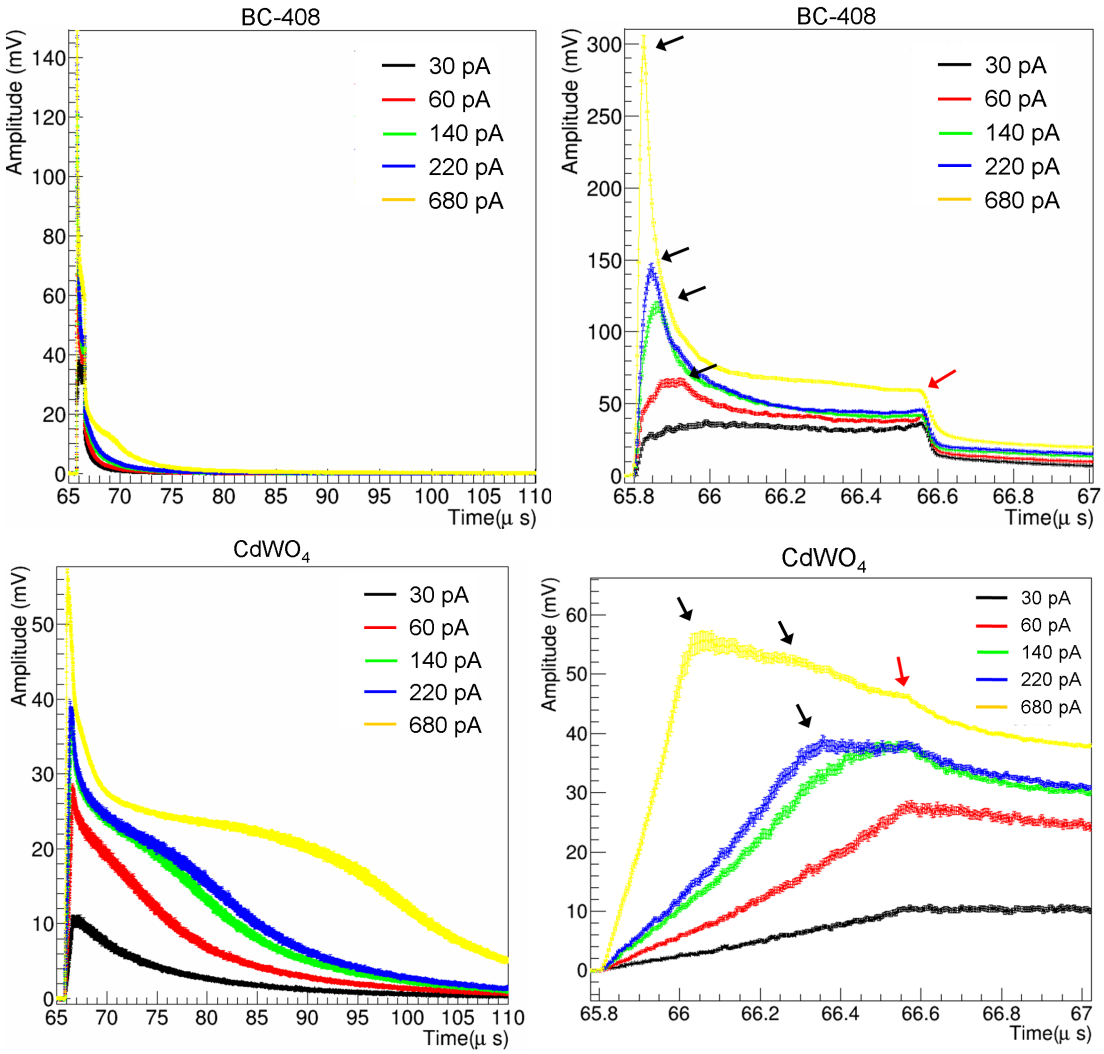


**Figure (5.35).** Top left: Luminescence rise and decay of BC-408 taken with different beam currents. Top right: Same as top left bu with a blow-up of the horizontal scale during and immediately after excitation, and vertical axis at full scale. Bottom left: Luminescence rise and decay of $CdWO_4$ taken with different beam currents. Bottom right: Same as bottom left but with a blow-up of the horizontal scale during and immediately after excitation. The red arrows on the images on the right indicate the moment the excitation is switched off. The black arrows indicate "peaks" on the signal seen even during excitation.

To emphasize and clarify, Figure 5.36 shows the signals obtained from AFG13 (top) and TAJ3063 (bottom) during excitation (left) and normalized after excitation (right), using beam currents of 4 (black curves), 20 (red curves) and 60 nA (green curves). Also in these sample, as in the scintillators, we can observe the presence of peaks also during the phase of excitation[3]. Looking at the signals after the excitation is switched off (blue

[3]The signal during excitation might be related to the population dynamics of the luminescence centers.

arrow), it is possible to see the appearance during the decay of "peaks", indicated by black arrows. They might be related to the presence of the peaks seen during excitation. Moreover, the red curve from TAJ3063 shows a peak during excitation, indicated by the red arrow, that is not seen on other curves (considering also the ones from AFG13). The interpretation of this circumstance is all but obvious, but even if only empirically, the observation of the luminescence during a relatively long excitation might indicate another method for comparing samples. We are still investigating this aspect of the results, and in the following of this thesis it will not be anymore considered in our analysis.

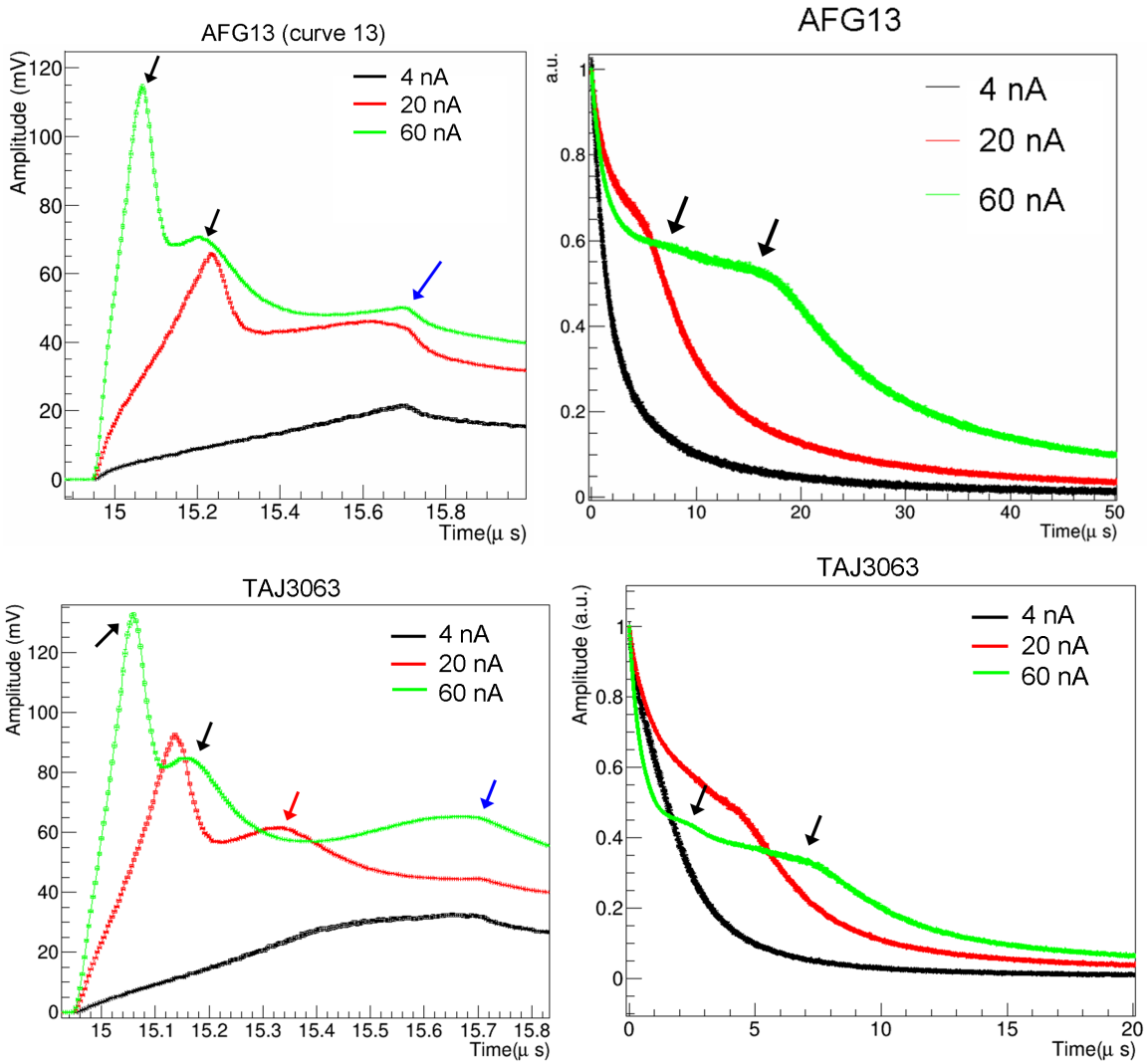


**Figure (5.36).** Luminescence signals from AFG13 (top) and TAJ3063 (bottom) during excitation (left) and normalized after the excitation was switched off (right). Blue arrows represent the instant the excitation was switched off. Black arrows indicate "peaks" in the luminescence intensity and the red arrow indicates a "peak" not seen in any of the other shown curves.

As exemplified in Figure 5.37 , concerning the presence of the plateau in the luminescence decays obtained with the beam current of 20 nA, some samples did not show any indication of its presence (Figure 5.37 on the left). In others, some curves presented this "particular" behavior while other curves did not (Figure 5.37 in the middle). And in some samples, all decay curves presented the plateau (Figure 5.37 on the right).

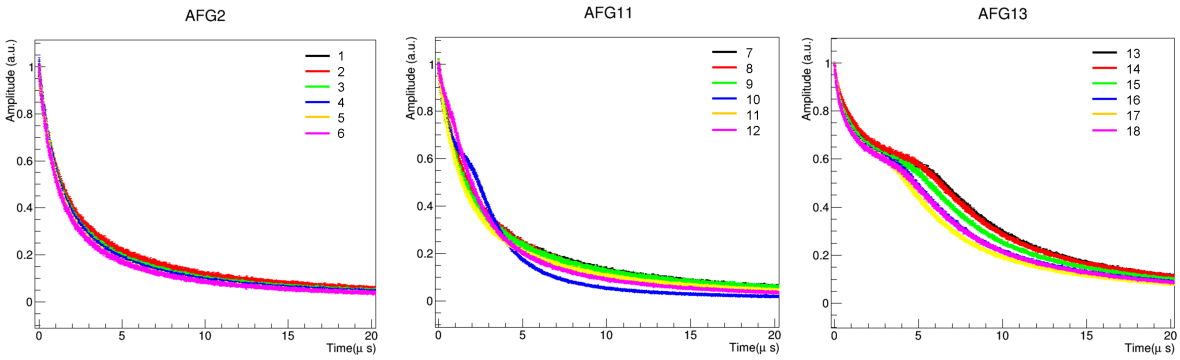


**Figure (5.37).** Normalized luminescence decays from AFG2, AFG11 and AFG13 obtained with a beam current of 20 nA, showing the presence of a plateau in some of the decays.

Since, from the results presented so far concerning the non-exponential behavior of some of the obtained signals, this behavior seems to be real and not an instrumental artifact, we considered these curves in our analysis. In order to account for the signals with the plateau, since we could not find a mathematical expression that might describe the decay, the average lifetime was calculated as:

$$\langle t \rangle = \frac{\int_0^{t'} tI(t)dt}{\int_0^{t'} I(t)dt}. \tag{5.1}$$

The time $t'$ was taken when the signal intensity decreased to approximately 5% of the intensity at $t = 0$. It is important to keep in mind that, since we are not discriminating the components of the decay, when calculating the average decay time the concentration of the emitting centers takes part in the effective emission decay time obtained. For this reason more consistency in the results is needed to account for concentration variation in the samples. Of course, the results presented here give only indications about possible discrimination using this parameter (average decay time) since more statistics is needed to give more reliable results.

Figure 5.38 shows the mean lifetimes calculated. The black line represented the average of the calculated mean lifetimes and the dashed red lines the average plus/minus one standard deviation. Although some clustering might inferred for the MY and TAJ samples, altogether no conclusive evidence of provenance differentiation can be derived from this analysis.

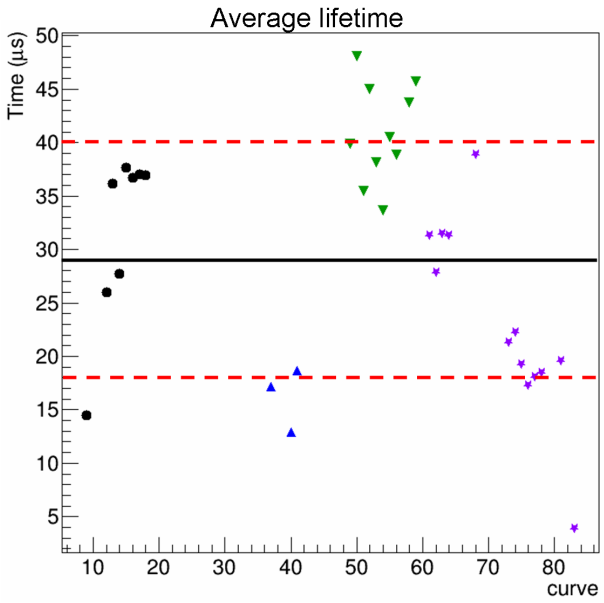


**Figure (5.38).** Mean lifetime calculated from the curves that presented a plateau in their luminescence decay when irradiated with a beam current of 20 nA. Samples from Afghanistan are shown in black, from Myanmar in blue, from Tajikistan in green and from Siberia in violet.

A multi-exponential fit was instead performed for the curves that did not present the plateau in their luminescence decay. The calculated lifetimes, as previously, were divided in groups, considering only the components that contributed to at least 5% on the decay, as the following: group 1 (decay times faster then 2 $\mu$s), group 2 (lifetimes between 2 and 10 $\mu$s), group 3 (lifetimes longer than 10 $\mu$s). The results can be seen in Figure 5.39 (group 1 on the left, group 2 in the middle, group 3 on the right). From the Figure, a possible marker can be inferred from group 3, that shows that the lifetimes from CHILE present longer values than the ones from the other origins.

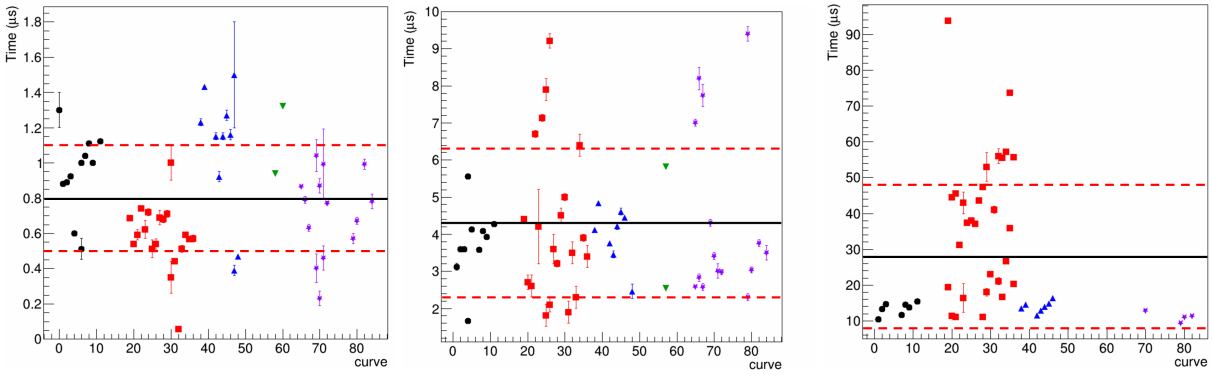


**Figure (5.39).** Lifetimes obtained by performing a multi-exponential fit on the curves corresponding to irradiations with 20 nA where no plateau was observed. Circles in black represent Afghan samples, red squares represent Chilean samples, upwards blue triangles represent samples from Myanmar, samples from Tajikistan are represented by downwards green triangle, and samples from Siberia are represented by violet stars.

Finally, still concerning the luminescence emission detected in the wavelenth range 450±50nm, irradiations with a beam current of 60 nA were also performed. While in some samples all irradiated areas presented a complex behavior, such as TAJ3063 shown in Figure 5.40 on the left, in others some areas still presented a multi-exponential decay,

as for example some of the irradiated points in SIBERIA3160, shown in Figure 5.40 on the right. Since most of the decay curves obtained in these measurements presented a complex shape that could not be represented by a sum of exponential decays, the effective emission decay (average lifetime) was calculated for all the decays.

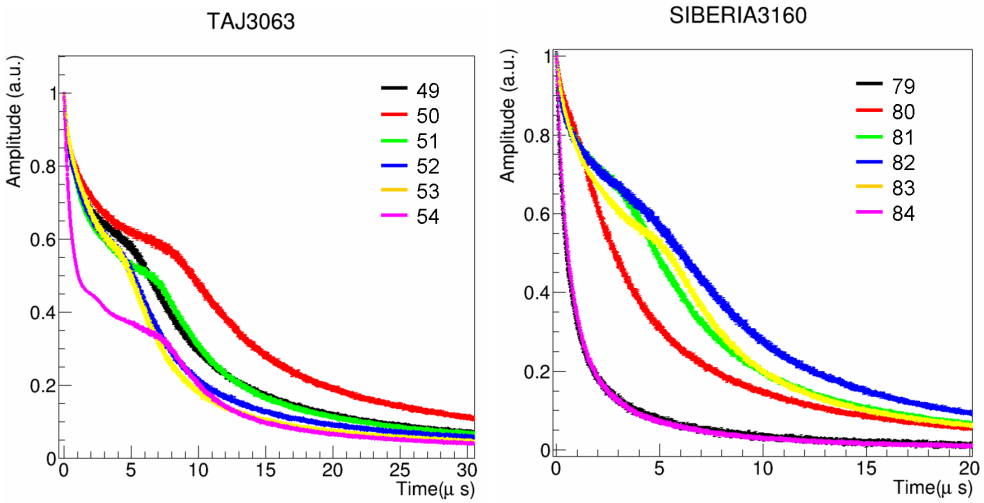


**Figure (5.40).** Luminescence decays from TAJ3063 (left) and SIBERIA3160 (right) obtained irradiating the samples with a beam current of 60 nA.

The results for the average lifetimes are shown in Figure 5.41: black circles represent Afghan samples, red squares represent Chilean samples, upwards triangles represent samples from Myanmar, downwards triangles represent samples from Tajikistan, and violet stars represent samples from Siberia. It is possible to say that Chilean samples are clearly distinguished from the others by possessing longer average lifetime (of the order of hundreds of $\mu$s). As it has been already seen in the previous results from time-resolved and steady-state measurements, AFG13 results (indicated by the black circle) are significantly different than the results from the other Afghan samples (AFG2 and AFG11). In some cases, AFG13 shows results that are more similar to those obtained from the samples from Tajikistan. One of the main difficulties about working with these mineral samples is that, in the case of the Afghan samples used in this work, the exact mine from where they come is not specified. We might be working with samples from different mines that might possess different composition.

Concerning the values obtained for the average lifetime, while most of the results obtained from the Afghan samples (AFG2 and AFG11) stayed around 20 $\mu$s, as well as those from the samples from Myanmar, the average lifetimes obtained from the Siberian samples are more scattered, going from few $\mu$s to around 50 $\mu$s. We notice that the average lifetime calculated from these curves, even though derived "blindly", i.e., without knowing the reason for the plateau seen in the decay curves, can anyway be an empirical discrimination criterion of provenance.

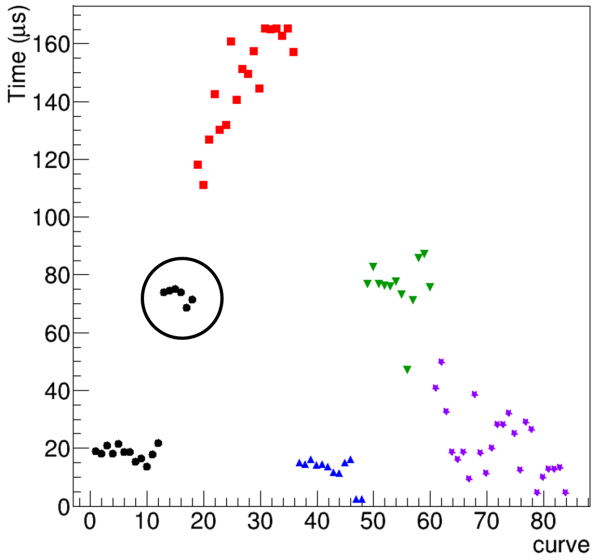


**Figure (5.41).** Average lifetimes calculated from the results obtained by irradiating lapis lazuli with 3 MeV protons, a beam current of 60 nA and excitation time of 1 $\mu$s. The x-axis is the curve number. Samples from Afghanistan are shown in black: AFG2 (curves 1-6); AFG11 (curves 7-12); and AFG13 (curves 13-18) that are indicated by the black circle. Samples from Chile are shown in red (three samples, CHILE3, CHILE4 and CHILE6), from Myanmar in blue (MY1 and MY2), from Tajikistan in green (TAJ3063 and TAJ3065) and from Siberia in violet (SIBERIA3155, SIBERIA3156, SIBERIA3159 and SIBERIA3160). For a more detailed discussion see text above.

Next, the results obtained placing the high pass optical filter with the cutoff at 495 nm in front of the PMT window will be presented. In this measurement set, beam currents of 4 nA, 20 nA and 60 nA were used, as in the previous measurements presented. The lapis lazuli zones irradiated were the same as the ones shown in Figures 5.17-5.21. Since the PMT is less efficient in the wavelength range $>$ 500 nm, the PMT output in these measurements was considerably lower than the ones obtained previously with the 450$\pm$50 nm filter. For this reason, when using a beam current of 4 nA during 1 $\mu$s, not all irradiated areas gave a signal with enough statistics for the proper analysis to be performed. In fact, none of the Chilean samples provided a signal high enough for analysis (with the beam current of 4 nA), in spite of the fact that, when measuring the luminescence spectra under continuous irradiation, they were some of the samples that provided the highest counts in this wavelength region.

Most of the curves could be fitted by a sum of exponentials (three exponentials for the measurement with 4 and 20 nA of beam current, and up to five exponentials for the measurements with 60 nA). Also in this case, the lifetimes were divided in three groups: group 1 contains the lifetimes in the range 0-2 $\mu$s; group 2 contains the lifetimes in the range 2-10 $\mu$s; and group 3 contains the lifetimes $>$ than 10 $\mu$s. Figure 5.42 shows the results obtained with the beam current of 4 nA for the group 1 (left), group 2 (middle) and group 3 (right), where once again only the components that contributed to at least 5% to the emission were considered. The black line represents the average taken considering all lifetimes within a group, and the dashed red lines represent the average plus/minus one standard deviation. Due to the lack of luminescence intensity in this set of irradiation, the uncertainties on the results are higher than the ones obtained with the previous optical

filter. The fact that Chilean samples do not enter in any of the groups shown in Figure 5.42 is itself already as a way to discriminate between lapis lazuli from Chile and the others. Considering the results in the three groups, it is only possible to say that the first Afghan sample (AFG2, points 1-6) shows a distinctly different behavior than the others, both from Afghan and other origins.

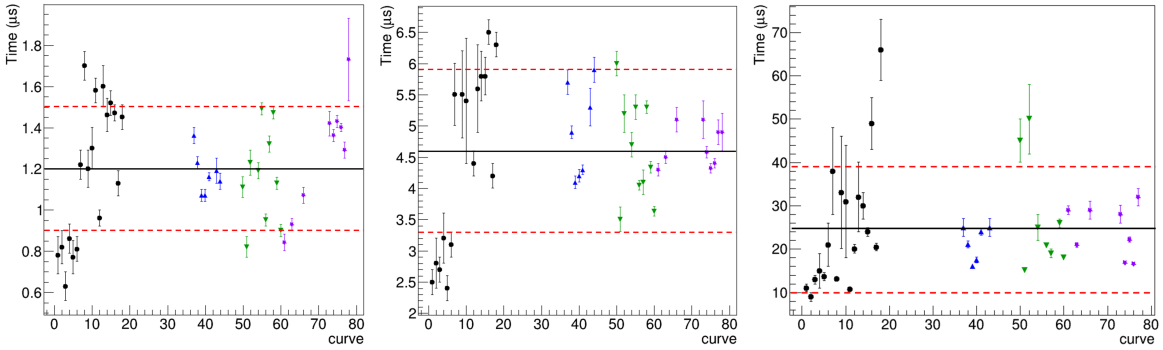


**Figure (5.42).** Lifetimes obtained by performing multi-exponentials fits to the results from irradiations with 4 nA of beam current, and performing wavelength discrimination with the use of a high-pass filter at 495 nm. Group1 ($\tau < 2$ $\mu$s is shown on the left, Group2 (2 $\mu$s $< \tau <$ 10 $\mu$s ) is shown in the middle, and Group3 ($\tau > 10$ $\mu$s) is shown on the right. Black circles represent Afghan samples, upwards blue triangles represent samples from Myanmar, downwards green triangles represent samples from Tajikistan, and Siberia samples are represented by violet stars.

Differently from what was observed with the measurements performed with the previous optical filter (450±50 nm), in this set of measurements, when using a beam current of 20 nA, most decay curves could still be described by a sum of exponentials (mostly 3 exponentials). The results are shown in Figure 5.43 for the group 1 in the left, group 2 in the middle and group 3 on the right. Group 1 shows that Tajikistan samples do not have lifetimes faster than 1 $\mu$s. Also, some points in Siberian samples present considerably faster lifetimes. Groups 2 and 3 show that also in the wavelengths $>$ 495 nm Chilean samples present longer lifetime components than samples from the other studied origins.

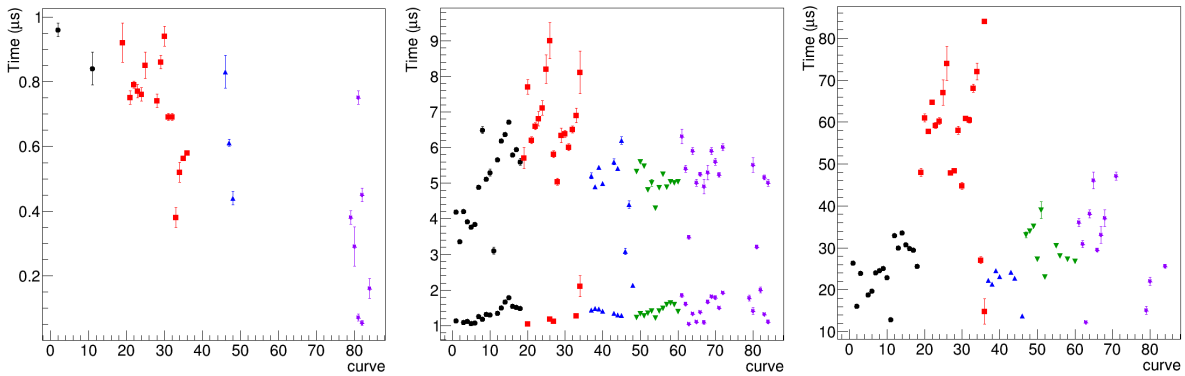


**Figure (5.43).** Lifetimes obtained by performing multi-exponentials fits to the results from irradiations with 20 nA of beam current, and performing wavelength discrimination with the use of a high-pass filter at 495 nm. Group1 ($\tau < 1$ $\mu$s is shown on the left, Group2 (1 $\mu$s $< \tau <$ 10 $\mu$s ) is shown in the middle, and Group3 ($\tau > 10$ $\mu$s) is shown on the right. Black circles represent Afghan samples, red squares represent Chilean samples, upwards blue triangles represent samples from Myanmar, downwards green triangles represent samples from Tajikistan, and Siberia samples are represented by violet stars.

The results concerning measurements performed with a beam current of 60 nA are

shown in Figure 5.44 for group 1 on the left, group 2 in the middle and group 3 on the right. Here, in contrast to what was seen in the results obtained with the 450 nm optical filter, most of the curves could be fitted with a sum of four or five exponentials. No significant differences can be seen from the results shown in Figure 5.44.

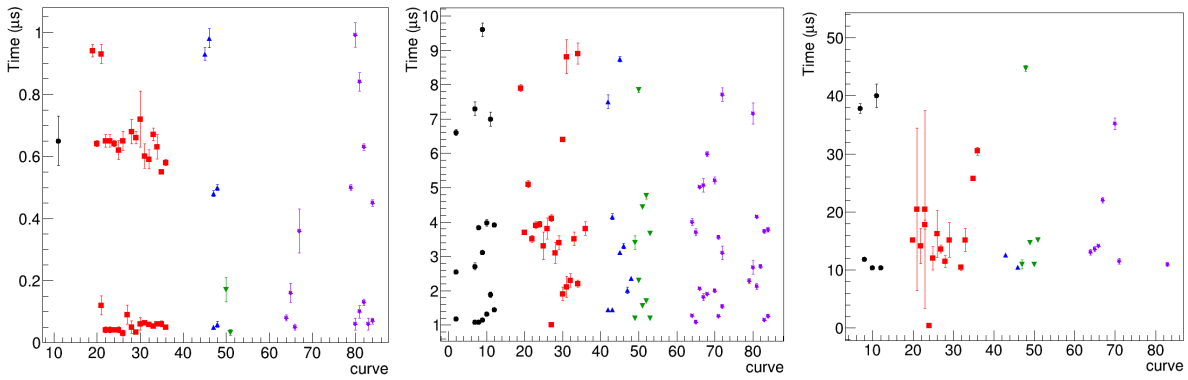


**Figure (5.44).** Lifetimes obtained by performing multi-exponentials fits to the results from irradiations with 60 nA of beam current, and performing wavelength discrimination with the use of a high-pass filter at 495 nm. Group 1 ($\tau < 1$ $\mu$s is shown on the left, group 2 (1 $\mu$s $< \tau <$ 10 $\mu$s ) is shown in the middle, and group 3 ($\tau > 10$ $\mu$s) is shown on the right. Black circles represent Afghan samples, red squares represent Chilean samples, upwards blue triangles represent samples from Myanmar, downwards green triangles represent samples from Tajikistan, and Siberia samples are represented by violet stars.

Concerning the curves that could not be fitted with a sum of exponential curves, as in the previous cases the mean lifetime per each curve was calculated, and the results can be seen in Figure 5.45. Similarly to what was observed from the results taken with the optical filter of 450 nm, Chilean samples present longer average lifetimes than others. However, at the higher wavelength range, this longer average lifetime is found for some irradiated points only, while at the lower wavelength range, this happens for all the irradiated points.

The measurements at two different wavelength ranges were initially planned just as an attempt to find clear differences in the decay behavior on the luminescence from the samples. Instead, as a final comment, from the results obtained with the two filters we can say that - apart from the just mentioned difference for the Chilean samples - it turned out that no other differentiation can be detected concerning the lifetimes obtained: in both sets of measurements lifetime components were found in all the ranges, from tens of nanoseconds to tens of microseconds.

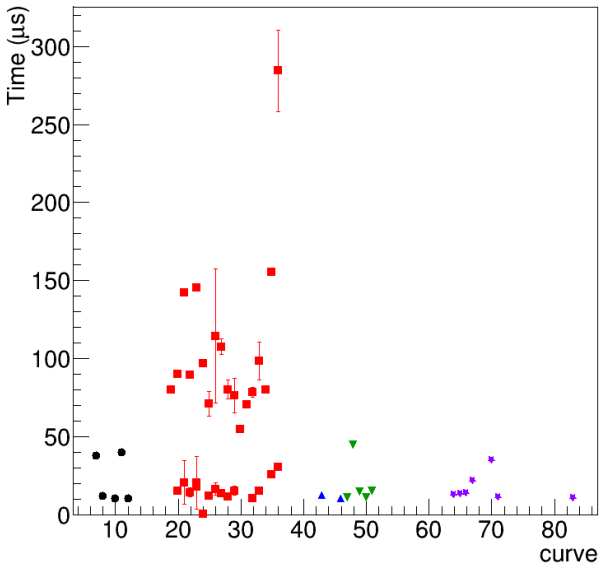


**Figure (5.45).** Average lifetimes calculated from the curves that could not be fitted with a sum of exponential decays. Irradiation were performed with a beam current of 60 nA and wavelength discrimination was done with the use of a high-pass filter at 495 nm. Black circles represent Afghan samples, red squares represent Chilean samples, upwards blue triangles represent samples from Myanmar, downwards green triangles represent samples from Tajikistan, and Siberia samples are represented by violet stars.

## 5.4 CARBON IONS RESULTS

In this paragraph, the results obtained irradiating lapis lazuli with $^{12}C$ of 10 MeV will be presented. Performing irradiations with carbon ions was not a trivial operation since never previously had heavier ions than protons been used to produce pulsed beams on the DEFEL line. However, as mentioned in Chapter 4, it was considered that tests with heavier ions might be worth the effort, because the penetration depth of these ions is much shorter than for 3 MeV protons, thus exciting only more selectively only near surface layers.

The measurements were carried out irradiating up to two areas per sample with a beam current of approximately 50 nA. The irradiation time was of approximately 1 $\mu$s using only the predeflector for beam chopping. Wavelength discrimination was performed by the use of a 500 nm high-pass optical filter. Figure 5.46 shows the luminescence decays obtained for the lapis lazuli samples: Afghanistan on top left, Chile on top middle, Myanmar on top right, Tajikistan on bottom left, Siberia on bottom middle. A blow-up of Siberia3159 in log scale is also shown on bottom right to point out a very subtle concave shape in the first part of the decay, which is the reason why a fit with a sum of exponentials could not be performed for this sample.

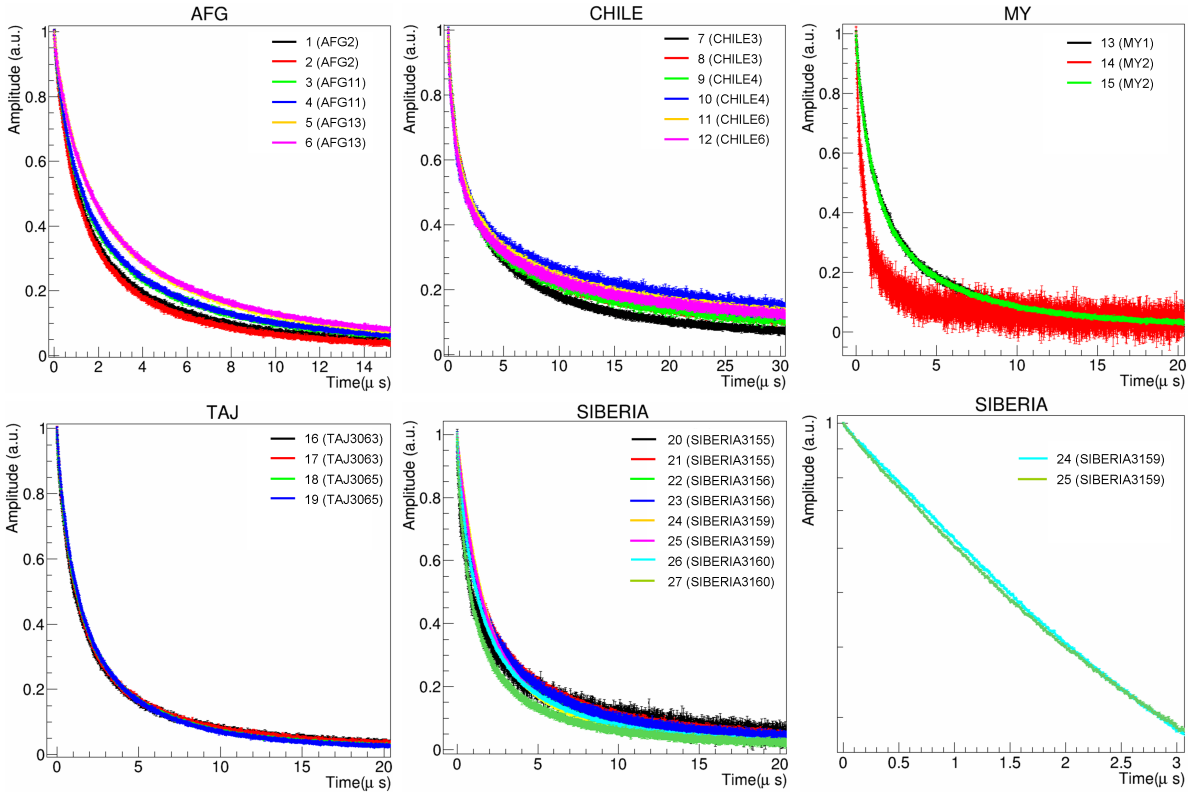


**Figure (5.46).** Normalized decay curves taken from lapis lazuli samples by irradiation with $^{12}$C ions and a beam current of 50 nA.

The curves from Figure 5.46 were fitted with a sum of four-five exponentials, except as mentioned for the ones from SIBERIA3159. The lifetimes obtained from the fits were divided, here too, in three groups (see Figure 5.47): group 1 on the left ($0<\tau<1$ $\mu$s); group 2 in the middle ($1<\tau<10$ $\mu$s); and group 3 on the right ($\tau>10$ $\mu$s). The results show that no distinction can be performed by group 1 and group 2. Instead, only the Chilean samples and two points from the Siberian ones have lifetime components in group 3 contributing significantly (at least 5%) to the total emission. Once again, therefore, Chilean samples presented longer lifetime components than the other samples.

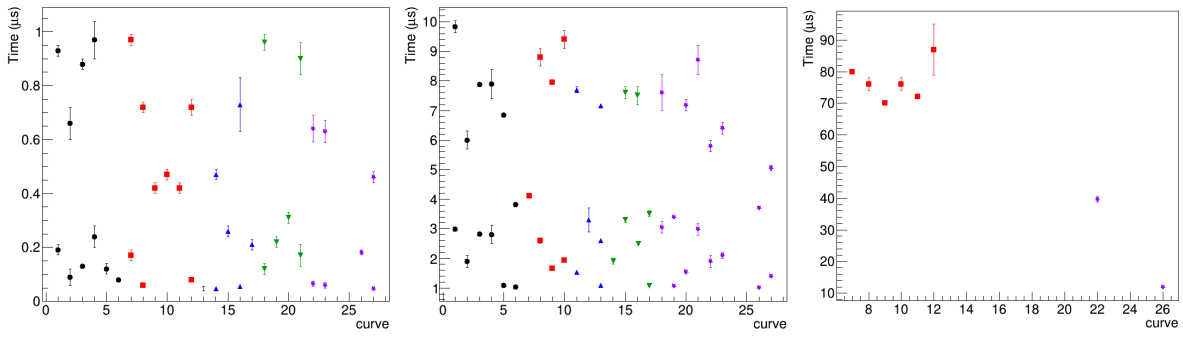


**Figure (5.47).** Lifetimes obtained by performing a multi-exponential fit of the curves shown in Figure 5.46. Group1 ($\tau < 1$ $\mu$s) is shown on the left, group2 ($1$ $\mu$s $< \tau < 10$ $\mu$s) is shown in the middle, and group 3 ($\tau > 10$ $\mu$s) is shown in the right. Black circles represent Afghan samples, red squares represent Chilean samples, upwards blue triangles represent samples from Myanmar, downwards green triangles represent samples from Tajikistan, and Siberia samples are represented by violet stars.

As a final general comment to all the reported results, one can observe first of all that only one approach of measurement conditions and data analysis is not enough to

provide significant markers to distinguish the lapis lazuli provenances, as one might have optimistically expected, but proved to be unrealistic. Nevertheless, from the whole of the measurements performed, a number of hints can be already extracted that, after deeper investigations that are envisaged to be done in the near future, might eventually lead to some stronger evidence of discrimination.

Table 5.1 shows a sort of recapitulation of what it has been possible to extract with reasonable evidence from the entire set of the measurements performed. The list of lapis lazuli origins studied in the thesis is reported in the different lines (AFG13 is left separated from the other Afghan samples because of some "anomalous behavior" it presented in the results obtained under all the different sets of measurement conditions). The columns correspond just to the different sets of measurements, each marked by a differently colored sphere: red for the measurements performed with 3 MeV protons, beam current of 100 nA, and irradiation of approximately 10 ns; blue, green and orange for the measurements performed with 4, 20 and 60 nA of beam current respectively, all with 1 $\mu$s irradiation with 3 MeV protons, and performing wavelength discrimination at 450±50 nm; pink, light blue and black correspond to measurements performed with 4, 20 and 60 nA respectively, still with 1 $\mu$s irradiation with 3 MeV protons but with the high-pass optical filter with the cutoff at 495 nm; finally, yellow corresponds to the set of measurements performed with carbon ions, 50 nA of beam current, and wavelength discrimination using the high-pass optical filter with the cutoff at 500 nm. For each lapis lazuli origin, a sphere was placed in the columns corresponding to the measurement conditions, for which that origin gave at least an indication of a different luminescence response behavior than the others (providing a way to be possibly discriminated). Even though the decision to assess a discrimination of a certain origin in a set of measurement can be critical and subjective, we consider the presence of a sphere under many columns for a given origin a stronger indication than if only few spheres are present. For instance, with their distinctly different behavior under many conditions, Chilean samples showed in our opinion good evidence that TRIBIL measurements, performed in the different conditions we used, make it possible to discriminate this origin from the others.

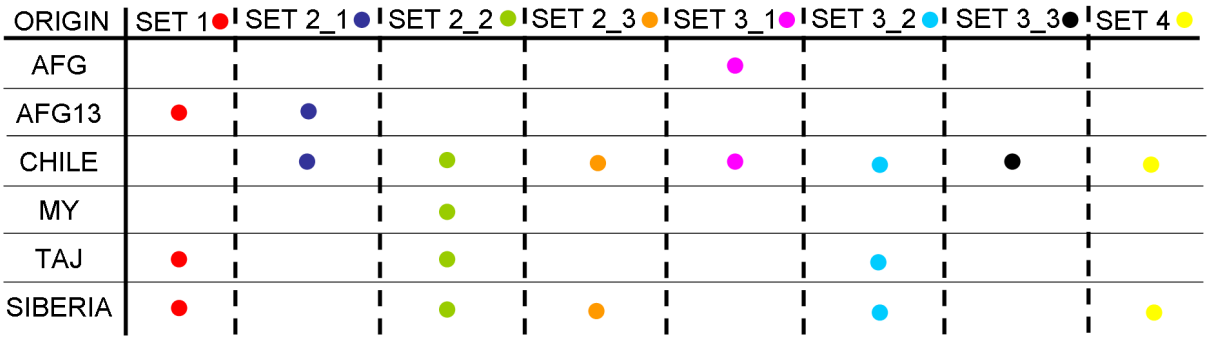


**Table (5.1).** Table containing the list of origins studied in the thesis. Each set of measurements is represented by a different colored sphere, and each time an origin can be discriminated in a particular set of measurements, the sphere of the corresponding color is placed in the column. Red spheres represent the measurements performed with 3 MeV protons, beam current of 100 nA, and irradiation duration of approximately 10 ns. Blue (for 4 nA), green (for 20 nA) and orange (for 60 nA) correspond to the irradiations performed with 3 MeV protons, and wavelength discrimination using the 450±50 nm optical filter. The set of measurements performed with 3 MeV protons and wavelength discrimination using the high-pass filter with the cutoff at 495 nm are represented by the pink (4 nA), light blue (20 nA) and black (60 nA) spheres. The yellow spheres represent the measurements performed with carbon ions, 50 nA of beam current and wavelength discrimination using the high-pass optical filter with the cutoff at 500 nm.

In conclusion, maybe lapis lazuli was a much too complex material to allow us to extract simple differentiation criteria. However, there are still other ways to probe a target using the TRIBIL setup developed at LABEC, which means that strong markers can still be "hidden" in the world of possibilities. Studies concerning the formation of defects, such as the change of luminescence yield during irradiation, as already pointed out in this Chapter, are one of the many possible ways to characterize materials. In addition, future improvements on the setup and the analysis method can be done, aimed at the detection of faster lifetimes, and/or more stringent wavelength discrimination (using narrower bandwidth optical filters), which however implies the need of improving the luminescence collection efficiency to collect enough statistics.

# CHAPTER 6

# DESIGN AND REALIZATION OF A SCANNING XRF SYSTEM

As mentioned in the Introduction, another of my activities at LABEC during the three years of my PhD was the development of the first XRF scanning system of the laboratory. As well known, XRF (X-Ray Fluorescence) is a technique of elemental composition analysis, very useful to the Cultural Heritage studies because it gives important information about artworks, such as the identification of pigments in the paintings, and the verification of their conservation state. The working principle is the same as in PIXE (Chapter 1): X-ray emission is induced from the atoms of a target through the ionization of their inner shells and the subsequent electron transitions from outer shells. However, what produces the inner shell ionization is in XRF the photoelectric effect by a beam of primary X-rays of the order of typically few tens of keV, rather than the bombardment with a beam of ions in the MeV range as it is in PIXE. Both PIXE and XRF provide multi-elemental analysis, although the different excitation mechanism results in different characteristics of the two techniques, with pros and cons of each. For instance, owing to the photoelectric cross section trend vs Z, XRF is much less efficient than PIXE for the detection of low-Z elements, but has higher X-ray yields for high-Z elements. Also, the probed depth from surface is considerably higher with XRF than with PIXE (at least for the higher-Z elements[1]), owing to the larger penetration of the primary photons with respect to the ions used for PIXE[2].

A very important consideration in comparing PIXE with XRF comes from the fact that some artworks can not be moved from the site where they are kept, either because of their size, or because their owners or the museum curators do not give their permission, or more simply - as e.g. in the case of mural paintings - because moving them to a laboratory is physically impossible. Thus, the fact that XRF systems, using a simple small X-ray tube as exciting source, can be a transportable instrument, is an advantage of this technique in comparison to PIXE measurements, for which the artwork must be

[1]This is due to the fact that low-Z elements emit only low-energy X-rays, so that even though the atoms can be excited more in depth, the emitted X-rays are anyway strongly absorbed in the material itself except for the emitting atoms in the very surface layers.

[2]The larger probed depth of XRF for high Z elements (emitting instead higher energy X-rays, much less absorbed in the material), can be a pro or a con, depending on the problem under investigation. Sometimes a selectivity to the very surface layers may be advantageous (when the contribution of the substrate should be avoided) while in other cases it is a limit.

necessarily carried to an accelerator facility.

In the traditional manner, a XRF spectrometer is used for single point measurements, i.e., one small area is irradiated and one spectrum is taken at a time. The possibility of performing XRF analysis of a larger area over which reconstructing the space distribution of the various detected element, by scanning the region of interest, has been shown to be of great use because it overcomes the limitations of the point by point measurements. For instance, being able to place the measurement points in the context of an image allows for discrimination of anomalous zones and areas of major interest.

My work for the development of the XRF system, which included software and hardware development, was performed in collaboration with colleagues at the laboratory. The first version of the scanning system was used in museums in the framework of several collaborations between the laboratory, historians of art and restorers. In this Chapter, a description of the prototype and its mode of operation will be given, along with examples of its applications to some artworks and of some first preliminary investigations also performed on some lapis lazuli stones studied with TRIBIL in this thesis.

## 6.1 INSTRUMENTATION

The measurement head (Figure 6.1) of the instrument consists of an X-ray tube (Moxtek with 40 kV of maximum voltage and 0.1 mA of maximum anode current) and a SDD detector (Amptek/XR100, 25 $mm^2$ x 500 mm). They are placed at 45° with respect to each other, with the X-ray tube placed so that the beam is perpendicular to the target. The X-ray tube has a chromium anode[3], and in front of the tube exit window there are two collimators: one of Pb, 15 mm long and 3 mm of aperture; and one of Cr, with apertures that can be changed from 0.3 to 1 mm.

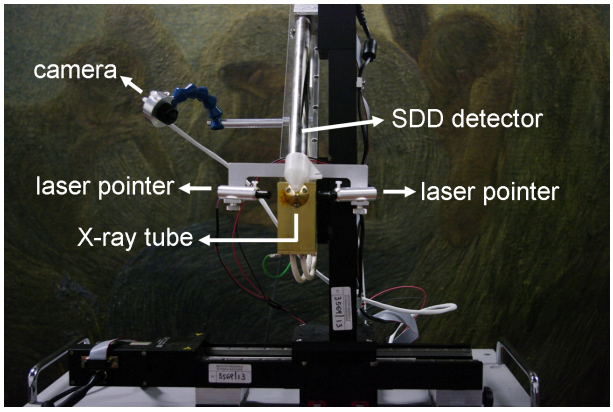


**Figure (6.1).** Front view of the measurement head of the XRF scanning system of LABEC.

Additional elements are also placed in the measurement head for positioning and monitoring purposes. In order to correctly select the irradiation zone, two laser pointers are installed, each one at 45° relative to the direction of the X-ray beam. Also, a camera connected through Ethernet to a computer is placed in the measurement head in order

[3]Tubes with different anodes, and maximum voltage and current, have also been used during the development of the system.

for the operator to have a clear view of the irradiation area also while staying afar (which is necessary to comply with radiosafety regulations).

The measurement head is placed on a linear stage (PI/M-404.8PD Physik Instrumente) that can be moved in three axis. Each axis of the linear stage motion is controlled by a DC controller (MercuryTM/C-862) that communicates with a computer through serial/USB connection. The linear stage, in turn, is placed on top of a box that contains the power supplies (such as those for the motors) and an analog-to-digital converter (CAEN DT5780) of the signal from the detector.

The preamplified signal from the SDD detector is sent to the ADC, which communicates with a computer through an optical link. A particular board (PCI Express) installed in a computer (CAEN/A3818) allows for the optical signal to be processed. This connection is intrinsically fast, which is needed for acquisition when large amounts of data are transmitted, so that no information is lost.

The overall system, which we will call from here on "measurement station" (linear stages, instruments, power supplies box) is 70 x 70 x 40 $cm^3$. Considering transportation, the main parts that must be carried are: the measurement station, a computer for control from afar, and the radioprotection system.

Radioprotection security is actuated through 4 independent, light and easy-to-move fence posts, which are normally positioned as to form a square of approximately 4 $m^2$ to delimit a no access area, equipped with reflectors and Sick/Wl4 photocells. If a person crosses the line defined by a pair of posts, the interlock system turns off the X-ray tube, and the system can only be switched on after clearance of the area. A red light switches on when X-rays are emitted, and an emergency button is also present that manually switches off the tube when pressed. The radioprotection system is controlled by in-house developed hardware.

## 6.2 ACQUISITION AND LINEAR STAGE CONTROL SOFTWARE

By using the Qt Platform, a software was developed in-house to scan an area to be investigated and construct a map where each pixel contains two types of information: the x-y position and the X-ray spectrum acquired while the stage was within that pixel. The maximum dimensions of a map can be of (20 x 20 $cm^2$). The first parameters to be set, once the area dimension has been selected, are the scan velocity, that can reach up to 50 mm/s, and what we might call the "scanning step", for which the minimum value that can be set is 0.25 $\mu$m. Indeed, although the stage moves continuously, a "step" can be defined, in the sense that only after a travel of the stage equal to the selected step value, the coordinates associated to the pixel are changed (by a quantity equal to the step). Having a continuous stage movement instead of a step-motor system is an advantage, because in the latter system data are only acquired while the stage is at rest at each position. Our method increases the data acquisition efficiency because it eliminates the dead times during the movement from one position to the next one, which characterize the step-motor controlled systems.

The selected "step values" (in the sense just explained) define therefore the actual area dimension of each pixel; the smaller the step, the smaller are the details of the target that the system can resolve. Obviously however, the space resolution also depends on the size of the X-ray beam on the target. For a given selected step, and at equal all other conditions (primary X-ray beam intensity and material composition) the velocity of the movement of the stage determines the amount of counts (statistics) per pixel; a lower velocity results in higher counts, since the corresponding spectrum is accumulated for a longer time. Once established step value and scan velocity, the movement can be chosen as to be a X-Y scan (Figure 6.2 on the left) or a Y-X scan (Figure 6.2 on the right).

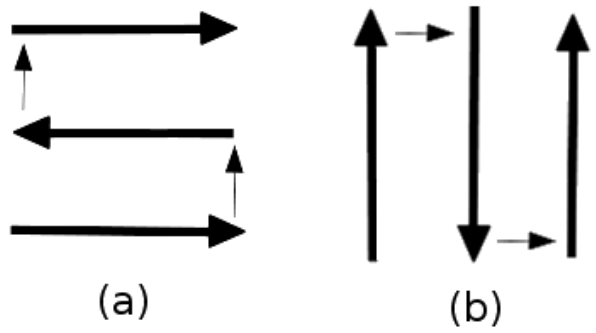


**Figure (6.2).** Scheme of the two ways that the scanning procedure can be set. On the left it is shown what we call an "X-Y" scan, and on the right an "Y-X" scan.

The X-ray tube is turned on manually by setting its potential difference and anode current. Once the X-ray tube reaches its desired working condition[4], the scan and the acquisition of the detector output are switched on by the home-made software. While the measurement head is moving continuously, the ADC is constantly digitizing the detector signals (of an amplitude proportional to the energies of the detected X-rays) and the data are stored in a memory location in the computer. The trigger for data acquisition is internal, i.e., a trigger signal starting the acquisition process is generated when the signal is above a chosen threshold (see below for more details in the ADC paragraph). Each time the linear stage arrives at a position that is a multiple of the preset "step" value, the x and y position are written on the next memory location available with a proper marker (prefix) so as to be recognizable as a position value in the later processing of the map construction.

All communication between different parts of the software is made through shared memory. At the end of the acquisition over the preset area, for each pixel, the spectrum is reconstructed and saved in another memory location[5]. For the construction of the maps the fraction of memory dedicated to the energy spectra associated to each pixel is read. The map coloration relative to a given energy interval (i.e. to a given element with X-rays at that energy) is performed considering the pixel containing the maximum counts

[4]This can be rather fast (tens of seconds) but some precautions must be taken and the increase in voltage and current should not be "instantaneous" to avoid discharges that might damage the tube.

[5]When displaying the spectrum it can also be shown with the scale calibrated in energy. After a proper calibration using a radioactive source or the X-ray emission induced by irradiating a standard of well known composition, the spectrum channels are converted into energy values.

for that energy interval. The maximum corresponds to the maximum value in the RGB scale, and all other pixels are scaled in color to the maximum, assigning black to zero counts.

The software interface, i.e. what is seen on the computer screen, is divided in two windows (Figure 6.3). One is the "main window", dedicated to the integral or elemental map visualization, and another is dedicated to the visualization of the spectrum. For the latter two options are available: by clicking in a pixel in the map, the spectrum of that particular pixel is displayed; and by selecting a rectangular area on the map (dragging the mouse), the spectrum of that area is displayed. Also here, the communication between the two "parts", main window and spectra window, is made by shared memory.

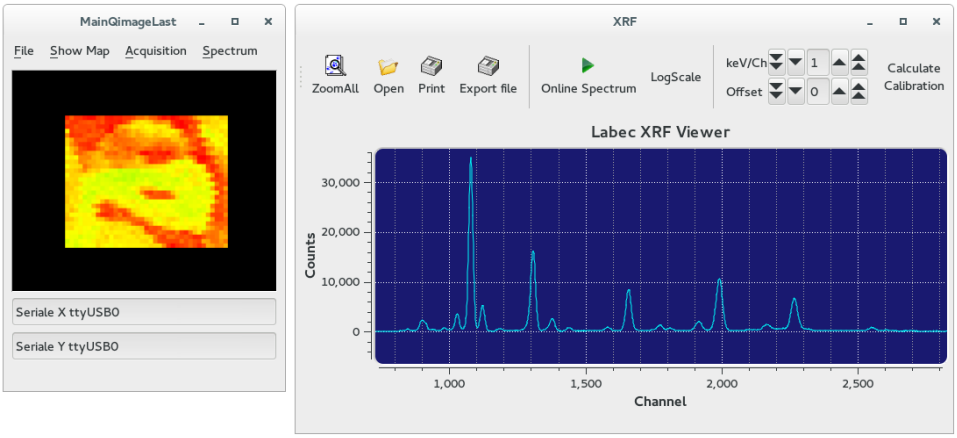


**Figure (6.3).** Software interface of the XRF scanning system. On the left is shown the main window, where a map is visualized, and on the right the spectrum window, where the spectrum of a pixel, of a sub-area or of the whole area can be displayed.

Figure 6.4 shows an example of elemental maps performed with the XRF scanning system prototype. The map was taken from an illuminated letter in a XIV manuscript on parchment. The optical image is shown on the left (A), the image relative to the Cu distribution is shown in the center (B) and the one of the Ca distribution is shown on the right (C). The dimensions of the analyzed area were of about 9 cm x 10 cm, and the experimental conditions were: X-ray tube with Mo anode[6], 20 kV, 0.1 mA, 1 mm beam spot size on sample, 2 mm/s scanning speed and 1 mm step (X-Y scan). It is immediately seen that the Cu and Ca distributions are “complementary” to each other, and - without entering in a discussion about the interpretation of this specific case, which is not within the scope of this work - this example very clearly shows one of the biggest advantages of performing XRF measurements with a scanning system.

[6]When this map was taken, we had at disposal a tube with Mo anode rather than the one with Cr anode that is installed in the last version.

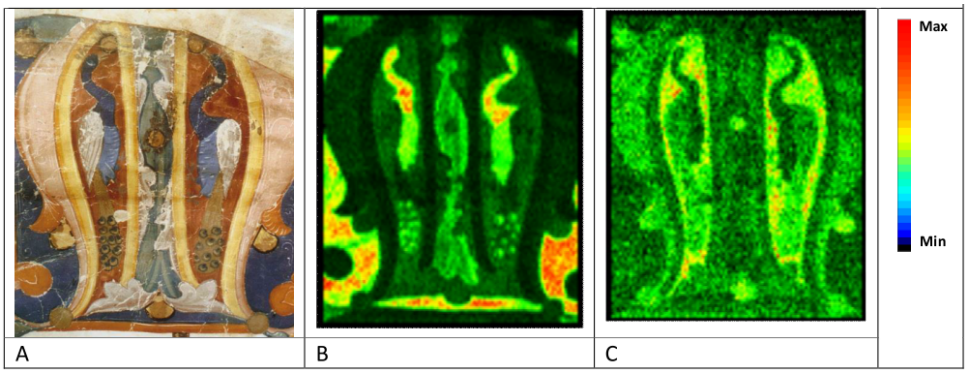


**Figure (6.4).** Example of maps obtained with the XRF scanning system, taken from an illuminated letter in a XIV manuscript on parchment. The dimensions of the analyzed area are 9 cm x 10 cm, and the experimental conditions were: X-ray tube with Mo anode, 20 kV, 0.1 mA, 1 mm beam spot size on sample, 2 mm/s scanning speed and 1 mm step (X-Y scan).

Besides the main procedure described above to construct the map, the main software contains additional features that make it more flexible to user demands. An option that enlarges the map size is available for better details visualization. Another option that was requested by the colleagues that currently use the instrument in museums is the possibility to return exactly to a measured point after a scan. Usually in fact, after a pre-analysis of an area of interest, there is the need for more statistics in a particular point (or sub-region) of the map. By double-clicking on the pixel in the map window the linear stages return to that position of interest with high reproducibility.

## 6.3 THE ANALOG-TO-DIGITAL CONVERTER

The ADC (100 MS/s, 14-bit) used is a desktop system, which means it is portable and requires no crates. Since it allows the user to change the readout parameters according to the detector characteristics, thus enabling the measurement of different signals using the same hardware, the digitizer itself is in fact a Digital Multi Channel Analyzer (MCA). The readout parameters are chosen using commercially available software (CAEN/DPP-PHA Control Software), which permits the visualization in "real time" of the effect of the parameters in the signal manipulation. After the parameters were set for a particular detector signal, they are transferred to a program written in-house in C++, which contains all commands to control the acquisition system, which is directly loaded by the main software each time a new acquisition starts.

To clarify, the DPP-PHA Firmware installed inside the digitizer is a Digital Pulse Processing algorithm that makes the board an actual spectroscopy acquisition system, which provides energy (i.e. pulse height) and timing information as well as portions of the waveform for debugging, monitoring and pulse shape analysis. One of the first stages of the signal handling is the Trigger and Timing Filter (TTF) that is used to identify the input pulses, generate a trigger and provide the time of trigger firing. The TTF implements a digital RC-$CR^2$ filter, as shown in Figure 6.5. The trigger logic gets armed at the threshold crossing, then it generates the trigger signal at the RC-$CR^2$ zero crossing. Setting the threshold value corresponds to set the LLD (lower level discrimination) of the

energy spectrum.

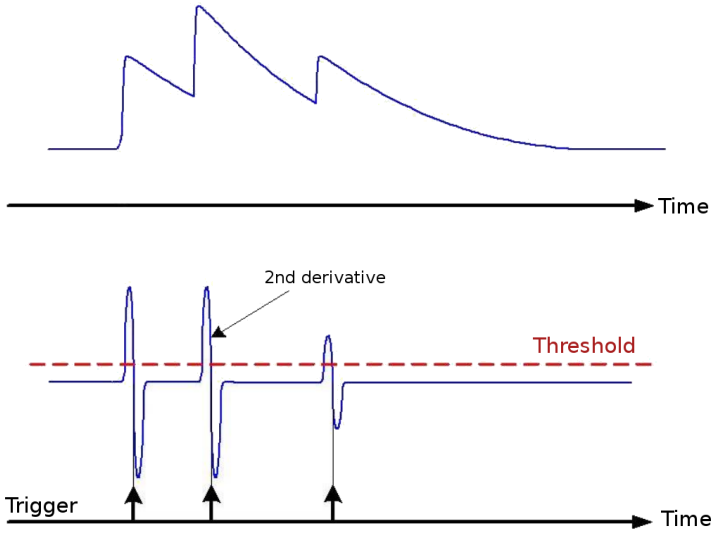


**Figure (6.5).** Simplified view of the TTF filter. The input is shown on top, and the filtered signal on the bottom. This procedure is used to choose the trigger threshold.

Another important stage is the Trapezoidal Filter (Energy Filter). In the traditional analog chain, the Shaping Amplifier is able to convert the exponential shape from the Charge Sensitive Preamplifier into a quasi-Gaussian shape whose height is proportional to the pulse energy. Similarly, the Trapezoidal Filter is able to transform it into a trapezoidal signal, with a flat top height proportional to the input pulse height (energy).

In the first version of our XRF scanning system the SDD detector had its own commercial power supply, inside which is also included the cooling system (Peltier cooler). In a recently improved version, the detector is powered by the digitizer itself thanks to a high voltage output (available in a newer version) that is also controlled from afar through predefined commands sent through the same Ethernet communication as data acquisition. The Peltier cooler control, instead, was made in-house and is installed inside the same box where the other power supplies are placed.

## 6.4 EXAMPLES OF APPLICATIONS

In this paragraph, some examples of applications showing the main kinds of information one can obtain with the scanning XRF system will be presented. The colleagues of the laboratory that were responsible for the application of the XRF scanning system in the studies to be now briefly presented were Anna Mazzinghi and Chiara Ruberto. They were the ones with the right competence to diagnose and characterize artworks, in collaboration with historians and restorers.

As already mentioned, the scanning system is a big step forward compared to single point analysis, in particular for the representativeness of the results, which are no more referred to a single point only. In some cases, choosing the measurement point to perform compositional analysis is critical, and it is possible that the irradiated area eventually comes out to be an “anomalous” point. A case-study that may well illustrate this risk is a

handle (4 cm x 5.3 cm) from a fresco by Botticelli: "Sant'Agostino nello Studio", shown in Figure 5. For the map construction in this case, the scanning step was chosen to be 1 mm, and the scanning velocity 1mm/s. By making an elemental map of calcium, it is possible to see a second handle drawn below the visible one, i.e., what is called a "pentimento" of the painter, which was only possible to be see thanks to the scanning measurement. Besides, in the elemental map of Ti, two retouched areas of the white-painted parts of the handle are clearly seen (pointed out by the presence of a titanium-white pigment, which is a much more modern pigment than available at Botticelli's times); without the map visualization, in the case a single point analysis had been performed "accidentally" on these zones, wrong conclusions might have been extended to the whole white-painted parts of the handle, which were instead originally made using a bone based pigment, as is apparent from the Ca map.

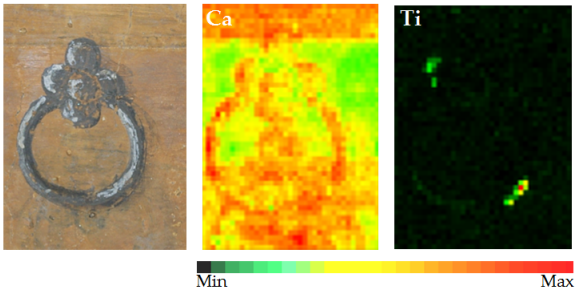


**Figure (6.6).** Example of a 4 cm x 5.3 cm area scanned in a fresco by Botticelli: "Sant'Agostino nello Studio". The scan condition was: scanning step of 1 mm, and scanning velocity of 1mm/s. The maps of Ca and Ti are also shown. The irradiation condition was: Cr anode, 20 kV and 100 $\mu$A.

Another example concerns the spatial resolution of the instrument. Often, the details of an artwork are very small, and thus it is necessary to have the possibility to distinguish the details by performing a higher resolution scan. In order to do that, while keeping the instrument characteristics the same (collimator of 0.8 mm), scannings with smaller steps are performed. Figure 6.7 shows an analysis carried out on a fragment of a Roman mural painting (4 cm x 4.5 cm), where just thanks to the choice of small steps (and low scan velocity to preserve good statistics per pixel), even small details of the face could be resolved: eyes, hair, and lips.

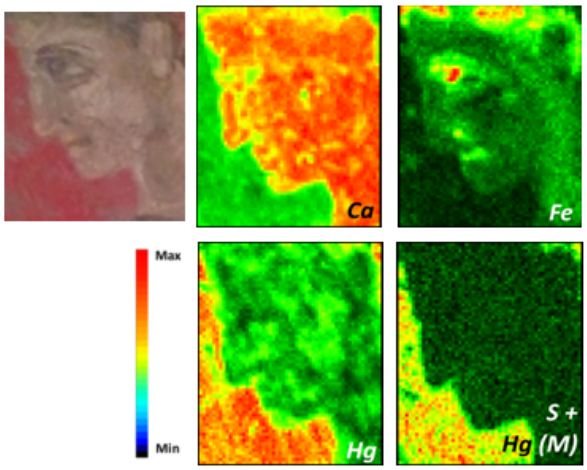


**Figure (6.7).** Example of a 4 cm x 4.5 cm area scanned in a fragment of a Roman mural painting with a "high" resolution scan. The scan condition was: step of 250 $\mu$m and velocity of 250 $\mu$m/s. The irradiation condition was: Cr anode, with 30 kV and 100 $\mu$A.

## 6.5 FIRST MEASUREMENTS ON LAPIS LAZULI STONES

The XRF scanning system was also used on some of the lapis lazuli stones attempting to see whether different regions might be discriminated. For these first attempts, two scanning approaches were used, one where the step was at the minimum, i.e. 250 $\mu$m[7] and correspondingly a low velocity of 250 $\mu$m/s to get enough statistics per pixel, and He flow to detect low-Z elements[8]. We had indeed seen that the "details" with different visual aspect on the stones are very small, so, if the objective was to relate the compositional maps to the visual differences, a smaller scanning step was the best way to attempt identifying the details.

Figure 6.8 shows as an example an elemental map obtained from a region in the AFG13 sample (top left). Calcium (top center) is correlated to the whitish areas of the stones, which are generally a visual indication of the white, Ca-containing minerals calcite and diopside (in the case of Asian samples). Iron (top right) is found in higher quantities in the darker zones, an indication of pyrite. In this case, potassium (mostly related to blue zones) was found to be anti-correlated to the areas where Ca is more abundant. Sulphur was found to be correlated to the zones of Fe, (quite reasonably, because of the presence of pyrite, $FeS_2$) and also to another "hot spot" that is seen as "opaque" white in the irradiated area. In the same spot as one of those containing Sulphur, a Si "hole" is seen.

[7]Smaller steps would be anyway of no use, owing to the larger size of the collimator defining the primary X-ray beam size.

[8]A helium flow in front of the detector very effectively decreases the absorption of the emitted secondary X-rays at the lowest energies, thus increasing the sensitivity in the detection of low-Z elements (whose production is already disfavored by the low cross section of the photoelectric effect). With a path in air rather than helium (even short, of about 3 cm, as in our setup), X-rays below 3 keV would instead be drastically absorbed, making the system totally blind to the detection of elements like Mg, Al, Si, P, S.

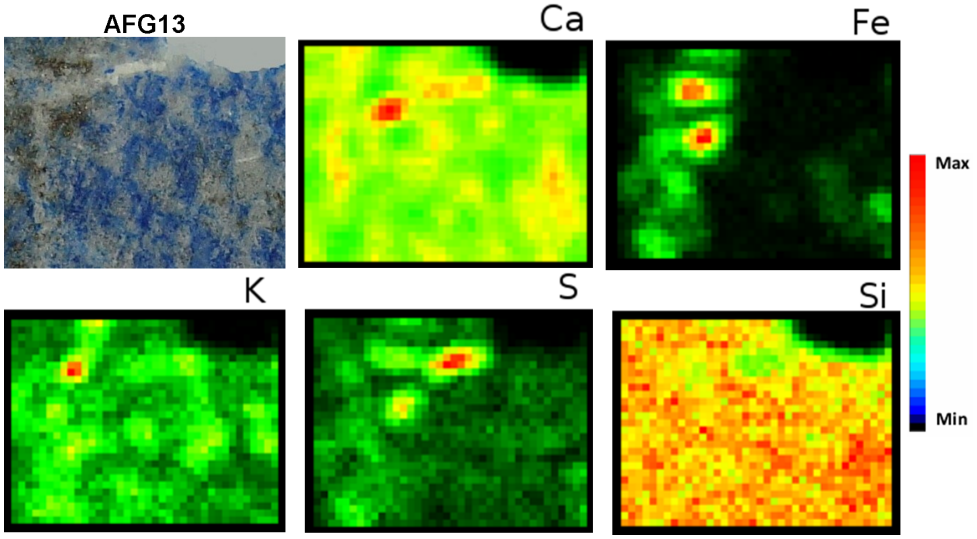


**Figure (6.8).** Example of "high" spatial resolution maps (step of 250 $\mu$m and velocity of 250 $\mu$m/s) performed at lapis lazuli stones, taken from an area of the AFG13 sample (10 mm x 8 mm). The elemental maps of Ca, Fe, K, Si, S are shown.

Besides the measurements just presented, another approach, in a sense complementary to the previous one, was also taken, with a scanning step of 1 mm and velocity of 1 mm/s. This set of measurements was performed attempting to see whether "macroscopic" homogeneous areas might be found, as a way of selecting zones for the TRIBIL measurements. Figure 6.9 shows an example taken from CHILE3. Although the poor statistics does not allow us to draw in general strong conclusions, it can be seen how Fe is related to the "dark" zones of the stone, which reasonably correspond to pyrite areas, as also indicated by a higher number of counts of the sulphur X-rays. The map of potassium seems to be at least in part correlated to those of Fe and S. The Ti map does not seem to show correlation to any other element nor any visually characterized areas. Finally, there is a feature that may be interesting to critically discuss in these results: Ca is distributed along the whole zone without "hot spots" but more smoothly, with a higher number of X-ray counts in a large "stripe" on the left. Since - as we have seen in the previous example - Ca is usually related to whitish zones, which are not optically visible as a large area in the sample, there are two possibilities for the appearance of the stripe of higher Ca X-ray counts: either there is a thin layer of a mineral not seen with the naked eye on the large stripe zone, or the small white veins which are indeed visible result in a larger stripe in the map because of lack of spatial resolution in these measurements.

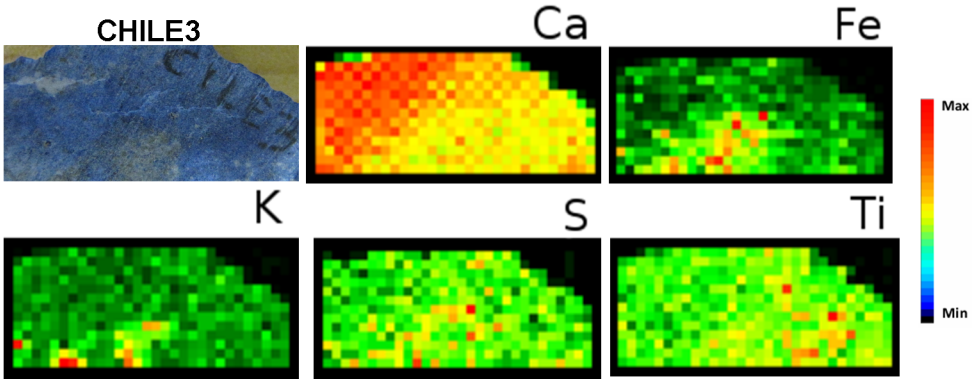


**Figure (6.9).** Example of maps from a stone (3 cm x 1.3 cm), taken from CHILE3, performed with a step of 1 mm and velocity of 1 mm/s. The elemental maps of Ca, Fe, K, S, and Ti are shown.

These very first attempts of XRF mapping on lapis lazuli have only been reported to witness the effort we made to find a simple preliminary analysis that might then guide the choice of the areas, on which to perform the TRIBIL measurements reported in the previous Chapter. We must admit that the goal was only very partially achieved: in order to be really effective to the purpose, many more measurements, and above all, higher statistics should have been collected to make it possible to extract useful information to that specific purpose. This was not possible to be done so far, also for the trivial reason of lack of time. However, it is undeniable that it has been very important to have made more in general available to the laboratory an efficient and versatile XRF scanning system with the characteristics reported in this Chapter, as by the way demonstrated by the two cases concerning the fresco by Botticelli and the small Roman mosaic, reported above in the previous paragraph. Many more examples of applications, where the portable XRF scanning system implemented during my PhD proved to be crucially important to solve diagnostic problems in the field of Cultural Heritage, can be found in another PhD dissertation that is presently being presented for discussion in the doctorate of Science for Cultural Heritage of the Florence University [81].

# CONCLUSION AND FINAL REMARKS

Exploiting the pulsed ion beam facility (DEFEL) of the LABEC laboratory, my PhD work, concerning time-resolved luminescence induced by ion beams, proposed new methods to perform this kind of measurement. The most important innovations of this work were possible thanks to a thorough exploitation of the potentials of the DEFEL beamline (which had not been frequently used in the past years). Pulses with a large number of particles per bunch were needed to be generated by the DEFEL beam line, and even heavy ion beams - never used previously in pulsed mode at LABEC - were exploited. As to data acquisition, the innovation consisted in the implementation of a new way to process the TRIBIL signals, using a sampling ADC.

The basic idea behind the experiments was the following: a signal coming directly from the DEFEL chopper, related to the arrival of the bunch of particles in the target, was used as an external trigger for the acquisition system; the luminescence signal from the target was amplified by a photomultiplier tube; the PMT output was directly sent to the ADC input; an acquisition window was defined in such a way that the rise and decay luminescence signal was saved, as well as digitized samples for baseline calculations. For proper data analysis, for each measuring condition a large number of pulsed irradiations was repeated in sequence (from hundreds to thousands), with a frequency of 10 Hz, and an average luminescence signal was calculated for each irradiated point. This also allowed us to verify the good reproducibility of the results.

The setup was "checked" with a standard scintillator ($CdWO_4$) and two of its known lifetimes ($\approx$5 $\mu$s and 14 $\mu$s) were found, in agreement with the ones published in the literature. Therefore, we can conclude that thanks to this work an original and very effective "instrument" for material analysis through the study of their luminescence behavior has been implemented. It has proven to be reliable and very versatile, in that it allows one to check the material luminescence response to a variety of excitation conditions: we have in fact developed and fine tuned the possibility of varying many irradiation parameters (beam intensity, ion species, pulse duration). In addition, a first setup for wavelength discrimination of the emitted luminescence has been realized.

The TRIBIL setup was then applied to try and see whether it might contribute to provenance studies of lapis lazuli. This stone is of great interest for the Cultural Heritage community, and several studies had attempted to find markers that could discriminate

one origin from the others. Some provenance markers had been already proposed in previous studies using various techniques, and we applied TRIBIL in the hope to find other possible markers to discriminate further origins. To this purpose, three samples from Afghanistan, three from Chile, two from Myanmar, two from Tajikistan and four from Siberia were irradiated, each on several different spots and under different irradiation conditions.

Our TRIBIL application to the lapis lazuli was approached in a particular manner. Indeed, a "theoretical" interpretation of the luminescence results of lapis lazuli is problematic, in particular because of the intrinsically inhomogeneous character of these semi-precious stones that may be constituted by a large variety of different minerals - each, in addition, possibly containing several impurities. Therefore, not only we tested the response of the samples in as many ways as possible, by varying the excitation parameters, but we also tried different ways to empirically describe the luminescence behavior after excitation through different parameters. In other words, knowing that the temporal trend of the luminescence signal decay after pulsed irradiation can be dependent on factors such as dose and dose rate of the pulse, and on the ion species, besides being different at different wavelengths, our approach was to change the irradiation conditions and try to create a "catalog" of the luminescence behavior from lapis lazuli, hoping that systematic differences among the origins would eventually be observed.

During this process, "unexpected" behaviors on the luminescence decay signal were observed and investigated. While most of the luminescence decay signals could be fitted with multi-exponential decays, some behaviors from lapis lazuli (also observed in the standard scintillators), after a certain beam current could not be simply described by a sum of exponentials. Instead, a sort of plateau was observed that changed "amplitude" depending on the sample and beam current. Notwithstanding the reason for its appearance is not clear and must be further investigated, for the curves showing such a plateau the average decay lifetime was calculated and taken as an empirical parameter to describe the observed behavior.

The amount of data obtained in our measurements on lapis lazuli was very large, and trying to disentangle the different possible contributions to the observed differences and extract which ones (if any) were safely attributable to the different provenances, proved to be a very hard task. The most promising results, perhaps, were the ones obtained irradiating the lapis lazuli samples with 3 MeV protons, 60 nA of beam current, and performing wavelength discrimination in the 450 nm region, suggesting that an intense excitation together with a spectrometric analysis of the emitted luminescence might be the path for good discrimination criteria. By calculating the average lifetime of each decay curve, clusters were indeed observed for the samples from Chile, Tajikistan and Siberia. Even though the results from AFG13 ended up being similar - for these irradiation conditions - to those from Tajikistan, showing an "anomalous" behavior with respect to the other Afghan samples, AFG13 can however be clearly distinguished from the Tajikistan ones by performing measurements under another irradiation condition.

In conclusion therefore, although not to a really satisfactory level, some hints have been found, if one considers the whole of the measurements performed under different conditions, and not the single sets of irradiations under each of the various conditions.

Since another significant activity I was involved in during my PhD was the development of the first version of the XRF scanning system of LABEC, a brief description of this instrument has also been given in the thesis. Implementing a portable XRF system to determine the composition of materials of interest for Cultural Heritage in situ (in museums, churches, restoration laboratories) has opened in itself the way to give our contribution in a much larger number of case-studies, whenever it is not possible to move the artwork to our laboratory for the Ion Beam Analysis with the accelerator. In addition, the XRF system developed, thanks to the scanning option, allows us to obtain elemental maps of the different elements rather than only "point" analysis, which represents a great leap ahead for the representativeness of the results. Many interesting applications have already been performed with the instrument I contributed to design and realize, and they have been reported in other works. In this thesis, I limited myself to a short description of the technical aspects of the system and to some examples of application just to illustrate its potentials. Also shortly described are some preliminary results from measurements that were carried out just on the same lapis lazuli stones that were also the object of the TRIBIL measurements. In particular, for the latter measurements, the XRF maps obtained showed that it might be possible to discriminate different zones when pushing to better levels the spatial resolution of the system. Future measurements might then concentrate on finding trace elements correlated with particular areas from the stone and focus on the possibility of a preliminary selection of the areas in order to select those that promise to be better candidates for a discriminating TRIBIL analysis.

Coming back to the main subject of this thesis (TRIBIL), I believe that the most relevant outcome of general interest from this work, as mentioned above, is having made available at LABEC a new, very powerful tool for the characterization of materials in general. This now opens the possibility of new collaborations, in a field that is beyond those traditionally covered so far in the laboratory. Of course, still some work remains to be done in order to optimize the new facility. Among other improvements, a dedicated, more suitable vacuum chamber than the existing one (which had been initially built for completely different purposes when DEFEL was first designed) would make the change of setups much easier and faster; different PMTs and wavelength filters might be used, also implementing "smart" systems to insert and exchange them in front of the PMT without breaking the vacuum in the chamber; for the data acquisition, faster digitizers of the luminescence signal might be also used to better resolve the fast components of the luminescence decays.

We do hope to be able to implement such improvements in the near future.

# BIBLIOGRAPHY


[1] N. Taccetti, et al. The pulsed beam facility at the 3 MV Van de Graaff accelerator in Florence: Overview and examples of applications. *Nucl. Instr. and Meth. B*, (188):255–260, 2002.

[2] F. A. Mirto and L. Carraresi. The pulsed beam facility at the Tandetron accelerator in Florence. *Nucl. Instr. and Meth. B*, (266):2113–2116, 2008.

[3] S. Calusi, et al. The ionoluminescence apparatus at the LABEC external microbeam facility. *Nucl. Instr. and Meth. B*, (266):2306–2310, 2008.

[4] R. Hellborg. *Electrostatic Accelerators: Fundamentals and Applications*. Springer, 2005.

[5] M. Kiisk, et al. The charge state distribution of a carbon beam measured at lund pelletron accelerator with the newly installed terminal pumping system in use. *Nucl. Instr. and Meth. B*, (481):1–8, 2002.

[6] H. Liebl. *Applied Charged Particle Optics*. Springer, 2008.

[7] M. Reiser. *Theory and Design of Charged Particle Beams*. Wiley, 2004.

[8] K. Wille. *The Physics of Particle Accelerators: An Introduction*. Clarendon Press, 2001.

[9] F. Lucarelli, et al. The upgraded external-beam PIXE/PIGE set-up at LABEC for very fast measurements on aerosol samples. *Nucl. Instr. and Meth. B*, (318):55–59, 2014.

[10] L. Giuntini, et al. The external scanning proton microprobe of Firenze: A comprehensive description. *Nucl. Instr. and Meth. A*, (576):266–273, 2007.

[11] N. Taccetti, et al. Linear electronics for Si-detectors and its energy calibration for use in heavy ion experiments. *Nucl. Instr. and Meth. A*, (496):491–495, 2003.

[12] A. Castoldi, et al. Longitudinal profile of the charge cloud at high charge levels in multi-linear silicion drift detectors for position-sensing applications. *IEEE Trans. Nucl. Sci.*, pages 575–579, 2011.

[13] P. G. Bizzeti, et al. Response of $CdWO_4$ crystal scintillator for few MeV ions and low energy electrons. *Nucl. Instr. and Meth. A*, (696):144–150, 2012.

[14] S. Sciortino, et al. Micro-beam and pulsed laser beam techniques for the microfabrication of diamond surface and bulk structures. *Nucl. Instr. and Meth. B*, (348):191–198, 2015.

[15] L. Palla, et al. Accurate on line measurements of low fluences of charged particles. *EPJ Plus*, (130):39–44, 2015.

[16] F. A. Mirto. *New set-ups at LABEC, Florence: beam transport network controls, pulsed beam facility, scanning system for elemental mapping.* PhD thesis, Physics Department, University of Florence, 2007.

[17] P. D. Townsend and Y. Wang. Defect studies using advances with ion beam excited luminescence. *Energy Procedia*, (41):64–79, 2013.

[18] R. Brooks. *Modern Luminescence Spectroscopy of Minerals and Materials.* Springer, 2005.

[19] A. Bettiol, et al. The characterization of high-grade synthetic quartz, corundum and spinel using ionoluminescence (IL). *Nucl. Instr. and Meth. B*, (130):734–739, 1997.

[20] A. A. Finch, et al. Ionoluminescence of zircon: rare earth emissions and radiation damage. *J. Physics D*, (37):734–739, 2004.

[21] H. Calvo del Castillo, et al. Ionoluminescence of diamond, synthetic diamond and simulants. *Nucl. Instr. and Meth. A*, (580):400–403, 2007.

[22] H. Calvo del Castillo, et al. Some new trends in the ionoluminescence of minerals. *Anal. Bioanal. Chem.*, (387):869–878, 2007.

[23] W. Becker, et al. Fluorescence lifetime imaging by time-correlated single-photon counting. *MRT*, (63):58–66, 2004.

[24] H. Calvo del Castillo, et al. Relationship between ionoluminescence emission and bond distance (M-O) in carbonates. *Nucl. Instr. and Meth. B*, (249):217–220, 2006.

[25] D. Jimenex-Ray, et al. Ionoluminescence induced by swift heavy ions in silica and quartz: A comparative analysis. *Nucl. Instr. and Meth. B*, (286):282–286, 2012.

[26] W. Hays and A. M. Stoneham. *Defects and defect processes in non-metallic solids.* Denver Publications, 2004.

[27] M. Aguilar, et al. Luminescence of NaCl-I. Electron and ion beam excited spectra. *Radiation Effects*, (40):1–7, 1979.

[28] M. Gaft. *Modern Luminescence Spectroscopy of Minerals and Materials.* Springer, 2005.

[29] P. D. Townsend, et al. Luminescence detection of phase transitions, local environment and nanoparticle inclusions. *Contemporary Physics*, (49):255–280, 2008.

[30] S. Tavernier. *Experimental Techniques in Nuclear and Particle Physics.* Springer, 2010.

[31] G. F. Knoll. *Radiation Detection and Measurement.* Wiley, 2010.

[32] W. Becker. *Handbook of stopping cross-sections for energetic ions in all elements.* Pergamon Press, 1980.

[33] D. Fink and L. T. Chadderton. Ion-solid interaction: Status and perspectives. *BJP*, (35):737–740, 2004.

[34] J. R. Lakowicz. *Principles of Fluorescence Spectroscopy*. Springer, 2006.

[35] A. S. Marfunin. *Spectroscopy, Luminescence and Radiation Centers in Minerals*. Springer, 1979.

[36] J. B. Birks. *The Theory and Practice of Scintillation Counting*. Pergamon Press, 1967.

[37] I. Pelant and J. Valenta. *Luminescence Spectroscopy of Semiconductors*. OUP Oxford, 2012.

[38] T. Calderón. Ionolumminescence and minerals: the state of the art. *Rev. Mex. Fis.*, (54):21–28, 2008.

[39] A. Taraschan. *Luminescence of Minerals*. Naukova Numka, 1978.

[40] B. S. Gorobets, et al. Luminescence spectroscopy of the earth. *Radiat. Meas.*, (24):485–491, 1995.

[41] M. Gaft. Application of laser induced luminescence in ecology. *Water Sci. Tech.*, (27):547–556, 1993.

[42] M. Gaft, et al. Laser-induced time-resolved luminescence of minerals. *Spectrochimica Acta Part A*, (54):2163–2175, 1998.

[43] G. Baldacchino, et al. Direct time-resolved measurement of radical species formed in water by heavy ions irradiation. *Nucl. Instr. and Meth. B*, (146):528–532, 1998.

[44] E. Gardès, et al. SPORT: A new sub-nanosecond time-resolved instrument to study swift heavy ion-beam induced luminescence - application to luminescence degradation of a fast plastic scintillator. *Nucl. Instr. and Meth. B*, (297):39–43, 2013.

[45] K. Kimura. Ultra-fast luminescence in heavy-ion track-cores in insulators: Electron-hole plasma. *Nucl. Instr. and Meth. B*, (212):123–134, 2003.

[46] M. Koshimizu, et al. Time-resolved luminescence spectra of electron-hole plasma in ion-irradiated CdS. *Nucl. Instr. and Meth. B*, (212):376–380, 2003.

[47] M. Hofmann, et al. Ion-beam excitation of liquid argon. *EPJ C*, (73):1–16, 2013.

[48] C. Da Cunha. *Le lapis lazuli: son histoire, ses gisements, ses imitations*. Editions du Rocher, Paris, 2004.

[49] C. Klein. *Mineralogy*. Zanichelli, 2004.

[50] D. P. Silverman. *Wonders of Tutankhamun, An Artabras Book*. Crown Publishers, 1978.

[51] G. W. Bowersox and B. E. Chamberlin. *Gemstones of Afghanistan*. Geoscience Press, 1995.

[52] J. Wyart, et al. Lapis lazuli from Sar-i-Sang, Badakhshan, Afghanistan. *Gems and Gemmology*, (17):184–190, 1981.

[53] G. Herrmann, et al. Lapis lazuli: the early pahases of its trade. *Iraq*, (30), 1968.

[54] B. Aston, J. Harell and I. Shaw. *Ancient Egyptian Materials and Technology*. Cambridge University Press, 2000.

[55] R. Webster. *Gems, their sources, descriptions and identification*. Butterworths, 1975.

[56] A. S. Sofianides and G. E. Harlow. *Gems and Crystals from the American Museum of Natural History*. Simon and Schuster, 1990.

[57] D. D. Hogarth and W. L. Griffin. Contact-metamorphic lapis lazuli: The Italian Mountain deposits, Colorado. *Canadian Mineralogist*, (18), 1980.

[58] M. Tosi. *The Lapis Lazuli trade across the Iranian plateau in the 3rd millennium B.C.* published in "Studi di onore di Giuseppe Tucci", Istituto Universitario Orientale, Napoli, 3.

[59] P. Ballirano and A. Maras. Mineralogical characterization of the blue pigment of Michelangelo's fresco "The last judgment". *American Mineralogist*, (91):997–1005, 2006.

[60] A. Borelli, et al. Caratterizzazione del lapislazzuli. *La Gemmologia*, pages 24–27, 1986.

[61] C. Cipriani, et al. Le collezioni del museo di mineralogia di Firenze: VI) Lapislazzuli. *Museologia Scientifica*, 1988.

[62] M. Bacci, et al. An integrated spectroscopic approach for the identification of what distinguished Afghan lapis lazuli from others. *Vibrat. Spec.*, (49):80–83, 2009.

[63] G. D. Smith and R. J. Klinshaw. The presence of trapped carbon dioxide in lapis lazuli and its potential use in geo-sourcing natural ultramarine pigment. *J. Cult. Herit.*, (10):415–421, 2009.

[64] L. Osticioli, et al. Analysis of natural and artificial ultramarine blue pigments using laser induced breakdown and pulsed Raman spectroscopy, statistical analysis and light microscopy. *Spect. Acta Part A*, (73):525–531, 2009.

[65] C. M. Schmidt, et al. Characterization of lapis lazuli pigments using a multitechnique analytical approach: implications for identification and geological provenancing. *Anal. Chem.*, (81):8513–8518, 2009.

[66] M. Favaro, et al. Characterization of lapis lazuli and corresponding purified pigments for a provenance study of ultramarine pigments used in works of art. *Anal. Bioanal. Chem.*, (402):2195–2208, 2012.

[67] M. Derrick. *Infrared Spectroscopy in Conservation Science*. The Getty Conservation Institute, 1999.

[68] J. Zöldföldi, et al. Where does lapis lazuli come from? non-destructive provenance analysis by PGAA. *34th International Symposium on Archaeometry*, pages 353–361, 2004.

[69] A. Re, et al. Lapis lazuli provenance study by means of micro-PIXE. *Nucl. Instr. and Meth. B*, (269):2373–2377, 2011.

[70] A. Re, et al. New markers to identify the provenance of lapis lazuli: trace elements in pyrite by means of micro-PIXE. *Appl. Phys. A*, (11):69–74, 2013.

[71] A. Quaranta, et al. Ion beam induced luminescence analysis of painting pigments. *Nucl. Instr. and Meth. B*, (574):289–294, 2007.

[72] A. Lo Giudice, et al. Multitechnique characterization of lapis lazuli for provenance study. *Anal. Bioanal. Chem.*, (395):2211–2217, 2009.

[73] C. D. H. Herd and R. C. Peterson. Violet-colored diopside from Southern Baffin Island, Nuvanut, Canada. *Ca. Miner.*, (348):1193–1199, 2000.

[74] L. H. Abu-Hassan and P. D. Townsend. Luminescence efficiency of silica during ion beam excitation. *Nucl. Instr. and Meth. B*, (32):293–298, 1988.

[75] K. Moritani, et al. Production behavior of irradiation defects in vitreous silica under ion beam irradiation. *J. Nucl. Mat.*, (312):97–102, 2003.

[76] S. Kitazawa, et al. Radiation-induced luminescence and photoluminescence from sol–gel silica glasses and phosphosilicate glasses by 1 MeV $H^+$ irradiations. *Physica B*, (349):159–165, 2004.

[77] J. V. P. Long and S. O. Agrell. The cathodo-luminescence of mineral in thin sections. *Miner. Mag.*, (34):318–326, 1965.

[78] T. Fazzini, et al. Pulse-shape discrimination with $CdWO_4$ crystal scintillators. *Nucl. Instr. and Meth. A*, (410):213–219, 1998.

[79] C. L. Melcher, et al. Applicability of Barium Fluoride and Cadmium Tungstate scintillators for Well Logging. *IEEE Transactions on Nuclear Science*, (36):1188–1192, 1989.

[80] https://root.cern.ch/.

[81] A. Mazzinghi. *Sviluppo di strumentazione XRF a scansione per applicazioni ai Beni Culturali*. PhD thesis, University of Florence, 2015.

# ACKNOWLEDGMENTS

Firstly I want to thank my tutor, Pier Andrea Mandò, for accepting to supervise me and encourage me to pursue the unknown;

I want to thank my dear colleague and friend, Lara Palla, without whom this work could not have been done. Thank you for always sharing with me your knowledge, reminding me that science goes on because of altruistic people like you;

I thank Francesco Taccetti, for the patience when I still could not speak Italian, teaching me everything I needed and for repeating "countless" times the same thing until I could finally understand.

I want to thank Alessandro Lo Giudice and Alessandro Re, for lending me their lapis lazuli stones and giving me advice concerning the work. Also, I want to thank Giovanni Pratesi, for lending me additional lapis lazuli stones. Without you this work could not have been carried on;

I want to thank Alberto Catelani, for the construction of many parts of the setup. And in particular Marco Manetti, not only for building my setup pieces in record time but also for the friendship along these years;

I want to thank Giovanni Agati, Guido Toci, Anna Gueli and Giulio Campo for providing essential instrumentation for this work;

I want to warmly thank my dear colleagues and friends, Anna Mazzinghi, Chiara Ruberto and Lucia Liccioli, not only for the great advice concerning my work, but also for always being willing to listen and make me laugh;

I want to thank the whole LABEC group, specially Lorenzo Giuntini, Mirko Massi, Luca Carraresi and Nello Taccetti, for helping me whenever I needed, giving me ideas on how to proceed with the work, passing me their great knowledge;

I thank Alberto Quaranta and Matteo Dalla Palma for important insight and advice;

I want to thank my parents, because without them I could have never pursued my passion for physics. Thank you for always believing in me, and teaching me that love for what you do is fundamental;

I thank my brothers, because their love and admiration make me always reach higher;

And a special final “thank you” to Tommaso Innocenti, for never letting me think I was not capable. Your love and patience kept me serene so I was able to enjoy the PhD in its whole, wonderful experience.